

Shape fluctuation and deformation of biological soft interfaces

Hiroaki Ito

Abstract

Life is one of the emergent phenomena of nature in this world, and the mechanism of life phenomena should follow the laws of nature. From such a standpoint, physics, which tackles the laws of nature from a fundamental perspective, would be able to provide us with knowledge that helps us understand the essential aspects of life phenomena. Existing lives are consisting of a micrometer-scaled minimum unit, called a cell, and the inner and outer worlds of the cells are separated by the soft membrane structure, called cell membrane or plasma membrane, mainly composed of phospholipids and membrane proteins. As a biological interface, the cell membrane with the underlying supporting network structure of specific proteins, called cytoskeleton, not only responds to external stimuli such as the changes in concentration gradient of substances and mechanical environment but also spontaneously express membrane fluctuation and deformation to realize active life phenomena: cell motility, cell division, embryonic development, endo- and exo-cytosis, and so on, for example. In other words, “living” state is sustained through the dynamic non-equilibrium interfacial phenomena at biological interfaces.

It is, in general, highly challenging to understand the material properties, *e.g.*, viscoelasticity, or physical properties and mechanisms underlying the fluctuation and deformation of the biological interfaces, because the biological interfaces are composed of an extraordinary variety of soft materials such as lipid molecules, membrane proteins, cytoskeletal proteins, motor proteins, etc, and their hierarchically-higher-order structures. To build a better understanding of them, it is necessary to investigate how biological molecules behave and interact with each other, what kind of higher-order structures they hierarchically form, and how these structures develop over time, from physics of “soft matters”.

In this thesis, we address these challenging problems from the aspect of the fluctuation and deformation of biological interfaces. To gain an essential understanding of their physical natures by treating them as biological soft matters, we investigated both living and non-living interfaces composed of a vast number of biological molecules. The living system is a red blood cell with the cell membrane and the connected spectrin cytoskeletal network, whose fluctuation and deformation in response to the external stimuli by endotoxins are characterized by bending stiffness and spring constant of shape confinement by cytoskeletal network. The non-living system is the lipid monolayer connected to actin and myosin, which actively generate a contractile forces by consuming adenosin-triphosphate (ATP). We experimentally reconstitute the active interfacial deformation caused by actomyosin for the first time, and discuss the physical natures of the emergent two different kinds of interfacial fluctuation and deformation in correlation with the different higher-order structure formations of actin and myosin inside the micrometer-scaled confinement. Finally, we study an experimental method, called droplet transfer method, with a view to form a lipid bilayer system from the lipid monolayer system encapsulating actin and myosin.

Contents

List of Publications	6
I General introduction	7
1 Biological interfaces	8
1.1 Cell membrane	9
1.2 Cytoskeleton	10
1.2.1 Actin filaments	11
1.2.2 Microtubules	12
1.2.3 Intermediate filaments	13
1.2.4 Spectrin	13
2 Reconstitution of biological interfaces	14
2.1 Phospholipids	14
2.2 Hierarchical structure of phospholipids	15
2.2.1 Lipid monolayer	18
2.2.2 Lipid bilayer	19
3 Fluctuation and deformation of soft interfaces	21
3.1 Bending energy	21
3.1.1 Derivation of bending energy from theory of elasticity	23
3.2 Surface tension	28
3.2.1 Laplace pressure	28
3.3 Fluctuation and deformation of a lipid membrane	29
3.4 Fluctuation and deformation of cell shape	32
4 Outline of the thesis	36
II Passive shape fluctuation and deformation of a cell	38
5 Shape fluctuation of a red blood cell	39
5.1 Introduction	39
5.2 Materials and methods	41
5.2.1 Sample preparation	41
5.2.2 Microfluidic diffusion chamber	42
5.2.3 Microscopic observation	44

CONTENTS

5.2.4	flicker spectroscopy	44
5.2.5	Correlation coefficient	45
5.3	Results	46
5.3.1	Morphological transition	46
5.3.2	Quantification of elastic moduli	47
5.4	Discussion	49
5.4.1	Physical mechanism of echinocytosis	50
5.4.2	Mechanics of adult and neonatal RBCs	52
5.4.3	Impact of molecular chemistry	55
5.4.4	Impact of P19	55
5.5	Conclusion	56
 III Active shape fluctuation and deformation caused by actomyosin		57
6	Active shape fluctuation caused by actomyosin	58
6.1	Introduction	58
6.2	Materials and methods	59
6.2.1	Cell culture	59
6.2.2	Preparation of actomyosin fraction	59
6.2.3	Preparation and observation of actomyosin droplets	60
6.3	Results	61
6.3.1	Reconstitution of actomyosin droplets	61
6.3.2	Dynamic interfacial deformation	65
6.3.3	Symmetry breaking of the interfacial fluctuation	68
6.3.4	Molecular contributions to the force generation	70
6.4	Discussion	72
6.4.1	Non-periodicity	73
6.4.2	Non-Gaussianity	75
6.4.3	Mechanism of the oscillatory deformation	75
6.5	Conclusion	78
7	Active deformation caused by actomyosin	79
7.1	Introduction	79
7.2	Materials and methods	80
7.3	Results	80
7.3.1	Wrinkle development	80
7.3.2	Characterization of actomyosin-induced deformation	82
7.3.3	Curvature dependence of the wrinkled shape	83
7.4	Discussion	84
7.4.1	Theoretical model for the onset of wrinkling	84
7.4.2	Effect of interfacial tension	87
7.5	Conclusion	88

IV	Toward reconstitution of an artificial cell	89
8	Dynamics of droplet transfer at an oil/water interface	90
8.1	Preparation method of cell-sized lipid bilayer vesicles	90
8.1.1	Conventional preparation method	90
8.1.2	Droplet transfer method	91
8.2	Materials and methods	92
8.3	Results	94
8.3.1	Observation of transfer kinetics	94
8.3.2	Size dependence of transfer kinetics	95
8.4	Discussion	96
8.4.1	Theoretical modeling	96
8.4.2	Potential barrier to the adhesion of two monolayers	101
8.4.3	Relation to the force balance model	102
8.5	Conclusion	103
9	Application of kinetic filtration effect	104
9.1	Introduction	104
9.2	Materials and methods	105
9.2.1	Materials	105
9.2.2	Fabrication of a microfluidic device	105
9.2.3	Preparation of an oil phase with lipids	105
9.2.4	Generation of cell-sized liposomes	105
9.2.5	Investigation of the size distribution of microdroplets discharged from the glass capillary	106
9.2.6	Generation of W/O microdroplets by hand tapping, and generation of liposomes by the standard droplet transfer method	106
9.3	Results	106
9.3.1	Droplet-shooting and size-filtration (DSSF) method	106
9.3.2	Mechanism of cell-sized liposome generation by DSSF method	107
9.4	Conclusion	109
V	General conclusion	111
10	General conclusion and future prospects	112
10.1	General conclusion	112
10.2	Problems and future prospects	114
	Acknowledgement	116

List of publications

Publications covered in this thesis

H. Ito, N. Kuss, B. E. Rapp, M. Ichikawa, T. Gutschmann, K. Brandenburg, J. M. B. Pöschl, and M. Tanaka, “Quantification of the Influence of Endotoxins on the Mechanics of Adult and Neonatal Red Blood Cells” *The Journal of Physical Chemistry B* **119**, 7837-7845 (2015).

Y. Nishigami*, H. Ito*, S. Sonobe, and M. Ichikawa, “Non-periodic oscillatory deformation of an actomyosin microdroplet encapsulated within a lipid interface” *Scientific Reports* **6**, 18964 (2016). *These authors contributed equally to this work.

H. Ito*, Y. Nishigami*, S. Sonobe, and M. Ichikawa, “Wrinkling of a lipid interface induced by actomyosin cortex” *Physical Review E* **92**, 062711 (2015). *These authors contributed equally to this work.

H. Ito, T. Yamanaka, S. Kato, T. Hamada, M. Takagi, M. Ichikawa, and K. Yoshikawa, “Dynamical formation of lipid bilayer vesicles from lipid-coated droplets across a planar monolayer at an oil/water interface” *Soft Matter* **9**, 9539-9547 (2013).

Related publications

M. Morita, H. Onoe, M. Yanagisawa, H. Ito, M. Ichikawa, K. Fujiwara, H. Saito, and M. Takinoue, “Droplet-shooting and size-filtration (DSSF) method for synthesis of cell-sized liposomes with controlled lipid compositions” *ChemBioChem* **16**, 2029-2035 (2015).

H. Ito, M. Yanagisawa, M. Ichikawa, and K. Yoshikawa, “Emergence of a thread-like pattern with charged phospholipids on an oil/water interface” *The Journal of Chemical Physics* **136**, 204903 (2012).

H. Himeno, H. Ito, Y. Higuchi, T. Hamada, N. Shimokawa, and M. Takagi, “Coupling between pore formation and phase separation in charged lipid membranes” *Physical Review E* **92**, 062713 (2015).

Part I

General introduction

Chapter 1

Biological interfaces

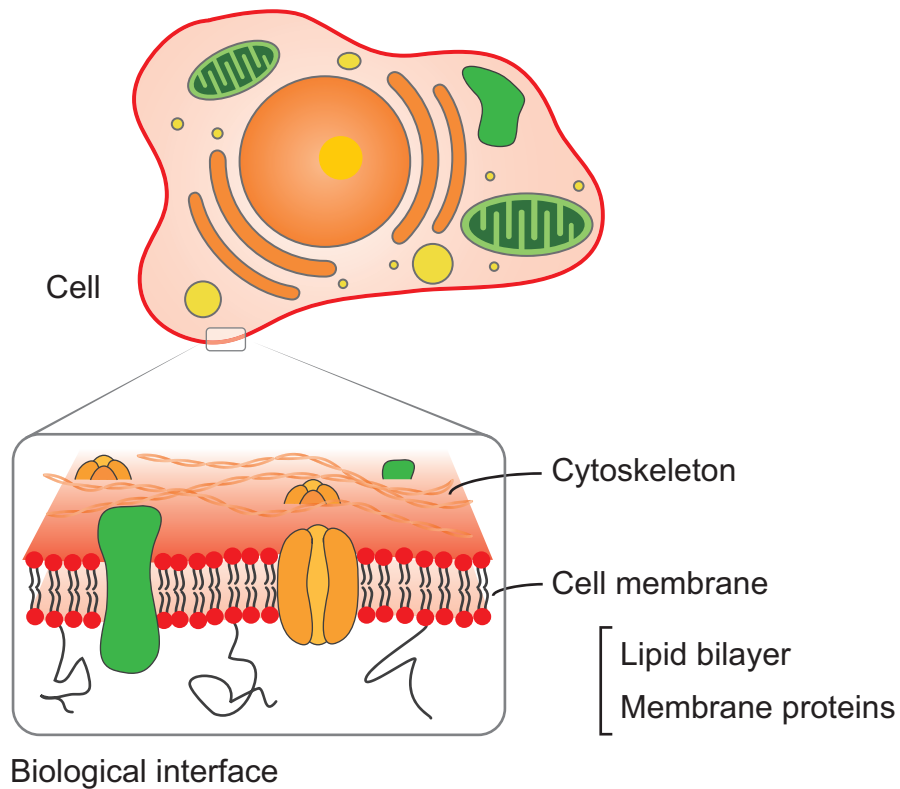


Figure 1.1: Schematic illustration of a biological interface.

Life is composed of micrometer-scaled minimal unit, which is called “cell”. The internal and external spaces of this unit of life are separated by a membrane structure, called a cell membrane, mostly composed of lipid molecules and membrane proteins. This biological interface can rapidly responds to the concentrations of internal and external substances and/or mechanical changes in the internal and external situations, and serves a scaffold for the dynamic physiological phenomena such as expression of proteins, signal transduc-

tion, and membrane deformation. In other words, “living” state is maintained through the non-equilibrium phenomena in the cell membranes. To understand the non-equilibrium interfacial phenomena in biological interfaces from a fundamental viewpoint of physics sheds light on the question “What is life?” [1], which is one of ultimate intellectual interests of the human race, and potentially leads to the understanding of the mechanism of diseases, aging, death, and the quite efficient chemical-mechanical energy transduction of life phenomena as well.

Biological interfaces of cells are mainly consisting of two essential components: cell membrane and cytoskeleton (Fig. 1.1). Here, we introduce the detailed structures of these components and their biological functions to obtain the proper picture of biological interfaces in the following chapters.

1.1 Cell membrane

Cell membranes, or plasma membranes, play great variety of biological roles including compartmentalization of cytosol and extracellular matrix, signal transduction, substrates of various biochemical reactions such as energy transduction, passive and active transport between cytosol and extracellular matrix. Although the specific roles of the cell membranes are different in various cell types, the basic structure is universal among them. Therefore, the physical or material properties of cell membranes are expected to be understood in the universal framework, and are highly interesting subject from not only biology but also physics.

The basic structure of cell membranes is lipid bilayer¹, whose thickness is approximately 4–5 nm. Many membrane proteins are embedded in or connected to the lipid bilayer membrane. The mass ratio of the lipids and membrane proteins is approximately 50:50, and the number ratio of them is 50:1 [2]. In this section, we introduce the detailed species, structures, and functional roles of the membrane lipids and proteins contained in cell membranes.

Membrane lipids

Cell membrane contains a multitude of lipid species, in which phospholipids are the most abundant. Other lipid molecules are glycolipids, sphingomyelin, and sterols such as cholesterol in the case of animal cells. The molecular structure of a phospholipid is the combination of hydrophobic and hydrophilic groups. In the case of animal cells, the hydrophobic group is the combination of two different carbon chains. One of two chain is saturated without double-bonded carbons, while the other is unsaturated with double-bonded carbons. The double bond in the hydrocarbon chain behaves as a kink and results in the expansion of the effective volume of hydrophobic part. The hydrophilic part is any one of phosphatidylcholine (PC), phosphatidylethanolamine (PE), phosphatidylserine (PS), and phosphatidylinositol (PI). These species are different in steric effect and the electrostatic property. The number of the phospholipid species in a cell membrane of a single cell is 500–2000 in the case of a normal eukaryotic cell, and over 150 in a red blood cell, which is the most simplest cell. In a cell membrane of a single cell, there are approximately 10^9 lipid molecules.

¹Physical properties of pure lipid bilayer membrane are described in the next chapter in detail.

Membrane proteins

Whereas the lipid molecules construct the basic two-dimensional membrane, the membrane proteins embedded in or connected to play other key roles, *i.e.*, diverse biological functions. The membrane proteins have an amphiphilic property like a lipid molecule. They can be classified according to whether the connection to the cell membrane is permanent or temporal. The connections are achieved by the hydrophobic interaction between the inside hydrophobic part of the lipid bilayer membrane and that of the membrane proteins; The membrane proteins embed their hydrophobic group, *e.g.*, a single or multiple penetrations of α -helix, β -sheet, β -barrel, or hydro carbon chains implemented by covalent bond to the proteins into the cell membrane. A rich variety of the biological functions of these membrane proteins are, for example, signal receptors, enzymes, transporters of ions, membrane-binding proteins that locally regulate the membrane curvature and the cell shape, bridges between the cell membrane and the cytoskeleton, which is introduced in the next section in detail, and so on. These proteins often cooperate their protein expressions and biological functions with each other, and locally and globally organize the cellular dynamic deformation and live responses.

Fluid mosaic model

The cell membrane composed of the lipid bilayer membrane and the membrane proteins have the physical properties of incompressible two-dimensional liquid. This picture, in which the membrane proteins freely float and diffuse on the two-dimensional sea of lipids, is called “fluid mosaic model” [3]. In fact, the lateral movement of lipid molecules and membrane proteins in the cell membrane have been verified by the fusion of two differently-labeled cell membranes [4], fluorescence recovery after photobleaching (FRAP), and single molecule tracking techniques [2]. This is because the cell membrane structure is softly sustained by the weak non-covalent lipid-lipid, lipid-protein, and protein-protein interactions such as van der Waals interaction, electrostatic interaction, and hydrophobic interaction. However, according to the following experimental progresses, the cell membrane have been proven to have laterally heterogeneous structure with liquid-ordered patchwork domains, rather than freely diffusive homogeneous two-dimensional liquid.

Dynamic heterogeneous structure

The cell membranes not only separate internal and external solutions but also behave as a microscopic functional platform through the formation of laterally-heterogeneous small domains, whose diameter is of the length scale of 2–20 nm, enriched in cholesterol, sphingolipids, glycolipids, GPI-anchored proteins, and transmembrane proteins [5,6]. After the first proposal of this lipid raft hypothesis in 1997 [7], in recent years, strong evidences for the existence of highly dynamical structure of this micro domain in cell membranes have been reported [8–11]. However, the driving forces of the lateral segregation and the mechanism of the coordination of this dynamic process are still a matter of debate.

1.2 Cytoskeleton

Living cells actively and precisely regulate their interfacial shapes, as they spontaneously deform in their living processes such as cell motility and cell division, or they deform in

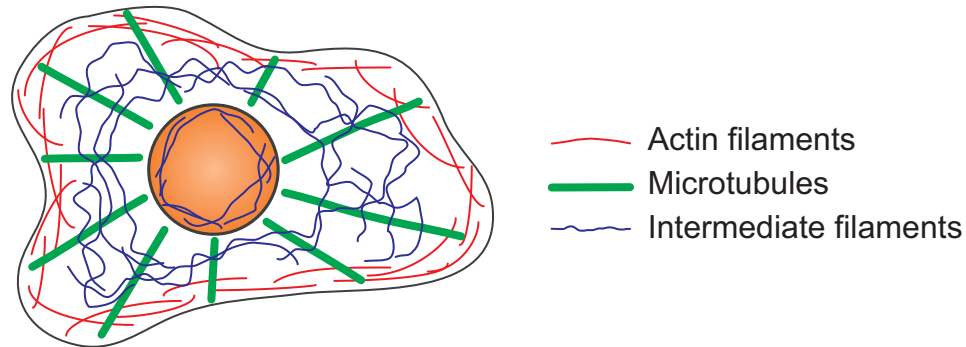


Figure 1.2: Schematic illustration of the three typical types of cytoskeletal filaments in a cell. Actin filaments (red), microtubules (green), and intermediate filaments (blue).

response to the changes in the external environment such as substance concentrations. In living cells, such active-shaping functions are realized by the filamentous proteins, called cytoskeleton, which mechanically sustains and determines the shapes of biological interfaces. Well known cytoskeletal proteins are three families of protein filaments, actin filaments, microtubules, and intermediate filaments, with different mechanical properties and stabilities (Fig. 1.2). These protein filaments not only resist to the mechanical stresses but also actively rearrange their architectures through the cooperation with hundreds of binding proteins that help to form network nodes with various bond angles and to actively generate forces as well. Particularly, the force generation is performed by adenosine-triphosphate (ATP) hydrolysis of the specific binding proteins called molecular motor proteins, such as myosin, kinesin, dynein, etc. In this section, we explain the properties of these biopolymers and the related accessory proteins with their physiological roles.

1.2.1 Actin filaments

Spatiotemporal distribution and structure formation of actin are generally important factors for the determination of the cell shape. In fact, the amino acid sequence of the actin protein is conserved about 90% in most eukaryotic cells. Actin subunits, which are monomeric actin proteins called globular actin or G-actin, assemble into actin filaments, through the self-association by weak non-covalent interaction. The actin filaments are called F-actin, whose diameter is 8 nm and the persistence length, *i.e.*, correlation length of filamentous bending caused by thermal fluctuation, is 9–18 μm [12]. Since single G-actin has polar and chiral properties, the self-assembled structure, F-actin, also has such properties with the defined plus end and minus end and right-handed helicity. The polymerization and depolymerization of the filamentous structure by the self-association and dissociation of the small subunits are essential for the dynamic remodeling of actin cytoskeleton in the cytosol, because the diffusion or transportation of long filaments is difficult in such a viscous and crowded environment. In living cells, thick filament structure with higher stiffness, called actin bundles, and gel-like network structure can be seen as a result of the higher-order self-association of actin filaments. In these cases, again, the association and dissociation of G-actins at the plus and minus ends allow the rapid rearrangement of the higher-order structures.

Actin binding proteins

Whereas the fundamental physical behavior of the polymerization/depolymerization have been investigated through the intensive *in vitro* experiments with varied conditions of monomer concentration, pH, ATP concentration, and salt concentration, it is known that, in addition to these factors, the numerous actin binding proteins interact with G-actin and F-actin to organize the higher-order spatiotemporal structures. For example, fimbrin and α -actinin form a bridge between two filaments in parallel, and these cross-linkings promote the bundling of actin filaments. On the other hand, filamin forms a bridge between two filaments at a right angle, and eventually forms the gel-like sheet structure, known as “lamellipodia” seen in the cellular movement on a substrate. While these actin binding proteins function through the connection to F-actins, formins are dimeric proteins that interact with G-actins to enhance the nucleation rate of actin polymerization. Also, Arp2/3, the complex of actin related protein 2 and actin related protein 3, interacts with G-actins and enhances the nucleation rate. Arp2/3 complex, which locates at the minus end of a nucleated filament, further connects to another F-actin filament at an angle of 70° , leading to the formation of a tree-like extended network. Formins and Arp2/3 complexes accelerate the polymerization of G-actins beneath the cell membrane, and form shell-like structure, called actin cortex, that directly determines the interfacial shape and its movement. Although the factors that are involved in the connection between the cell cortex and the cell membrane are not completely revealed, it has been clarified that ERM (ezrin, radixin, and moesin) protein families play key roles for the connections between F-actin and transmembrane proteins.

Motor protein

The most famous actin binding proteins are myosin family, which are molecular motor proteins. Myosin molecule is composed of head and tail parts. The head part interact with F-actin, and undergoes conformational changes together with ATP hydrolysis, resulting in the repeatable unidirectional sliding motion of the actin filament. This repeatable sliding is called power stroke of myosin. The complex of F-actin and myosin is so-called actomyosin. Particularly in myosin family, the structure of myosin II is comprised of the coiled-coil of two long chains, called heavy chains, and the large head parts, which interact with actin filaments, are connected to N-terminal of the chains. Such myosin II dimers further assemble into the higher-order structure, called bipolar thick filament, through the weak attraction among hundreds of coiled-coil heavy chains. In the well-known structure of sarcomere in muscle cells, the bipolar thick filaments generate the contractile force by sliding the actin filaments systematically aligned in parallel to the opposite directions. In non muscle cells, the contractile force generated in the actomyosin complex contributes to other important biological behaviors such as membrane deformation for cell motility, contractile ring during cell division, stress fibers involved in the shape determination of a cell that adheres onto a substrate, and so on. Other types of myosin, myosin I, myosin III, myosin V, and so on, are engaged in other functions, endocytosis, organelle transportation, etc., for intracellular organization.

1.2.2 Microtubules

Microtubules have similar properties with actin filaments: polar subunits, polar filaments, and polymerization/depolymerization together with GTP hydrolysis. However, the mechan-

ical property of microtubules is very different from actin filaments because the subunits of microtubules, tubulins, assemble into hollow cylinder-like filaments with many interaction sites via the intermediate called protofilaments composed of 13 tubulins. Thus, the outer diameter is larger, 25 nm, than that of an actin filament, and the much longer persistence length of microtubules reaches even 5 mm [12], which is much longer length scale than the single cell size. Due to the mechanical rigidity of the microtubules, the breakage in the middle of a filament is energetically-unfavorable, nevertheless the dynamic remodeling of the filament is allowed thanks to the tubulin polymerization/depolymerization at the plus/minus end.

Motor proteins

The molecular motor proteins that couple to the microtubules are kinesin family and dynein family. They move on the microtubule unidirectionally through the conformational changes with using chemical energy obtained from ATP hydrolysis. Most of kinesin family walk toward the plus end of the filament, while dynein family toward the minus end. In cells, kinesin and dynein contribute to the intracellular transportation of cargoes like organelles and vesicles by walking along the microtubules that run throughout the cytosol. Dynein is also involved in the active beating of cilia and flagella.

1.2.3 Intermediate filaments

Intermediate filaments are helical filaments without subunits, and thus there are diverse cytoskeletal proteins compared to actin and tubulin. For example, lamins in nuclei, keratin filaments in epithelial cells, and neurofilaments in nerve cells are well-known. Each kind of intermediate filament in cytosol serves mechanical stiffness to each cell in different tissues.

1.2.4 Spectrin

Spectrins are filaments that locate beneath the cell membrane of a red blood cell. They are bounded to the cell membrane via short (30–50 nm in length) actin filaments, other proteins, band 4.1, adducin, and tropomyosin, or transmembrane proteins, glycophorin, and band 3 protein. The whole structure of the network underlying the membrane is highly-coordinated two-dimensional hexagonal lattice, whose internode flexible links are composed of spectrin tetramer with two α -chains and two β -chains, which are 80–100 nm in the length [13, 14]. Thanks to the flexibility and stiffness of this spectrin cytoskeletal network against shear deformation, red blood cells can restore the original biconcave shape after passing through the micro-capillary vessels in our microcirculatory system whose vessel diameter is considerably smaller than the size of a red blood cell.

Chapter 2

Reconstitution of biological interfaces

Toward understanding of the essences of cell-shape determination and active deformation of the cell membrane induced by the interaction with cytoskeleton and motor proteins, intensive experiments using reconstituted systems with only small number of components involved in the shape determination and the deformation have been conducted so far. These types of experimental systems include artificial lipid bilayer vesicles (liposomes), lipid monolayers surrounding water-in-oil (W/O) droplets, protein solution within a solid small compartment like poly(dimethylsiloxane) (PDMS), actively-driven cytoskeleton on a solid substrate in the presence of motor proteins attached onto the substrate, and so on. Particularly, liposomes and W/O droplets have deformable lipid interfaces which resemble the fundamental structure of cell membranes. In this chapter, we review these two reconstituted systems with deformable interfaces and their achievements up to the present.

The deformable reconstituted systems are based on the container made of lipid bilayer or lipid monolayer interfaces, which are formed as the hierarchical higher-order structures of self-assemblies of lipid molecules as the lipid bilayers of the cell membranes are realized. First, we explain the molecular properties of lipids, especially phospholipids as the most abundant components, and their hierarchical structure formations.

2.1 Phospholipids

The major element of the cell membranes is phospholipid molecules. Phospholipids can be classified roughly into two groups, glycerophospholipids with the basic skeleton of glycerol or glycerine and sphingophospholipids with the basic skeleton of sphingosine, both of which are the crucial elements for the cell membranes. Phospholipid are amphiphilic molecules that have both hydrophilic group and hydrophobic, or lipophilic, group within a single molecular structure. A hydrophilic group of phospholipids is composed of polar head group, which is an electric dipole with negatively charged phosphate group and, in most cases, positively charged polar group in an aqueous solution. A hydrophobic groups of phospholipids are further composed of two fatty acid chains (hydrocarbon chains). The length of the chains is about 2–4 nm. Figure 2.1 shows the molecular structures of typical glycerophospholipids, dioleoyl-phosphatidylcholine (DOPC) and dioleoyl-phosphatidylserine (DOPS), and the schematic of a phospholipid with head polar group and two hydrocarbon chains.

A particularly important property of phospholipids is the size ratio between hydrophilic

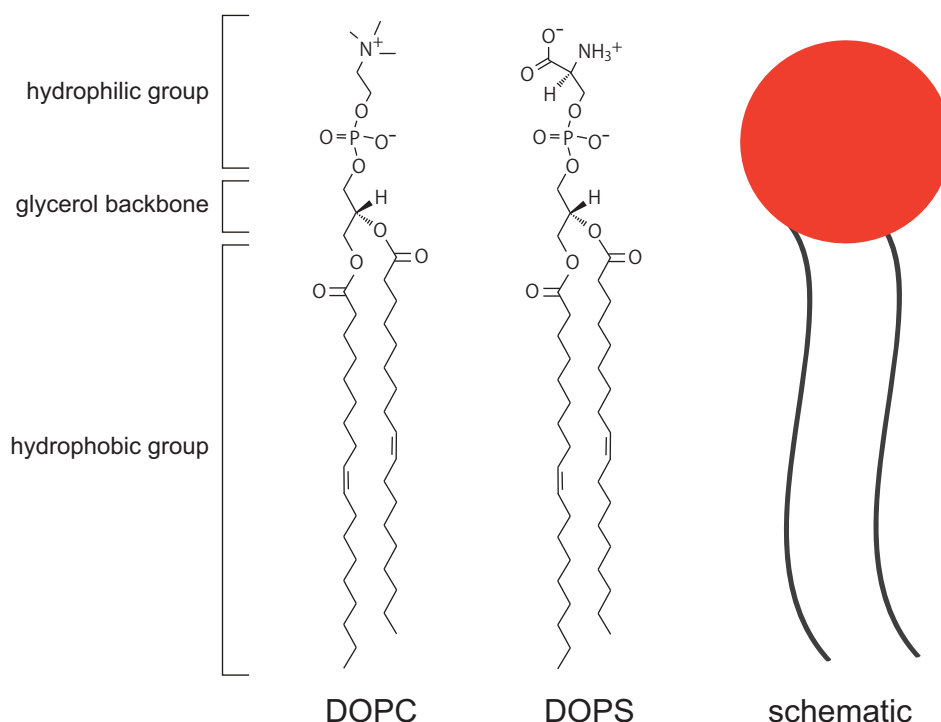


Figure 2.1: Molecular structures of phospholipids, dioleoyl-phosphatidylcholine (DOPC) and dioleoyl-phosphatidylserine (DOPS). A single phospholipid molecule contains both hydrophilic and hydrophobic groups and act as a surfactant. A phospholipid is frequently represented by one “head” and two “tails” as shown in the schematic (right).

group and hydrophobic group. This size balance, also called hydrophilic lipophilic balance (HLB), strongly influences their higher order structure formation we describe in the next subsection. The size of hydrophilic group is determined by the kind of a polar group. There are many kinds of polar groups, *e.g.*, choline group, ethanolamine group, serine group, glycerol group, and inositol group. For the polar group of phospholipids, they are called like phosphatidylcholine (PC), phosphatidylethanolamine (PE), etc. On the other hand, the size of hydrophobic group is characterized by the lengths of hydrocarbon chains and their steric behaviors. The important factors are the ratio $m : n$, where m is the number of carbon atoms and n is the number of unsaturated bondings among them. For example, the structural property of oleyl chain of DOPC or DOPS is represented as 18:1, namely eighteen carbons atoms and one double bonding. In general, according to the increases of m and n , the corresponding hydrocarbon chains becomes longer and creates more kinks, resulting in the increased steric volumes and hydrophobicity. Note that there is energy loss of approximately $0.7k_B T$ per a carbon atom in water. In the case of glycerophospholipids of cell membranes, the chain lengths are roughly in the range of 10–20, and unsaturated fatty acid chain is connected to the second position of glycerol skeleton.

2.2 Hierarchical structure of phospholipids

Lipid molecules, whose total length is 2–4 nm, self-assemble into hierarchical ordered structure in the wide range of the length order of nm– μ m. This intermediate length scale in

between atomic or molecular scale (from Å to nm) and macroscopic scale (longer than mm, in which we can see and touch in our lives) is called mesoscopic scale. The various hierarchical structures of lipid molecules are just in this mesoscopic length scale, and the detailed structures exhibit various phases and behaviors depending on the constitutive lipid species, their concentrations, solute conditions, and surrounding temperature.

Figure 2.2(a) shows a schematic illustration of a spherical aggregate called micelle. This type of structure is realized by self-assembling of hydrophobic groups and directing the hydrophilic groups toward the outside aqueous phase, as if they hide their hydrophobic parts from water. Lipid molecules are dissolved and dispersed in the solution if the lipid concentration is below critical micelle concentration (CMC), whereas they form aggregate structure, micelles, if the concentration is over CMC. Figure 2.2(b) shows a schematic illustration of an inverted micelle (or reverse micelle), which hydrophilic parts are hidden from surrounding organic phase in the cases that the bulk solution is oil or organic solvent. When the lipid concentration is further increased, tubular micelles, disk micelles, and hexagonal phase via hexagonally-stacking of tubular micelles appear. Figure 2.2(c) and (d) represent a lipid monolayer membrane we see at oil/water interfaces and a lipid bilayer membrane in water phase, respectively. These two structures form two-dimensional soft interfaces.

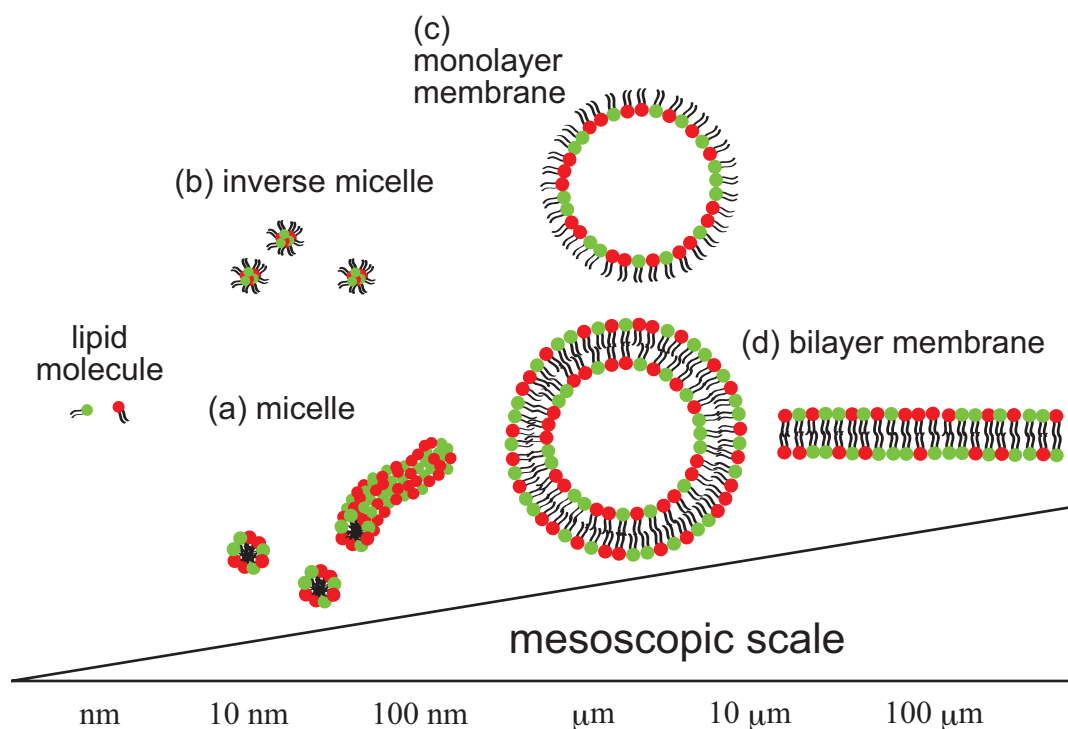


Figure 2.2: Schematic illustrations of various typical higher order structures of phospholipids in solutions: (a) micelle, (b) inverse micelle, (c) monolayer membrane, and (d) bilayer membranes (closed vesicle and plane membrane).

As indicated in the above paragraph, it is known that the higher-order structure formation of lipid molecules depends on the temperature and molecular concentration. As a

reference, we show the phase diagram of the various higher-order structures in figure 2.3.

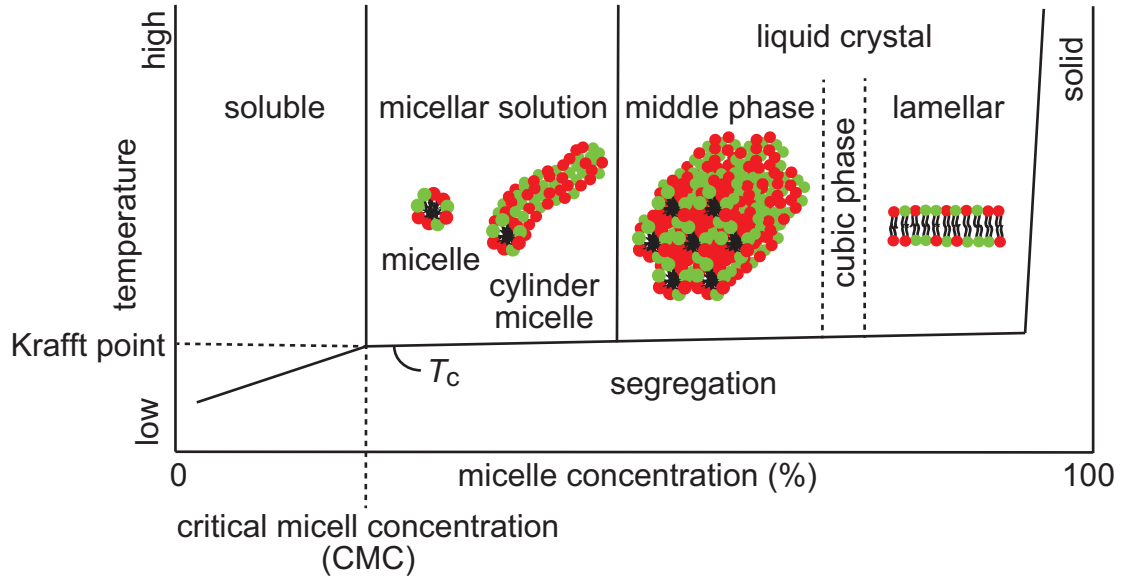


Figure 2.3: Phase diagram of water-surfactant system

In addition to the lipid molecule concentration and temperature, such structure formations are also affected by the steric balance between the hydrophilic group and hydrophobic group of a lipid molecule, as we describe in the previous subsection. Israelachvili *et al.* indicated that the higher-order structure formation through the self-assembly of an amphiphilic molecule can be generally understood by the packing parameter v/la , where v is the volume effectively occupied by acyl chains, l is the chain length, and a is the cross-sectional area of hydrophilic group (see a review book in detail [15]). Due to the geometrical constraints determined by the packing parameter, lipid molecules form spherical micelles for $v/la < 1/3$, tubular micelles for $1/3 < v/la < 1/2$, bilayer membranes for $1/2 < v/la < 1$ in aqueous phase, while they form inverse micelles, hexagonal II phase, etc. for $1 < v/la$ in organic phase. This geometrical effect is summarized in Figure 2.4.

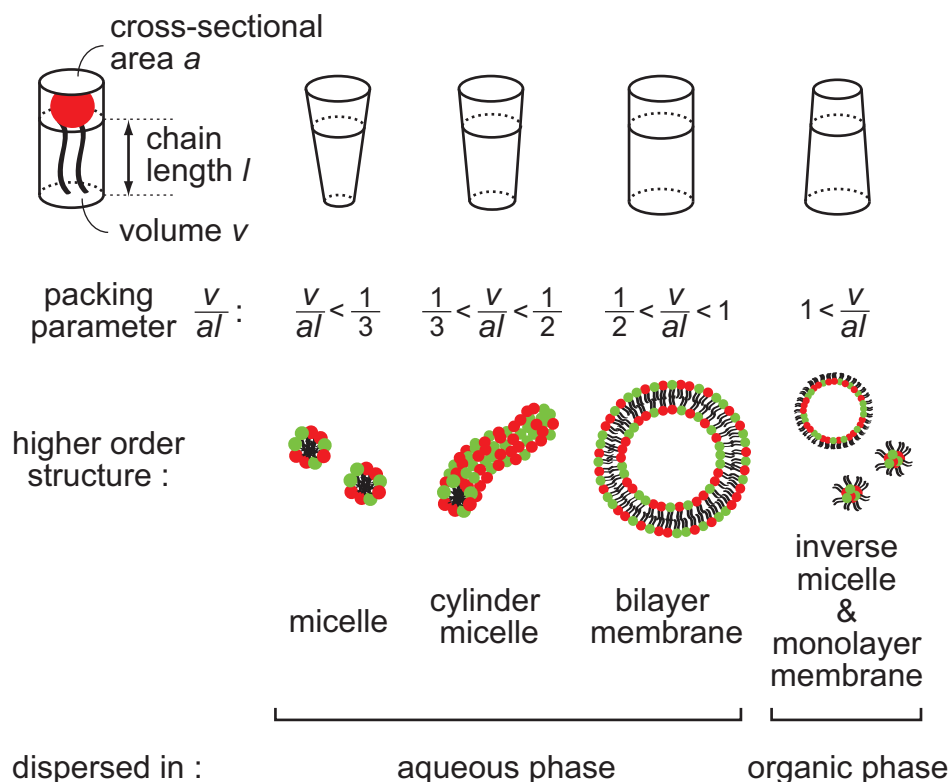


Figure 2.4: Packing parameter of an amphiphilic molecule and corresponding optimal higher order structures in aqueous and organic solutions.

2.2.1 Lipid monolayer

In the two-phase solution with organic (oil) phase and aqueous phase, the amphiphilic property of lipid molecules sorts them at the oil/water interfaces to reduce the interfacial free energy between oil and water. If a water droplet exists in oil, for example, the droplet is covered with lipid monolayer like an inner leaflet of a lipid bilayer vesicles as shown in Figure 2.5.

In the experiments, we can control the size of the droplet and that of interface ranging from nm to $sub-mm$. Whereas the microfluidic techniques [16–18] or vortex-mixing [19] may provide a relatively systematic way to control the droplet size, the easiest experimental method to control the droplet size is micropipette mixing. In this method, by dispersing initially macroscopic water droplets in oil phase dissolving lipid molecules by repeated micropipette suction and discharges, various sized W/O droplets can be obtained. In fact, there are many experiments that utilize μm -scaled W/O droplet system made by the method with micropipette as a model system mimicking the inner leaflet of biological membranes [20–23]. Inside the cell-sized spatial confinement, the higher ratio between surface area and volume of a system serves strong two-dimensional interfacial effects in general. As examples of the emergence of these interfacial effects, some biopolymers, DNA, actin proteins, cell-free translation system to synthesize GFP confined within the cell-sized W/O droplets with phospholipid monolayer exhibit different behaviors in their spatial distribu-

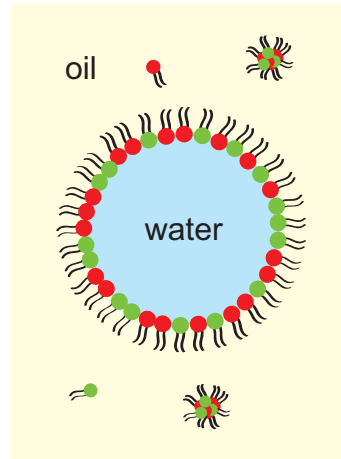


Figure 2.5: Schematic illustration of a water-in-oil (W/O) droplet covered with lipid monolayer membrane. Typical diameter is ranging from 10 nm (nano/micro-emulsion) to 100 μm (cell-size or bigger). In the surrounding oil phase lipid molecules and/or its aggregates (inverse micelles) are sometimes dispersed.

tions, conformations, expression of GFP, and so on [19, 21–23].

2.2.2 Lipid bilayer

In aqueous phases, lipid molecules often form two dimensional structure called lipid bilayer membranes, in which the hydrophobic groups of the lipid molecules are hidden from the aqueous phase. There are two kinds of typical lipid bilayer membranes: plane structure (lamellar) and closed structure (vesicle). Figure 2.6 shows a schematic illustration of a lipid bilayer vesicle, which is also called a liposome.

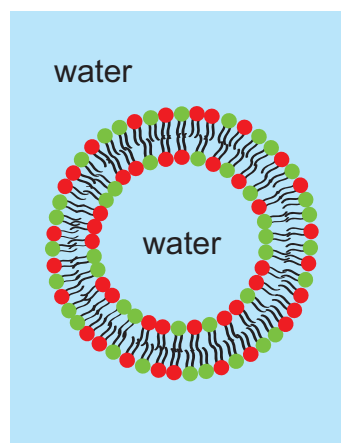


Figure 2.6: Schematic illustration of a lipid bilayer membrane vesicle, which is so-called liposome. As is the case of lipid monolayer, the typical diameter is ranging from 20 nm to 100 μm , and the address term depends on the size (see text for details).

A fragment of planar lipid bilayer exposes the hydrophobic groups at the edge of the membrane, at which they lose system free energy, mainly by the decrease in the entropy of surrounding water molecules. This is indeed the origin of the “hydrophobic interaction”. Therefore, to avoid the loss of system free energy, this lipid bilayer sheet spontaneously forms closed spherical structure, *i.e.*, vesicle, in general. The free energy loss by the line tension γ (unit of energy per unit length) at the edge of a lamellar fragment can be approximately written as $E_{\text{edge}} \sim 2\pi R_l \gamma$, where R_l is the characteristic length scale of the fragment. On the other hand, when the planar sheet transforms into a spherical vesicle, this shape change costs bending energy $E_{\text{bend}} = 8\pi\kappa$, where κ is bending stiffness (unit of energy), instead of the dissolution of the line tension E_{edge} . Assuming the constant surface area during the shape change, the smallest vesicle size can be estimated as $R_{\text{min}} \sim 2\kappa/\gamma$ by the balance of these two energies. For typical values of these parameters $\kappa \sim 1 \times 10^{-19}$ J and $\gamma \sim 1 \times 10^{-11}$ J/m for phospholipid bilayers, the typical smallest size of them is 20 nm.

Lipid bilayer vesicles are classified according to their diameter: small unilamellar vesicle (SUV) for 20 nm–100 nm in diameter, large unilamellar vesicle (LUV) for 100 nm–1 μm , and giant unilamellar vesicle (GUV) for larger than 1 μm . These names are used for a vesicle composed of a single lipid bilayer membrane; lipid bilayer vesicles composed of multiple bilayer membranes, like onions, are called multilamellar vesicle (MLV). Note that MLV was the first vesicle structure founded by Bangham *et al.* [24] in the history of the researches on artificial lipid bilayer vesicles introduced here.

GUVs with diameter of tens of μm resemble cell membranes in their size and basic structure [3], they have been intensively used and considered as model cell membrane systems in experimental, theoretical, and numerical investigations. In the experiments, the most basic way to prepare GUVs is swelling method such as natural swelling (gentle hydration) method or electroformation method. In the physicochemical investigations, shape deformation, shape fluctuation, and lateral phase separation in multi-component vesicles have been particularly focused on. As is the case with the W/O droplet systems, GUVs have been frequently adopted for cell-mimicking systems with both inner and outer leaflet of basic lipid bilayer structure. After the numerous investigations on the fundamental physicochemical behaviors of pure lipid bilayer GUVs, further studies on the interactions between lipid bilayer membrane and some external additives, *e.g.*, surfactants [25, 26], colloids [27–30], biological polymers [31, 32], and proteins [33–37] have been started. For instance, membrane budding and deformation like tubular protrusion, heterogeneous accumulations of the added substances have been confirmed in these systems. Although these additives induce wide spectrum of membrane responses in different ways, the observed phenomena were interpreted from different chemical and physical viewpoints in each experiment, and systematic knowledge have not yet been acquired up to now. However, for widely known and biologically important several proteins, *e.g.*, cytoskeletal proteins, a certain amount of knowledge and experimental techniques have been accumulated and established. It is a highly interesting open question that how and how much the revealed phenomena in these reconstituted systems actually work in the living cells.

Chapter 3

Fluctuation and deformation of soft interfaces

The biological interfaces and the artificial model interfaces we described in the earlier chapters are soft and deformable interfaces sustained by the weak non-covalent attractions among their elements. The emergent nature of their shape fluctuation and the deformation reflects the physical properties of these interfaces and the surrounding environments. Here, the word “fluctuation” means the phenomena that the interface temporally undergoes a shape change around the mean shape, independent of whether the driving force of the motion is thermal or athermal. Moreover, as another type of general shape changes, the mean shape itself can change in response to the changes in area/volume ratio of closed membranes and/or the applications of external forces. We call this phenomenon “deformation”. For the model lipid bilayer membranes, thermal fluctuation (Brownian motion) of the membrane and the various conformational deformation that correspond to a specified area/volume ratio have been well studied. Starting from the physical properties and descriptions of these fluctuation and deformation of pure lipid bilayers, those of living cells have been investigated. In this chapter, we introduce the fundamental physical setups before we enter the main contents of this thesis.

3.1 Bending energy

Let us characterize the deformed shape of a lipid membrane by mathematical formulae. In general, we have to consider three types of elastic energies when a quasi-two-dimensional elastic sheet ¹ deforms: bending energy F_{bend} , stretching (or compressing) energy F_{stretch} , and shear elastic energy F_{shear} . In the case of pure lipid bilayer membranes, shear elastic energy F_{shear} can be neglected due to the high lateral fluidity of lipid molecules within the membrane. Further, the stretching/compressing elastic energy of the lipid membrane is much larger than the bending energy, and thus the surface area per each lipid molecule is kept constant during the membrane deformation. Therefore, the stretching energy F_{stretch} is also not involved in the shape changes of the membrane, and the lipid bilayer undergoes conformational changes as incompressible two-dimensional fluid. For the above reasons,

¹Here we call a three-dimensional elastic body whose characteristic length of one dimension, *e.g.*, z -direction, is much shorter than those of the other two dimensions, *e.g.*, (x, y) -plane, as quasi-two-dimensional “sheet”. Thus, a micrometer-scaled lipid bilayer membrane with the thickness 4–5 nm can be treated as an elastic sheet.

conformational changes of a pure lipid bilayer membrane is determined only by bending energy [38–40]. To describe a mathematical formulae for the elastic energy, the lipid bilayer membrane is usually treated as a continuum body, as far as we consider usual shape changes of the membrane in the length scale much larger than that of cross-sectional length of a lipid molecule, *i.e.*, 1 nm. In this theory, the parameters that characterize a conformational state of an elastic sheet are two principal curvatures C_1 and C_2 (see Fig. 3.1), which are the eigenvalues of the second order differential of the surface-shape function. Using these

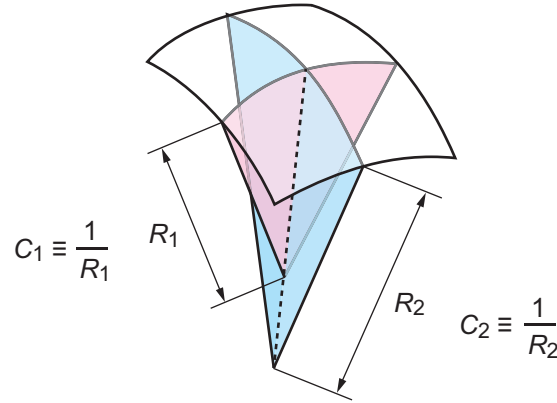


Figure 3.1: Schematic of the two local curvatures C_1 and C_2 that locally characterize a curved surface. The local curvature C_1 and C_2 are defined as the inverse of local curvature radii R_1 and R_2 , respectively.

parameters, mean curvature H and gaussian curvature K as two geometric invariants are obtained:

$$H \equiv \frac{C_1 + C_2}{2} \quad (3.1)$$

$$K \equiv C_1 C_2. \quad (3.2)$$

For small deformation, local bending energy for a deformed elastic membrane can be written by the expansion up to quadratic terms as

$$f = \frac{\kappa}{2}(2H - C_0)^2 + \kappa_G K, \quad (3.3)$$

where κ and κ_G are bending stiffness and Gauss bending stiffness, respectively, and both have the dimension of energy. Bending stiffness κ for various kinds of lipid membranes have been systematically measured through the experiments of micropipette aspiration by Evans *et al.* [41–43] and evaluation of membrane fluctuation (flicker spectroscopy) we discuss later. The measured typical values for phospholipid bilayer membranes are of the order of 10^{-19} J. The constant C_0 is spontaneous curvature introduced by W. Helfrich [39], which is an intrinsically optimal curvature determined by the components of inner and outer leaflets of the bilayer membrane. If both leaflets have the same homogeneous lipid compositions, C_0 becomes 0.²

²the simplest model introduced by P. B. Canham [38]

The closed lipid bilayer vesicle have the conformation that the surface integral of the local bending energy:

$$F = \frac{\kappa}{2} \int_A dA (2H - C_0)^2 + \kappa_G \int dA K, \quad (3.4)$$

where $\int dA$ represents the surface integral over the entire surface of the vesicle. The second term, integral of Gaussian curvature $\kappa_G \int dA K$, is topological invariant because of Gauss-Bonnet theorem [44]. For the topology-invariant deformation, the integration reads $\kappa_G 4\pi(1-g) = \text{const.}$, where g , called genus, is the number of handles or holes of the vesicle conformation. Therefore, we can ignore Gauss curvature energy by formally setting $\kappa_G = 0$ as long as the conformational topology is the same. Here, the constraints for the minimization of Eq. (3.4) are constant surface area A and constant volume V of the vesicle. Assuming no molecule enters or exits the membrane, the surface area of the incompressible two-dimensional fluid membrane is kept constant as discussed above. In addition, the internal solution enclosed by the vesicle is generally incompressible. In this situation, the inner volume can vary only by the enter or exit of water molecules across the membrane, namely osmotic effect. Assuming that the volume V is variable due to the osmotic effect, the osmotic pressure

$$\Pi \equiv R_g T (n/V - c), \quad (3.5)$$

where R_g is gas constant, T is absolute temperature, n is mole number of the osmotically active agents inside the volume, and c is the total mole concentration of the agents in the system, generates an additional increase in the osmotic energy:

$$F_{\text{osm}}(V) \equiv - \int_{V_0}^V dV' \Pi(V') \approx \frac{R_g T c V_0}{2} \left(\frac{V}{V_0} - 1 \right)^2, \quad (3.6)$$

where the $V_0 \equiv n/c$ is the optimal inner volume with the mole-concentrations matching. Note that here the signature is taken positive when the vesicle volume increases, and the last approximation is valid when $V/V_0 - 1 \ll 1$. Because of $R_g T c V_0 / 2 \sim 10^7 \kappa \gg \kappa$ for typical $c \sim 1 \text{ mM} = 1 \text{ mol/m}^3$ and $V \sim (10 \mu\text{m})^3$, the vesicle volume during the conformational changes by bending elasticity is effectively kept at $V = V_0$ [45].

However, the typical vesicle deformation like budding cannot be explained by the simple bending energy Eq. (3.4). This discrepancy is originated from the ‘‘bilayer’’ effect that the actual lipid bilayer has the additional degree of freedom in each inner and outer leaflet possibly coupled to the local curvature. This effect can be included in the theoretical model as the additional local curvature energy by considering the quadratic potential for the small differences in local molecular densities of the two leaflets under the constraints on the surface area and each molecular number in the two leaflets [46–48]. In this theory, which is called area-difference elasticity (ADE) model, the eventual parameters for the closed vesicle conformation become an area/volume ratio and an area difference between the inner and outer leaflets [49]. The results from ADE model can explain a wide spectrum of vesicle conformations observed in the experiments under various conditions. Both ADE model and the simplified bending energy model (Eq. (3.4)) are now widely accepted to discuss the quasi-static conformational deformation of lipid bilayer membranes.

3.1.1 Derivation of bending energy from theory of elasticity

Whereas we introduced bending energy Eq. (3.4) from the argument on two small principal curvatures C_1 and C_2 , it is also derived from more general argument in the theory of elas-

ticity, under assumption of the quasi-two-dimensional sheet as a continuum body. To enter the derivation, we first define strain tensor u_{ij} and stress tensor σ_{ij} , where i and j represent the (x, y, z) -axis in Cartesian coordinate $\{\mathbf{e}_x, \mathbf{e}_y, \mathbf{e}_z\}$.

Strain tensor

Let us set the position vectors

$$\mathbf{r} = \begin{pmatrix} x \\ y \\ z \end{pmatrix}, \quad \mathbf{r}' = \begin{pmatrix} x'(x, y, z) \\ y'(x, y, z) \\ z'(x, y, z) \end{pmatrix}, \quad \mathbf{u} \equiv \mathbf{r}' - \mathbf{r}, \quad (3.7)$$

which represent the positions of a body element before and after deformation, and displacement field respectively. Let \mathbf{r} and $\mathbf{r} + d\mathbf{r}$ be the positions close to each other, and \mathbf{r}' and $\mathbf{r}' + d\mathbf{r}'$ be those after the deformation. Since $du_i = \frac{du_i}{dr_j} dr_j$, the squared distance during the deformation is³

$$(d\mathbf{r}')^2 - (d\mathbf{r})^2 = \left(\frac{\partial u_i}{\partial r_j} + \frac{\partial u_j}{\partial r_i} + \frac{\partial u_k}{\partial r_i} \frac{\partial u_k}{\partial r_j} \right) dr_i dr_j. \quad (3.8)$$

In this formula, we define strain tensor u_{ij} as

$$(d\mathbf{r}')^2 - (d\mathbf{r})^2 = 2u_{ij} dr_i dr_j \quad (3.9)$$

$$u_{ij} \equiv \frac{1}{2} \left(\frac{\partial u_i}{\partial r_j} + \frac{\partial u_j}{\partial r_i} + \frac{\partial u_k}{\partial r_i} \frac{\partial u_k}{\partial r_j} \right). \quad (3.10)$$

Note that the strain tensor u_{ij} is symmetric tensor:

$$u_{ij} = u_{ji} \quad (3.11)$$

for all i and j .

Stress tensor

Next, we consider the forces acting on the elastic body, which can be classified as ‘‘volume force’’ \mathbf{G} and ‘‘surface force’’ \mathbf{F} . Assuming that the volume force can be described by the summation of those contribute to all the volume elements, it becomes

$$\mathbf{G} = \int_V \mathbf{g} dV, \quad (3.12)$$

where \mathbf{g} is the force per unit volume and $\int_V dV$ denotes the volume integral over entire volume of the body. On the other hand, the surface force comes from the net internal forces which eventually acting on the surface of the body by Newton’s third law as

$$\mathbf{F} = \int_A \mathbf{f} dA, \quad (3.13)$$

³Here we use Einstein summation convention.

where \mathbf{f} is the surface force density and $\int_A dA$ denotes the surface integral over entire surface of the body. If we consider the forces acting on an arbitral small element, the net surface force \mathbf{F} should be zero, *i.e.*, balanced itself, because the volume force \mathbf{G} is negligible compared to the surface force \mathbf{F} in such a small dimension. Thus, the surface force f_i can be represented as

$$f_i = \sigma_{ij}n_j, \quad (3.14)$$

where σ_{ij} is called stress tensor and n_j is the normal vector to the surface⁴. The stress tensor σ_{ij} represent the stress component along e_i -direction acting on the surface perpendicular to e_j . It is non-trivial but the stress tensor σ_{ij} is also symmetric:

$$\sigma_{ij} = \sigma_{ji} \quad (3.15)$$

Using divergence thorem of Gauss, the total forces can be written as

$$\mathbf{G} + \mathbf{F} = \int_V (\mathbf{g} + \nabla \cdot \sigma_{ij}) dV, \quad (3.16)$$

where ∇ is here the differential operator in three-dimensional space. From this expression, the mechanical equilibrium condition in a static state of the body is obtained as

$$\mathbf{g} + \nabla \cdot \sigma_{ij} = 0. \quad (3.17)$$

Particularly, when there is no external volume forces, it reads $\nabla \cdot \sigma_{ij} = 0$.

Hookean elastic material

In a Hookean elastic material, thus under the assumption of small strain u_{ij} , the stress tensor σ_{ij} can be related to the strain tensor u_{ij} in the linear form:

$$\sigma_{ij} = \lambda u_{kk} \delta_{ij} + 2\mu u_{ij}, \quad (3.18)$$

where the material coefficients λ and μ are called the Lamé coefficients, and δ_{ij} is Kronecker delta, after considering all the symmetry of the tensors of rank two and invariance by change of coordinates [50]. Instead of (λ, μ) , by setting another set of material coefficients (E, ν) as

$$\lambda = \frac{E\nu}{(1+\nu)(1-2\nu)} \quad (3.19)$$

$$\mu = \frac{E}{2(1+\nu)}, \quad (3.20)$$

where E is Young's modulus and ν is Poisson's ratio, the linear relationship between the stress tensor σ_{ij} and the strain tensor u_{ij} (Eq. (3.18)) is also written as

$$\sigma_{ij} = \frac{E}{1+\nu} \left(u_{ij} + \frac{\nu}{1-2\nu} u_{kk} \delta_{ij} \right). \quad (3.21)$$

⁴This argument is usually done with an infinitesimal tetrahedral body.

Hookean elastic energy for a thin sheet

In a Hookean elastic material, the elastic energy E_{el} can be generally written as

$$E_{\text{el}} = \frac{1}{2} \int_V \sigma_{ij} u_{ij} \, dV, \quad (3.22)$$

which can be interpreted the work done by the stress σ_{ij} ⁵. Now we consider a thin sheet, whose thickness along z -axis h is much smaller than the lengths of (x, y) -plane (Fig. 3.2). In the case of a thin sheet, the normal stresses σ_{xz} and σ_{yz} , and the transverse stress σ_{zz} is

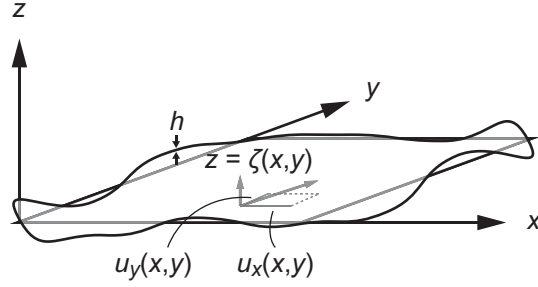


Figure 3.2: Schematic of a deviation of a planar sheet with small thickness h . The deviation along z -direction is represented by out-plane deflection $\zeta(x, y)$.

smaller than the other in-plane stresses [50], because of the stress-free boundary conditions at the upper and lower surface:

$$\sigma_{xz}(x, y, \pm \frac{h}{2}) = \sigma_{yz}(x, y, \pm \frac{h}{2}) = \sigma_{zz}(x, y, \pm \frac{h}{2}) = 0 \quad (3.23)$$

and thus

$$\sigma_{xz}(x, y, z) \simeq \sigma_{yz}(x, y, z) \simeq \sigma_{zz}(x, y, z) \simeq 0 \quad (3.24)$$

in the vicinity of these stress-free boundaries $-\frac{h}{2} \leq z \leq \frac{h}{2}$. Therefore, the elastic energy for a thin sheet E_{es} is obtained by using Eq. (3.24) in Eq. (3.22) as⁶

$$E_{\text{es}} = \frac{1}{2} \int_V (\sigma_{xx} u_{xx} + \sigma_{yy} u_{yy} + 2\sigma_{xy} u_{xy}) \, dV. \quad (3.25)$$

Substituting Eq. (3.21), it reads

$$E_{\text{es}} = \frac{E}{2(1-\nu^2)} \int_V [(u_{xx} + u_{yy})^2 - 2(1-\nu)(u_{xx}u_{yy} - u_{xy}^2)] \, dV. \quad (3.26)$$

From Eq. (3.21) and Eq. (3.24), we determine the explicit forms for the components of strain tensors in the elastic energy Eq. (3.26). This reads

$$u_{zx} \simeq 0 \quad (3.27)$$

$$u_{yz} \simeq 0 \quad (3.28)$$

$$u_{zz} \simeq -\frac{\nu}{1-\nu}(u_{xx} + u_{yy}). \quad (3.29)$$

⁵The factor $1/2$ is for averaging the stress during doing work, in the same way with the case of a linear spring. Note that the stress σ_{ij} is the value in the final state.

⁶The suffix “es” means “elastic sheet”.

Because the strain tensor u_{ij} is small in Hookean elastic materials, the quadratic term in Eq. (3.10) can be neglected compared to the linear terms: $u_{ij} = \frac{1}{2} \left(\frac{\partial u_i}{\partial r_j} + \frac{\partial u_j}{\partial r_i} \right)$. Using this linearized strain tensor, we obtain

$$\frac{\partial u_x}{\partial z} \simeq -\frac{\partial u_z}{\partial x} \simeq -\frac{\partial \zeta}{\partial x} \quad (3.30)$$

$$\frac{\partial u_y}{\partial z} \simeq -\frac{\partial u_z}{\partial y} \simeq -\frac{\partial \zeta}{\partial y}, \quad (3.31)$$

where $\zeta(x, y) \equiv u_z(x, y, z = 0)$ is out-plane deflection along z -direction. By integration and set the boundary conditions as $u_x(x, y, z = 0) = u_y(x, y, z = 0) = 0$, we obtain

$$u_x = -z \frac{\partial \zeta}{\partial x} \quad (3.32)$$

$$u_y = -z \frac{\partial \zeta}{\partial y}. \quad (3.33)$$

Therefore, by the definition of strain tensor, we finally obtain the explicit forms

$$u_{xx} \equiv \frac{1}{2} \left(\frac{\partial u_x}{\partial x} + \frac{\partial u_x}{\partial x} \right) = -z \frac{\partial^2 \zeta}{\partial x^2} \quad (3.34)$$

$$u_{yy} \equiv \frac{1}{2} \left(\frac{\partial u_y}{\partial y} + \frac{\partial u_y}{\partial y} \right) = -z \frac{\partial^2 \zeta}{\partial y^2} \quad (3.35)$$

$$u_{xy} \equiv \frac{1}{2} \left(\frac{\partial u_x}{\partial y} + \frac{\partial u_y}{\partial x} \right) = -z \frac{\partial^2 \zeta}{\partial x \partial y}. \quad (3.36)$$

Substituting Eq. (3.34)–(3.36) into the elastic energy Eq. (3.26), we have⁷

$$\begin{aligned} E_{\text{es}} &= \frac{E}{2(1-\nu^2)} \int_V z^2 \left[\left(\frac{\partial^2 \zeta}{\partial x^2} + \frac{\partial^2 \zeta}{\partial y^2} \right)^2 - 2(1-\nu) \left\{ \frac{\partial^2 \zeta}{\partial x^2} \frac{\partial^2 \zeta}{\partial y^2} - \left(\frac{\partial^2 \zeta}{\partial x \partial y} \right)^2 \right\} \right] dV. \\ &= \frac{Eh^3}{24(1-\nu^2)} \int_A \left[\left(\frac{\partial^2 \zeta}{\partial x^2} + \frac{\partial^2 \zeta}{\partial y^2} \right)^2 - 2(1-\nu) \left\{ \frac{\partial^2 \zeta}{\partial x^2} \frac{\partial^2 \zeta}{\partial y^2} - \left(\frac{\partial^2 \zeta}{\partial x \partial y} \right)^2 \right\} \right] dA. \end{aligned} \quad (3.37)$$

where $\frac{Eh^3}{12(1-\nu^2)} \equiv \kappa$ and $-\frac{Eh^3}{6(1+\nu)} \equiv \kappa_G$ are, again, bending stiffness and Gauss bending stiffness we saw in the energy of a lipid bilayer membrane Eq. (3.4). As we remarked before, lipid bilayer membranes are two-dimensional fluidic, and shear free. This means that the strain tensor component u_{xy} can be regarded as zero. Therefore, the energy Eq. (3.37) can be

$$E_{\text{es}} = \frac{1}{2} \int_A \left[\kappa \left(\frac{\partial^2 \zeta}{\partial x^2} + \frac{\partial^2 \zeta}{\partial y^2} \right)^2 + \kappa_G \frac{\partial^2 \zeta}{\partial x^2} \frac{\partial^2 \zeta}{\partial y^2} \right] dA. \quad (3.38)$$

The second derivatives of the deflection $\zeta(x, y)$ with respect to x and y are the orthogonal curvatures C_1 and C_2 of the deformed sheet in Cartesian coordinate when the strain u_{ij} is small. Therefore, Eq. (3.38), which are derived from “theory of elasticity” under assumption of small strain, is identical to the bending energy of a bilayer membrane Eq. (3.4), which are derived from the assumption of the two principal curvatures, except for the spontaneous

⁷Note that $\int_V dV = \int_A dA \int_{-\frac{h}{2}}^{\frac{h}{2}} dz$.

curvature term. Whereas the mean curvature H is defined by the first term in the right hand side in Eq. (3.37) or (3.38) as $H = \frac{1}{2} \left(\frac{\partial^2 \zeta}{\partial x^2} + \frac{\partial^2 \zeta}{\partial y^2} \right)$, it should be noted that the Gauss curvature K in an elastic body contains the contribution from shear strain u_{xy} , *i.e.*, $K = \frac{\partial^2 \zeta}{\partial x^2} \frac{\partial^2 \zeta}{\partial y^2} - \left(\frac{\partial^2 \zeta}{\partial x \partial y} \right)^2$ in general.

3.2 Surface tension

In addition to the elastic energy, another important factor we have to consider about the deformation of two-dimensional sheet is surface tension or interfacial tension. When we refer the changes in surface tension in a certain experimental system, there are three candidates in general: (1) changes in surface energy due to the changes in the number of agents consisting of the surface, (2) changes in surface energy due to the changes in the cross-sectional area of each agent while the number of agents is kept constant, and (3) the effective (entropic) surface tension originated from the area constraint [40, 42, 51]. There are various experimental methods to measure the surface tension, we have to be careful about the physical meaning of the surface tension measured in the observed phenomena.

In the case of the lipid bilayer membranes, the surface tension concerning the number of agents (1) can be regarded as constant because the lipid interchanges between the membrane and bulk can be neglected during the deformation. Also, the surface tension concerning each molecular area (2) can be constant because of the incompressible property of two-dimensional fluid, as we discussed before. Therefore, the surface tension of lipid bilayer membranes is effective surface tension (3), and introduced as Lagrange undetermined multiplier for the constraints on the surface area. This effective surface tension can be observed in the shape fluctuation spectrum. It is difficult to give the effective surface tension a direct interpretation as a general physical property, but the effective surface tension strongly influence the shape determination especially in low wavenumber regime.

In the case of lipid monolayer membranes at oil/water interfaces, in contrast to the lipid bilayer membranes, significantly higher surface tension of the order of 1 mN/m strongly suppresses the interfacial deformation. In this case, the meaning of the surface tension is the combination of number of agents (1) and geometrical constraint (3). If we assume there is no bending elastic energy at liquid/liquid, *e.g.*, oil/water, interface, the bending elastic energy for the lipid monolayer membrane can be estimated by a half of that of the lipid bilayer membrane, and the bending stiffness κ of a lipid monolayer membrane is, again, of the order of 10^{-20} – 10^{-19} J. Thus, the surface tension, rather than the bending energy, dominates the observable deformation in the length scale over 1–10 nm, and the W/O droplet systems are spherical in almost all the experimental conditions. This is the remarkable property of the lipid monolayer membranes compared to the bilayer membranes.

3.2.1 Laplace pressure

Let us consider the curved interface of the different two phases, *e.g.*, an oil/water interface (Fig. 3.3). The free energy of this system is

$$F_{\text{int}} = \sigma \int_A dA - p \int_V dV, \quad (3.39)$$

where σ and p are surface tension, or interfacial tension, and pressure, respectively. For simplicity, we here ignore pressure in the bulk. If the spherical interface move through a

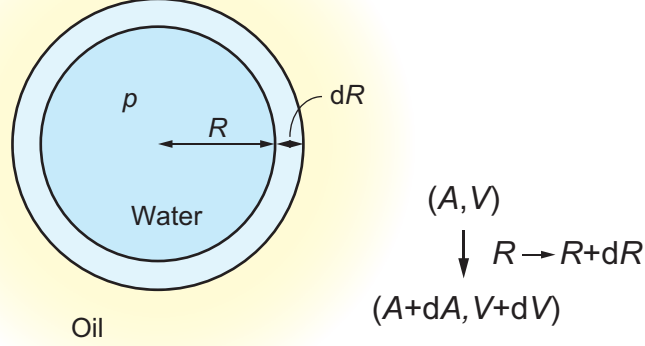


Figure 3.3: Schematic of a system of curved interface.

distance of dR toward the normal direction to the interface, the variation is

$$\begin{aligned} dF_{\text{int}} &= \sigma \int_A^{A+dA} dA' - p \int_V^{V+dV} dV' \\ &= 4\pi R(2\sigma - Rp)dR. \end{aligned} \quad (3.40)$$

Under equilibrium, $\frac{dF}{dR} = 0$ leads

$$p = \frac{2\sigma}{R}, \quad (3.41)$$

which is the additional pressure, called Laplace pressure, inside the spherical droplet necessary to keep the curved interface. In general, it is known that the pressure difference $p_{\text{out}} - p_{\text{in}} = 2\sigma H$ arises at the curved interface with the mean curvature H .

3.3 Fluctuation and deformation of a lipid membrane

Since lipid bilayer membranes are soft interfaces with bending elasticity of the order of thermal energy ($\kappa \sim 10^{-19} \text{ J} \sim 10k_{\text{B}}T$), they easily exhibit Brownian motion driven by the thermal energy in an aqueous solution. In general, when a planar lipid bilayer undergoes a small deformation like thermal fluctuation, it costs the following energy increase regarding the bending energy and (effective) surface tension:

$$\begin{aligned} F &= \frac{\kappa}{2} \int_A dA (2H)^2 + \sigma \left(\int_A dA - \int_A dx dy \right) \\ &= \frac{\kappa}{2} \int_A dx dy \sqrt{g} (2H)^2 + \sigma \int_A dx dy (\sqrt{g} - 1) \end{aligned} \quad (3.42)$$

$$g \equiv \det(g_{ij}), \quad (3.43)$$

where g is the determinant of metric tensor $g_{ij} \equiv \partial_{s_1} \mathbf{R}(s_1, s_2) \cdot \partial_{s_2} \mathbf{R}(s_1, s_2)$ for a two-dimensional plane. $\mathbf{R}(s_1, s_2)$ is a two-dimensional curved surface represented by an arbitrary (curved) coordinate (s_1, s_2) embedded in a three-dimensional space. Assuming the

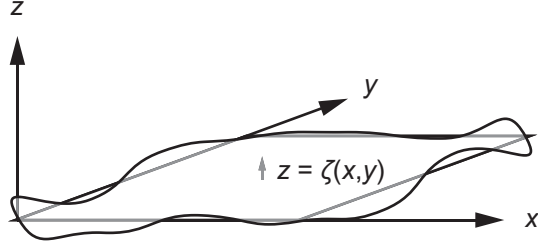


Figure 3.4: Schematic of a deviation of a planar sheet. The deviation along z -direction is represented by $\zeta(x, y)$ in Monge representation.

two-dimensional membrane in (x, y) -plane produce vertical (along z -direction) displacement $\zeta(x, y)$ (see Fig. 3.4⁸), g is described as

$$(s_1, s_2) = (x, y) \quad (3.44)$$

$$\mathbf{R}(s_1, s_2) = (x, y, \zeta(x, y)) \quad (3.45)$$

$$g = 1 + \left(\frac{\partial\zeta}{\partial x}\right)^2 + \left(\frac{\partial\zeta}{\partial y}\right)^2 = 1 + (\nabla\zeta)^2, \quad (3.46)$$

where ∇ is the two-dimensional differential operator. Thus, assuming the displacement ζ is small, *i.e.*, $\frac{\partial\zeta}{\partial x} \ll 1$ and $\frac{\partial\zeta}{\partial y} \ll 1$, g fulfills

$$\sqrt{g} \simeq 1 \quad (3.47)$$

$$\sqrt{g} - 1 \simeq \frac{1}{2} \left\{ \left(\frac{\partial\zeta}{\partial x}\right)^2 + \left(\frac{\partial\zeta}{\partial y}\right)^2 \right\}. \quad (3.48)$$

On the other hand, in Monge representation, the mean curvature is written as

$$2H = -\nabla^2\zeta (1 + \mathcal{O}((\nabla\zeta)^2)) \simeq -\nabla^2\zeta. \quad (3.49)$$

Substituting Eqs. (3.47)–(3.49) into Eq. (3.42), we obtain

$$F = \int_A dx dy \left[\frac{\kappa}{2} (\nabla^2\zeta)^2 + \frac{\sigma}{2} (\nabla\zeta)^2 \right]. \quad (3.50)$$

Further substituting Fourier transformation

$$\zeta(\mathbf{r}) \equiv \int \frac{d^2\mathbf{q}}{(2\pi)^2} \zeta(\mathbf{q}) e^{i\mathbf{q}\cdot\mathbf{r}}, \quad (3.51)$$

where $\mathbf{r} = (x, y)$ and $\mathbf{q} = (q_x, q_y)$, into Eq. (3.50), we can calculate the deformation energy represented in wavenumber space

$$F = \int \frac{d^2\mathbf{q}}{(2\pi)^2} f(\mathbf{q}) \quad (3.52)$$

$$f(\mathbf{q}) = |\zeta(\mathbf{q})|^2 \left(\frac{\kappa}{2} q^4 + \frac{\sigma}{2} q^2 \right). \quad (3.53)$$

⁸This representation is called Monge representation.

Flicker spectroscopy

If we assume thermal equilibrium of a system with the above-derived energy spectrum Eq. (3.52), we can apply the principle of equipartition of energy:

$$\langle f \rangle = \frac{Ak_{\text{B}}T}{2}, \quad (3.54)$$

where $A \equiv L \times L$ and L is the characteristic length scale of the system, *e.g.*, diameter of a cell or vesicle, k_{B} is Boltzmann constant, and T is absolute temperature. Applying the equipartition theorem Eq. (3.54) to the energy spectrum Eq. (3.52), the mean squared amplitude of the deformed shape in wavenumber space, *i.e.*, the spatial power spectrum of the deformed shape, becomes

$$\langle |\zeta(\mathbf{q})|^2 \rangle = A \frac{k_{\text{B}}T}{\kappa q^4 + \sigma q^2}. \quad (3.55)$$

It is possible to measure the mechanical parameters of the system κ and σ by the fitting the experimentally-obtained power spectrum of interfacial fluctuation using Eq. (3.55). From low wavenumber regime and high wavenumber regime of the power spectrum, we can obtain surface tension σ and bending stiffness κ . This kind of experimental method is called flicker spectroscopy [52]. In the case of a lipid bilayer membrane, the amplitude of the interfacial thermal fluctuation is of the order of 10 nm at room temperature ($\sim 25^\circ\text{C}$). Because this length scale of the amplitude is below the optical resolution, some experimental and analytical techniques are required in the image acquisition and the image analyses such as the interface detection with extra-spatial resolution by fitting the blurred information of the recorded images by Gaussian function. With these technical efforts, flicker spectroscopy have been frequently used for characterization of lipid bilayer membranes. It should be noted that the above expression is for the shape fluctuation of a planar membrane, but it can be applied to the thermal fluctuation of a GUV, whose diameter of the order of $10 \mu\text{m}$ is much larger than the thermally-activated small amplitude of the order of 10 nm.

Regarding the shape fluctuation of a spherical GUVs, the exact formula of wavenumber-mode expansion for quasi-spherical vesicles are given with using spherical surface harmonics. However, the mathematical expression is quite complicated including a series of Legendre polynomials and a factorial factor [53]. On the other hand, Pécrciaux *et al.* have refined the planar sheet representation Eq. (3.55) to exactly describe the fluctuation of equatorial lines in the cross-sectional images that is accessible in microscopic observation. They also quantitatively compared their refined equation to the model with spherical harmonics, and confirmed that the effective-tension effect from spherical harmonics is significant in the low wavenumber regime ($m = 0-4$; mode number) because of the area constraint in a closed geometry but the difference between them is within the experimental error in the high wavenumber regime ($m \geq 5$). After their quantitative work, their representation have been much more frequently adopted for flicker spectroscopy of a GUV due to the simplicity of the expression. In the following we show the detail of their representation.

The experimental observation of the shape fluctuation of a GUV is normally performed by optical or phase contrast microscopy. In this technique, the contour information we can obtain is the shape change in the cross-sectional image of the GUV. Therefore, we have to describe the mathematical expression that corresponds to the fluctuation spectrum of the equatorial line in the obtained images in (x, z) -plane (Fig. 3.5). To do so, we calculate

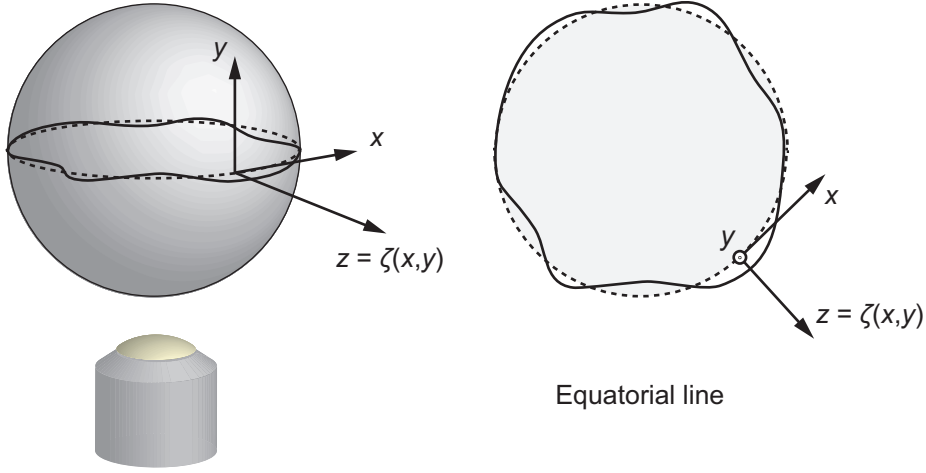


Figure 3.5: Schematic of experimentally accessible equatorial line.

inverse Fourier transformation over wavenumber q_y :

$$\langle |\zeta(q_x, y)|^2 \rangle = L \int \frac{dq_y}{2\pi} \langle |\zeta(\mathbf{q})|^2 \rangle e^{-iq_y y}. \quad (3.56)$$

The amplitude of the equatorial line in the cross-sectional images is then obtained by setting $y = 0$ in the inverse Fourier transformation:

$$\begin{aligned} \langle |\zeta(q_x, y = 0)|^2 \rangle &= L \int \frac{dq_y}{2\pi} \langle |\zeta(\mathbf{q})|^2 \rangle \\ &= \frac{k_B T}{2\pi L} \int dq_y \frac{1}{\kappa(q_x^2 + q_y^2)^2 + \sigma(q_x^2 + q_y^2)}. \end{aligned} \quad (3.57)$$

After the calculation of the integral by residue theorem, the final expression

$$\begin{aligned} \langle |\zeta(q_x, y = 0)|^2 \rangle &= \frac{k_B T \pi}{2\pi L \sigma} \left(\frac{1}{q_x} - \frac{1}{\sqrt{q_x^2 + \frac{\sigma}{\kappa}}} \right) \\ &= \frac{k_B T}{2L\sigma} \left(\frac{1}{q_x} - \frac{1}{\sqrt{q_x^2 + \frac{\sigma}{\kappa}}} \right) \end{aligned} \quad (3.58)$$

is obtained.

Note that the obtained wavenumber representation Eq. (3.58) is for the deformation of lipid bilayer membranes where the interfacial shape is determined by bending energy and surface tension. Contrary to the bilayer membranes, the deformation of lipid monolayer membranes is in most cases, as we discussed before, determined only by surface tension.

3.4 Fluctuation and deformation of cell shape

Up to here, we introduced the fluctuation and deformation of pure lipid bilayer membranes. In the case of biological interfaces, these equations consisting of bending elastic energy and effective surface tension are modified due to the existence of a multitude of membrane proteins and the effect of cytoskeleton underlying the cell membrane. While the membrane

proteins modify the value of bending stiffness κ and surface tension σ , the cytoskeleton connected to the cell membrane adds an optional elastic energy. In general, as we noted in Section 1, it is not easy to discuss the elastic effects from a variety of cytoskeletal filaments in a unified perspective because their effects depend on different connection mechanisms of different cytoskeletal proteins and the different mechanical properties, such as persistence length. In many past studies to describe a physical representation of cytoskeletal effects, one of the subjects in which deep understanding have been obtained is the deformability of red blood cells with spectrin cytoskeletal network. There are some advantages for us to first investigate red blood cells as an example of biological interfaces, for example, their internal structure without any organelles is much simpler than those of normal cells, we can easily obtain homogeneous cell samples from blood, and so on. One of the research subjects in physics is the shape fluctuation of a red blood cell. In these works, cell-shape fluctuation in solution have been treated as thermal fluctuation, and the physical properties such as viscoelasticity of biological interfaces have been quantified from the spectrum analyses (flicker spectroscopy). One big difference from GUVs is that the spectrin cytoskeletal network, interacting with the inner leaflet of cell membrane, generates shear elastic energy. Whereas the pure lipid bilayer membrane is highly fluidic and no effective shear energy is stored, spectrin hexagonal lattice with 80–100 nm internode distance are connected to the membrane proteins embedded in the cell membrane and it elastically responds to the shear deformation.

Flicker spectroscopy for red blood cells

The experimental technique of flicker spectroscopy first started from the analysis of “flickering” of the intensity in a phase contrast image of a red blood cell performed by F. Brochard and J. F. Lennon [52]. “Flickering” phenomenon is originated from the fluctuation of the separation distance between the upper and lower red blood cell membrane, where the interspace is filled with the optically-dense cytoplasm. In this work, they derived Eq. (3.53) for bending elastic energy and surface tension in the case of osmotically-swollen cells. In addition to these terms, they estimated the effect of cytoskeleton by a shear elastic energy density of two-dimensional rubber sheet [52, 54]:

$$f_{\text{shear}} = \frac{\mu}{4}(l^2 + l^{-2} - 2), \quad (3.59)$$

where μ is elastic constant and l is longitudinal extension. Assuming that the deflection $u(x)$ is small, they wrote the longitudinal extension l as

$$l = \sqrt{1 + \left(\frac{d\zeta}{dx}\right)^2} \simeq 1 + \frac{1}{2} \left(\frac{d\zeta}{dx}\right)^2, \quad (3.60)$$

and by substituting Eq. (3.60) into Eq. (3.59), they evaluated f_{shear} as

$$f_{\text{shear}} = \mu(l - 1)^2 \simeq \frac{m\mu}{4} \left(\frac{d\zeta}{dx}\right)^4. \quad (3.61)$$

Based on this approximation, they neglected f_{shear} compared to the bending energy density $f_{\text{bend}} = \frac{\kappa}{2} \left(\frac{d^2\zeta}{dx^2}\right)^2$ because the small deflection $\zeta(x)$ for shear deformation is fourth-order small quantity.

Although Brochard and Lennon ignored the shear elastic energy f_{shear} of a red-blood-cell shape fluctuation under the planar-sheet approximation, Peterson [55] and Strey *et al.* [56] paid attention to the fact that the shear deformation energy of the curved interface is the second order of displacement ζ , and included shear elastic energy in addition to bending elastic energy to describe the curved cell shape fluctuation [55]. However, the obtained shear modulus $\mu \leq 10^{-7} \text{ J/m}^2$ [56, 57] from flicker spectroscopy with the shear elastic energy term of a solid sheet was much smaller, by two orders of magnitude, than the shear modulus $\mu \sim 10^{-5}\text{--}10^{-6} \text{ J/m}^2$ measured by static deformation method using shear flow [58] or micropipette aspiration [59–62].

In response to the discrepancy about shear modulus μ between the thermal fluctuation and static deformation, another energy model aiming for the consistent description between them was proposed by Gov *et al.* [63]:

$$F = \int_A dA \left[\frac{\sigma}{2} (\nabla \zeta)^2 + \frac{\kappa}{2} (\nabla^2 \zeta)^2 + \frac{\gamma}{2} \zeta^2 \right], \quad (3.62)$$

where γ is effective shape constraint by the existence of spectrin cytoskeletal network, represented as the harmonic potential for the shape deviation from the mean circular shape. In this model, Gov *et al.* limited their focus on the shape fluctuation of 0.1–1 μm in the length scale, by considering the fact that the shear modulus in the past fluctuation studies was calculated from the longest length scale over a single cell, *i.e.*, wavenumber mode 1 and 2. It should be noted that this representation of the fluctuation energy under continuum approximation is valid only in the length scale longer than 80–100 nm, which is the internode distance of spectrin hexagonal lattice. Substituting Fourier transformation Eq. (3.51) into Eq. (3.62), the corresponding mean squared amplitude of the red blood cell shape fluctuation reads

$$\langle |\zeta(\mathbf{q})|^2 \rangle = A \frac{k_B T}{\kappa q^4 + \sigma q^2 + \gamma}. \quad (3.63)$$

Furthermore, Yoon *et al.* calculated the inverse Fourier transformation Eq. (3.56) in this equation in the same way with Pécrcéaux *et al.* [64], and obtained the mean square amplitude of the shape fluctuation that exactly corresponds to the equatorial line in the cross-sectional images [65]:

$$\langle |\zeta(q_x, y = 0)|^2 \rangle = \frac{k_B T}{L} \sqrt{\frac{\kappa}{2(\sigma^2 - 4\kappa\gamma)}} \left(\frac{1}{\sqrt{2\kappa q_x^2 + \sigma - \sqrt{\sigma^2 - 4\kappa\gamma}}} - \frac{1}{\sqrt{2\kappa q_x^2 + \sigma + \sqrt{\sigma^2 - 4\kappa\gamma}}} \right). \quad (3.64)$$

athermal fluctuation of red blood cell shape

Flicker spectroscopy is the measurement method to quantify the mechanical properties based on the supposition that the shape change of a red blood cell in a solution is thermally driven and equipartition theorem is applicable. Within this framework, the deformation energies decomposed in wavenumber space are related to the shape information with the corresponding wavelength. On the other hand, there are some reports that state the fluctuation amplitude of a red blood cell depends on the amount of ATP inside the cell [66, 67]. This result indicates that the shape fluctuation is driven not only by thermal agitation but also by some non-equilibrium processes, probably correlated with its biological processes. In fact, red blood cells perform temporal dissociation of spectrin nodes together with the

transportation of ATP from cytosol to the exterior through phosphorylation of a membrane protein called protein 4.1 [14, 54, 68–70]. Although it is still controversial and unclear how such a dynamic process can practically contribute to the fluctuation spectrum.⁹

In contrast to the purely passive shape fluctuation of artificial lipid membranes, this ATP-dependence is probably unique to the biological interfaces and highly interesting. To elucidate the detailed physical mechanism of this biological phenomena would be done with sophisticated experimental techniques combining molecular biology, cell biology, and physics in the future. In this thesis, we regard the red-blood-cell shape fluctuation as thermally driven fluctuation according to the large majority of previous reports, and we experimentally study the mechanics of the fluctuation by perturbing the cell structure with additive molecules from the outside.

⁹Gov *et al.* speculated that the dynamic dissociation of the cytoskeleton and the cell membrane plays a role of active “kick” to the membrane and locally enhances the fluctuation amplitude at the dissociation point [71], but no experimental evidence has not been studied. In addition, Gov *et al.* and Prost *et al.* stated that such a ATP-dependent fluctuation can be renormalized into “effective temperature” without qualitative changes in the spectrum [71, 72].

Chapter 4

Outline of the thesis

In keeping with the general introduction up to here, in this thesis, we describe our recent developments aimed at the elucidation of the physical mechanism of the shape fluctuation, deformation, and the emergent interfacial properties of biological interfaces. In particular we focus on the interaction between the membrane and cytoskeleton. To understand a variety of cellular deformabilities correlated with various kinds of membrane proteins and cytoskeleton from the viewpoint of not biology but “material science”, we study both living cells and non-living reconstituted systems.

In Chapter 5 in Part II, we report the study on shape fluctuation of a living system, *i.e.*, the shape fluctuation and deformation of a human red blood cell, which is the simplest cell-membrane-cytoskeleton system. Using flicker spectroscopy, we here measure the quantitative changes in the fluctuation and deformation behaviors before and after the addition of amphiphilic additional molecules, endotoxins, which are molecular factor of a well-known disease, sepsis. This study allows us to quantify how and how much the additives alter the mechanical properties of the cell membrane and cytoskeleton. Also, we report the comparison between adult and neonatal red blood cells and the effect of anti-septic peptide, which is a candidate of anti-septic drugs. From our analyses of the experimental results, we confirm that the cytoskeletal confinement term in Eq. (3.64), which is related to shear elastic energy but was neglected in the previous study [65], dominantly responds to the additives and should be examined.

The above fluctuation analysis is performed under assumption of thermal equilibrium, and in fact the experimental result is consistent with the assumption in the case of red blood cells. In Part III, we in turn focus on the mechanism of more active and spontaneous deformation like amoeboid motion. The most interesting difference from the relatively static behaviors of red blood cells under thermal equilibrium is the spontaneous force generation inside these “active” cells. In the spontaneous force generation, cytoskeletal protein, actin, and molecular motor protein, myosin, specifically play important roles; They generate contractile force by consuming ATP. The contraction phenomena in living cells are involved in the sophisticated functions such as cell motility and cell division through the tactical controls of spatiotemporal expression and structures of actin and myosin supported by numerous binding proteins. To understand how the contractility of the actin and myosin contributes to the actual deformation from the aspect of the material properties and the emergence of the phenomena, there are two strategies: to study *in vivo* living cells or *in vitro* reconstituted system. Because our purpose is to elucidate the non-equilibrium interfacial phenomena based on the physics of material properties, we here conduct the studies with

the reconstituted system composed of extracted actin and myosin enclosed within a lipid monolayer membrane. Using this system, we observe the two different types of interfacial deformation coupled to the different higher-order structure formations of actomyosin. From the spectrum analyses, we discuss the fast and repetitive interfacial motion in Chapter 6 and slow irreversible interfacial deformation in Chapter 7. The unique achievements in the series of works are not only to fabricate the reconstituted model interface that deforms by actomyosin contractility for the first time, but also to propose physical laws of interfacial active motion (Chapter 6) and interfacial deformation (Chapter 7) based on the analyses of the emergent experimental phenomena therein.

In Part IV, we introduce our study on droplet transfer method, which is used to transform the lipid monolayer membranes to the lipid bilayer membranes, which is more like the cell membrane structure. In general, it is quite difficult to form cell-sized lipid bilayer vesicles encapsulating desired solutes at a physiologically high concentration. This method is one of good candidates to overcome the experimental difficulty. In Chapter 8, we reveal the physical mechanism of the kinetic trapping process and droplet-size dependence, which have been problems underlying the method, through the combination of an experiment and a phenomenological theory. In addition, we introduce in Chapter 9 a developed method using capillary-based microfluidic device, in which the size-dependent kinetic process revealed in Chapter 8 is applied as filtration process to select only lipid bilayer vesicles with several tens of μm in diameter.

Finally, in chapter 10 in Part V, we summarize the thesis and give conclusive remarks with future prospects for the fluctuation and deformation of biological soft interfaces.

Part II

Passive shape fluctuation and deformation of a cell

Chapter 5

Shape fluctuation of a red blood cell

In this chapter, we report our experimental investigation on the fluctuation and the deformation of red blood cells (RBCs) by focusing on the relative changes in the cell mechanics when the cell is exposed to some additives. As a model case, we here investigate the influence of endotoxin-induced sepsis symptoms on human RBCs. The experimental strategy is to quantify the impact of endotoxins on the cell mechanics by the analysis of Fourier-transformed mean square amplitude of shape fluctuation, called flicker spectroscopy. With the aid of a microfluidic diffusion chamber, we noninvasively and systematically determine principal mechanical parameters of human RBCs in the absence and presence of endotoxins for individual RBCs for the first time. Because of the elongation of saccharide chain length of endotoxins, we find an increase in the morphological transition, *i.e.*, deformation of the mean shape, from discocytes to echinocytes, and monotonic changes in the mechanical parameters. Since septic shocks often cause lethal risks of neonates, we measure the mechanical parameters of neonatal RBCs, and compare them to those of adult RBCs. The quantitative comparison reveals that neonatal RBCs are more susceptible to the effect of endotoxins than adult RBCs. Furthermore, coincubation with the anti-septic peptide P19-2.5 (Aspidasept) with endotoxin results in a slight suppression of the impact of the endotoxin. These results clearly show the significant effect of not only bending stiffness of bilayer lipid membranes but also cytoskeletal confinement potential on the fluctuation and the deformation of RBCs.

5.1 Introduction

Lipopolysaccharides (LPSs) are the major constituent of outer membranes of Gram-negative bacteria that guarantee the structural integrity of bacteria. LPSs are also known as endotoxins because of their capability to cause systematic inflammatory response syndromes in our body, such as sepsis [73]. The most fundamental building block of endotoxin is composed of six hydrocarbon chains and a hydrophilic group, called lipid A, which is further modified with additional inner and outer core saccharides. The complex LPSs with only inner core, which is the simplest form for the growth of Gram-negative bacteria, and both inner and outer cores are called LPS Re and LPS Ra, respectively [74]. To date, many studies have indicated that the septic shocks caused by the exposure to endotoxin have a significant consequence on the mechanics of red blood cells (RBCs). For example, Pöschl and Linderkamp measured the deformability (physically equivalent to the aspect ratio between the major

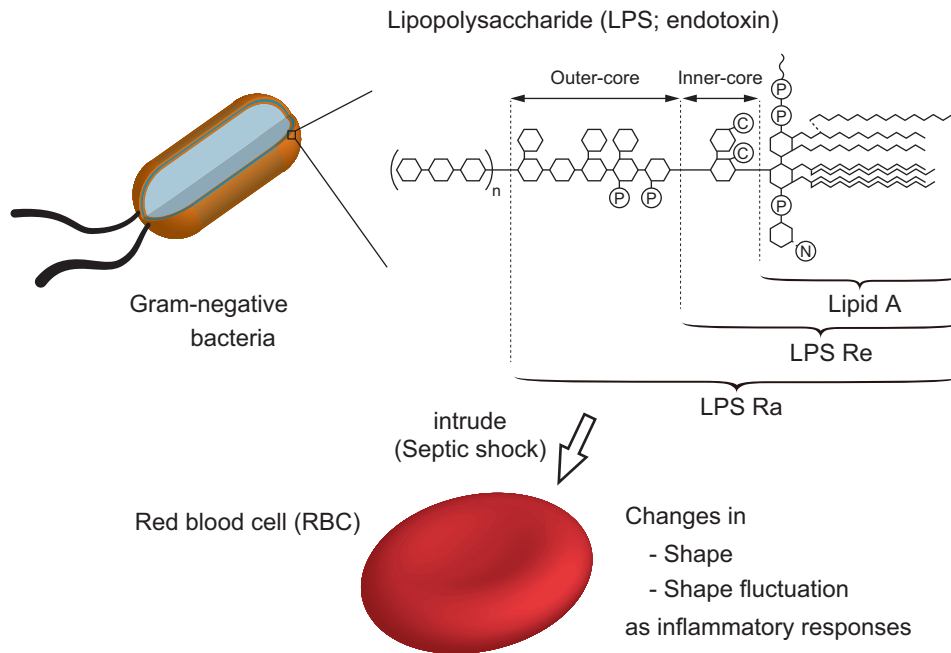


Figure 5.1: Schematics of lipopolysaccharides (LPSs; wild type, LPS Ra, LPS Re, and lipid A), which are consisting of the outer membranes of Gram-negative bacteria (not to scale). LPSs causes septic shock, systematic inflammatory response syndromes, by altering the mechanics of red blood cells (RBCs).

axis and minor axis) of elliptically deformed RBCs from adults [75, 76] and neonates [77], *i.e.*, newborn infants, under shear stresses, demonstrating that endotoxin causes more significant changes in the deformability of neonatal RBCs than adult RBCs. The exposure to group B *Streptococcus* leads to a significant decrease in the deformability under shear, *i.e.*, RBCs became stiffer against the elongation and thus lose their capability for microcirculatory blood flow. This tendency was much more pronounced for neonatal RBCs than adult RBCs, as sepsis tends to be more critical for neonates whose prematured immune systems cannot fight against external intruders [78]. From the physical viewpoint, the change in the aspect ratio of RBC under mechanical stresses could be attributed to the shear deformation of a viscoelastic body, which have been investigated using optical tweezers [79, 80] and optical stretchers [81–83] more recently. However, despite of major developments in impairing the progression of diseases and revealing cell mechanics, these approaches did not shed light on the impact of endotoxins on key mechanical parameters, such as the bending stiffness and surface tension [57, 63]. Therefore, to clarify this general elasticity under the endotoxic conditions can lead to deeper understanding and quantification of the diseased state and mechanical response of the RBCs.

Another experimental approach to determine the mechanical properties of membranes from the fluctuation of membrane shapes, called flicker spectroscopy, was developed after the pioneering study by Brochard and Lennon [52]. Here, the “flickering” of the local cell thickness observed by the phase contrast imaging was attributed to the thermal or non-thermal agitation against the bending energy of cell membranes described by Helfrich [40]. Brochard and Lennon assumed in their model that shear elastic energy of the cytoskeletal network could be neglected compared to the bending energy of the cell membrane due to the

assumption of a planar membrane. To obtain information on the cell shape more directly, the following studies included shear elasticity to the theory, which is more appropriate to analyze the curved cell rims [56,84]. More recently, the confinement of membrane deviation due to the underlying cytoskeletal structure, *i.e.*, spectrin network, was incorporated to the theory [63,71] to explain the gap between obtained shear moduli in the above models with experimental values obtained by static deformation experiments such as micropipet aspiration [60,61] and electro-deformation [62,85]. As it was pointed out by Yoon *et al.*, this energetic term of the cytoskeletal confinement and the shear energy term of a single, polymerized cytoskeletal network lead to a similar formulation for the mean square amplitude of the contour fluctuation [55,65]. Within the framework, the spring constant γ of the harmonic potential that confines membranes adjacent to cytoskeletons can be replaced by the ratio between the shear elasticity μ and the membrane area A , μ/A . Recently, this model was refined to optimize to the analysis of the cross-sectional images of equatorial cell rims, which are usually obtained by phase contrast microscopy [64]. This model can quantify the spring constant of the cytoskeletal confinement, bending stiffness, and surface tension by the fitting of experimentally obtained mean square amplitude of shape fluctuation of RBCs. However, despite of the development in the theoretical analysis, the use of flicker spectroscopy to determine the impact of external stimuli, leading to septic shocks, on the membrane mechanics has been limited because of the difficulties in tracking changes in the mechanics of individual cells over time: A simple ensemble is not sufficient to capture the essential behavior of individual cells, which often express considerably inhomogeneous cell mechanics because of the aging of RBCs during their life-span of 120 days.

In the present paper, we apply the flicker spectroscopy and microfluidic systems to quantify the mechanics of individual cells under healthy and septic conditions. Here, we adopted a “diffusion chamber” [86] to analyze exactly the same individual cells. Since the use of diffusion chambers enables one to exchange the surrounding environment of cells within a few minutes, we tried to quantify not only impacts of endotoxins but also the curative effects of anti-septic peptide P19 (P19-2.5, Aspidasent) against them [87].

5.2 Materials and methods

5.2.1 Sample preparation

Adult and neonatal blood was drawn from healthy donors with the approval of the Ethical Committee of University of Heidelberg and the informed consent of donors and parents. PBS buffers (pH 7.4) with 130 mM NaCl, 10 mM glucose and 1 mg/mL Bovine serum albumin (BSA, Sigma-Aldrich, St. Louis, MO) was used as the buffer solution throughout the study, where 10 mM glucose is needed to keep the ATP level and the cytoskeletal remodeling during the measurements. [66,67] RBCs were extracted from the blood sample by 1/40 dilution, centrifugation and replacement of supernatant by the buffer: First, we diluted the sample blood by the buffer (blood:buffer = 4 μ L:196 μ L). Next, the obtained 200 μ L solution was centrifuged (1000 rpm, 6 min) and the supernatant, which is 90% of the entire solution, was replaced by the PBS buffer. Then, we repeated the above process two times more. All human RBCs extracted in this process had the shape of a biconcave discoid (discocyte), as those under physiological condition are. Endotoxins, LPS Re and LPS Ra, were purified from bacterial strains R60 and R595 of *Salmonella enterica* serovar Minnesota [88,89], while lipid A was obtained by hydrolysis of LPS Re [90]. The powders of lipid A, LPS Re and

LPS Ra were dissolved in the PBS buffer at concentrations of $100 \mu\text{g}/\text{mL}$, respectively. Anti-septic peptide P19-2.5 (P19, MW = 2711) [87, 91, 92] was premixed with a portion of $100 \mu\text{g}/\text{mL}$ LPS Ra solution at a concentration of $1 \text{ mg}/\text{mL}$. Using these endotoxin and endotoxin with anti-septic peptide solutions, we performed the following perfusion in the microfluidic diffusion chamber.

5.2.2 Microfluidic diffusion chamber

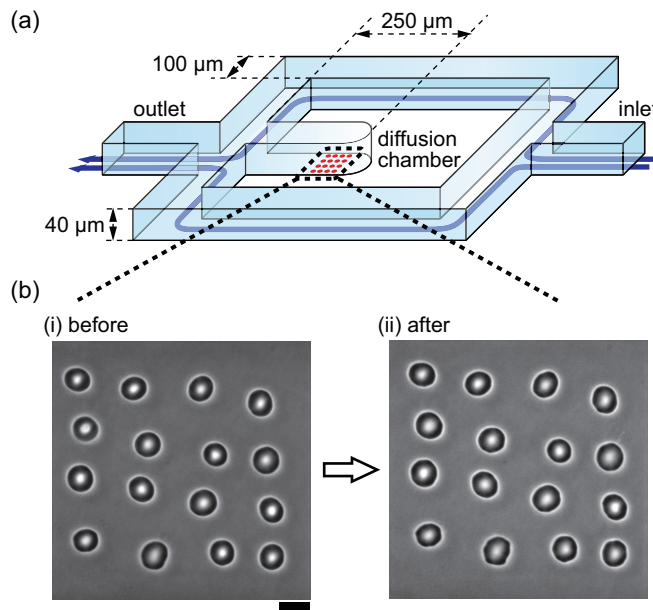


Figure 5.2: (a) Schematic of a microfluidic diffusion chamber. Blue arrows show the flow direction inside the channel. Substances dissolved in water can diffuse into the “diffusion chamber” in a controlled manner (see Fig. 5.3 for detail). (b) Full view of aligned red blood cells in the diffusion chamber before and after perfusion of LPS Ra $100 \mu\text{g}/\text{mL}$ solution inside the channel. Scale bar: $10 \mu\text{m}$.

Figure 5.2(a) shows a schematic illustration of a microfluidic diffusion chamber. The flow channels were molded in a poly(dimethylsiloxane) (PDMS) resin, and enclosed by a glass coverslip. The mold for replicating the PDMS chips was manufactured via photolithography in SU-8 (type 2075, purchased from micro resist technology, Germany) using a maskless projection lithography system as described previously [93]. Briefly, SU-8 was spin-coated (30 s at 500 rpm, 55 s rest, 20 s at 3000 rpm) on cyclic olefin copolymer (COC, type TOPAS 6013S-04), prebaked (1 h at 75°C , 4 h at 95°C), exposed and postbaked (2 min at 65°C , 10 min at 95°C) and developed in ethyl-L-lactate (purchased from Sigma Aldrich, Germany) in an ultrasonic bath (5 min). After unset PDMS was poured on the mold, the air contained in the PDMS was degassed under vacuum for 1 h. Then, the PDMS was baked at 80°C overnight. The microstructure was cut out of the mold, and the holes for inlet and outlet of solution were made. Finally, the glass coverslip and the PDMS chip were bonded by the surface treatment with a corona discharger (BD-20AC Laboratory Corona Treater, Electro-

Technic Products) for 10 s each. The inlet and outlet holes were connected to silicon tubes via polytetrafluoroethylene (PTFE) tubes, and the inlet silicon tube was connected to a syringe. Then 16 RBCs were placed and aligned in the diffusion chamber (see Figure 5.2(b)) using an optical tweezers in approximately 20 min. Figure 5.2(b) shows RBCs before (i) and after (ii) perfusion of another kind of solution. This microfluidic device allows us to exchange the surrounding solute condition inside the diffusion chamber within a few minutes only by diffusion, *i.e.*, without flow, at a desired timing and at a desired solute concentration.

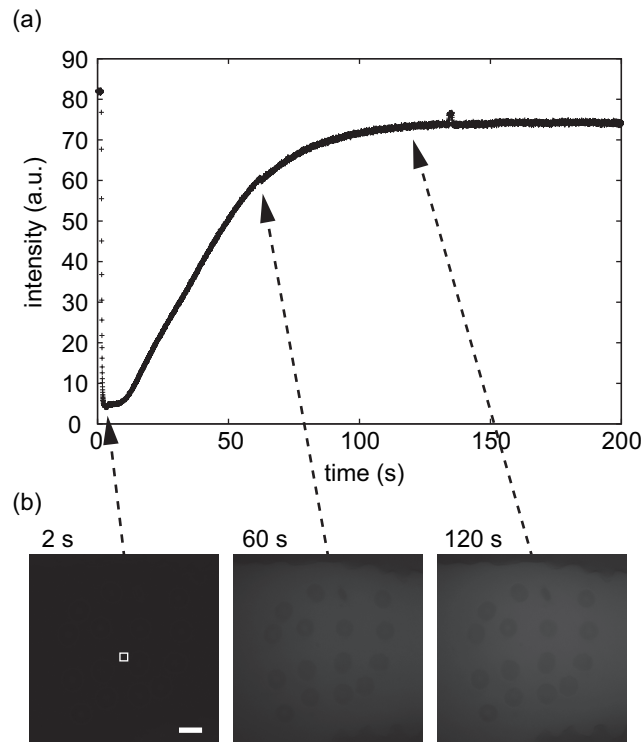


Figure 5.3: Demonstration of the exchange of the solution inside a microfluidic diffusion chamber (see Fig. 5.2(a)). (a) Time course of intensity change during the perfusion of the aqueous solution of fluorescent molecules (calcein, MW = 622.55). The increase in the concentration inside the chamber was saturated within a few minutes. (b) Full view of aligned red blood cells in the diffusion chamber. The fluorescence intensity was averaged inside the region enclosed by the white solid line. Scale bar: 10 μm .

Before use of the microfluidic “diffusion chamber” for the experiments of endotoxins, we confirmed the capability of the chamber as shown in Figure 5.3. Here we demonstrated the diffusion of a fluorescent molecule calcein (M.W. = 622.55) into the chamber. After the perfusion of the aqueous solution of calcein 100 μM , we measured the mean fluorescence intensity inside the chamber as a function of time (Figure 5.3(a)). The time course of the intensity change shows that the diffusion of the molecules into the chamber was achieved within a few minutes. It should be noted that this characteristic time is much shorter than approx. 15 min, which is required to reach a thermal equilibrium state for the present experimental system. Here, the thermal equilibrium of the experimental system is defined

as the state with no thermal focus-drift of microscopy as well as temperature-drift of the chamber. Figure 5.3(b) shows the corresponding fluorescence images inside the microfluidic diffusion chamber during the perfusion of calcein molecules, where the fluorescence intensity gradually increased without any significant flow.

5.2.3 Microscopic observation

The microfluidic device with aligned RBCs inside the chamber was set inside a thermostat (37°C) on the stage of an optical microscope (TE-2000U, Nikon and Axiovert 200, Zeiss) with a ring aperture. After thermal equilibrium with constant temperature, we recorded 600 frames of temporal cell shapes with a $\times 100$, N.A. = 1.3, oil-immersion objective lens and EM-CCD camera (C9743-13, Hamamatsu), resulting pixel size was $0.16\ \mu\text{m}$, or $\times 100$, N.A. = 1.4 oil-immersion objective lens and CCD camera (C4742-95-12ER, Hamamatsu), pixel size $0.1\ \mu\text{m}$, for each cell. To obtain temporal ensemble average of shapes for each cell, exposure time and time interval of adjacent two frames were taken as 30.5 ms. Then, the inlet silicon tube filled with the buffer was replaced by the tube filled with endotoxin solution, and repeated the above record procedure. In the case of treatments of P19, the inlet silicon tube for LPS Ra solution was further replaced by the tube filled with LPS Ra and P19 solution, and the procedure was repeated. Note that the diffusion of solutes into the chamber is much faster than the thermal equilibration of the whole system with newly perfused solution (see Fig. 5.3).

5.2.4 flicker spectroscopy

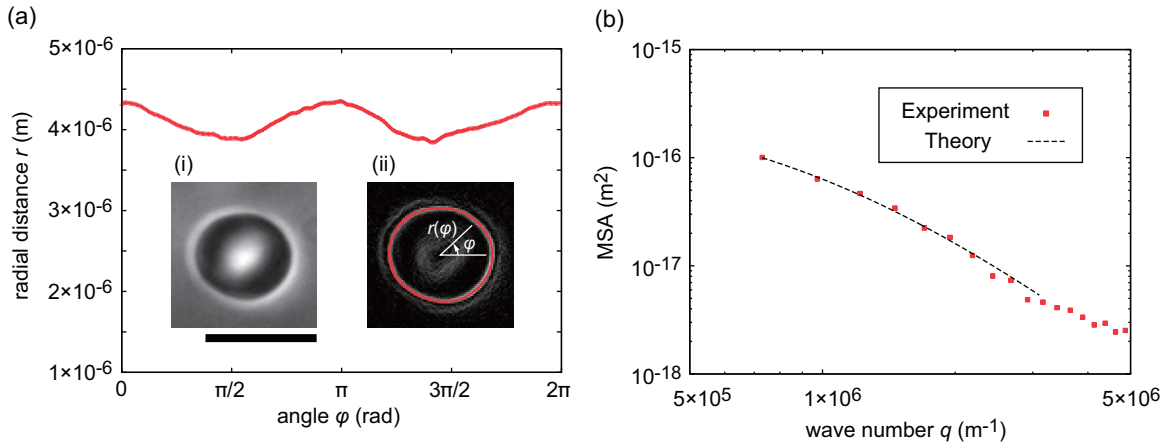


Figure 5.4: (a) Detected radial distance from the center of mass plotted versus angle φ ($0 \leq \varphi < 2\pi$). Typical examples of (i) the phase contrast image of a fluctuating red blood cell and (ii) the identified cell rim from the intensity gradient are presented as the insets. Scale bar: $10\ \mu\text{m}$. (b) Mean square amplitude of the shape fluctuation of the cell rim (red markers) and the best-fit result with theoretical model (dashed line). The fitting was performed from the third wavenumber mode to the maximum spatial resolution (see main text for details).

The inset of Figure 5.4(a) shows a typical phase contrast image. Cell rim can be detected as the intensity peak of an intensity-gradient magnitude image obtained in ImageJ [94]. Whole rim detection of the captured cell images was performed by a custom routine in Igor Pro (WaveMetrics, Oregon). Briefly, in polar coordinate (r, φ) , 360 discrete radial distance $r(\varphi)$ ($0 \leq \varphi < 2\pi$) for 360 deg from the center of mass to the rim were detected for each frame (Figure 5.4(a)). The fluctuation profiles, which are defined as the deviation from the time-averaged cell shapes, were Fourier-transformed into the mean square amplitudes as a function of wavenumber q :

$$\langle \zeta(q)^2 \rangle = \left\langle \left| \frac{2}{N} \sum_{n=0}^{N-1} \{r(n\Delta x) - \langle r(n\Delta x) \rangle\} e^{\frac{2\pi i(r)qn}{N}} \right|^2 \right\rangle, \quad (5.1)$$

where $\langle \rangle$ denotes time average over the whole frames, $N = 360$ is the sampling number, and $\Delta x = 2\pi \langle r \rangle / N$. On the other hand, theoretically predicted mean square amplitude is described as

$$\langle \zeta(q_x, y = 0)^2 \rangle = \frac{k_B T}{L} \sqrt{\frac{\kappa}{2(\sigma^2 - 4\kappa\gamma)}} \left(\frac{1}{\sqrt{2\kappa q_x^2 + \sigma - \sqrt{\sigma^2 - 4\kappa\gamma}}} - \frac{1}{\sqrt{2\kappa q_x^2 + \sigma + \sqrt{\sigma^2 - 4\kappa\gamma}}} \right), \quad (5.2)$$

where q_x is the continuous wavenumber corresponding to the experimental q , and L denotes one-dimensional length of a RBC [65]. Because Eq. (5.2) corresponds to the mean square amplitude of the cross-sectional line between a fluctuating planar membrane and a focal plane, it would be invalid for a closed and curved membrane of a RBC in a small wavenumber region. Thus, we performed the fitting with Eq. (5.2) over the third wavenumber mode ($\langle r \rangle q \geq 3$), where the gap between the mean square amplitudes of planar and spherical membrane becomes within 15%. Figure 5.4(b) exemplifies that Eq. (5.2) is sufficiently good to fit the experimental mean square amplitude in this wavenumber region. As previously demonstrated, the low wavenumber region is dominated by spring constant γ and surface tension σ , while the high wavenumber region is by bending stiffness κ [65, 95]. The overall curve is determined as a combination of these mechanical parameters [95]. As an example, Figure 5.5 demonstrates the two fittings that correspond to before (gray) and after (black) the perfusion of endotoxin solution. From the best-fit result, we quantified the essential elastic coefficients for each RBC: spring constant γ , bending stiffness κ and surface tension σ [95]. Coefficients of determination for the fittings were sufficiently high (above 0.999) with these three mechanical parameters. Note that spring constant of the cytoskeletal confinement γ is proportional to the shear modulus of membrane-cytoskeleton complex for a closed spherical membrane.

5.2.5 Correlation coefficient

In the present study we quantitatively calculated the impacts of endotoxins on the elastic properties of individual RBCs, namely the relative changes in the elastic parameters between before and after the perfusion of endotoxins. In general, to extract a statistical meaning from an ensemble of individual samples, the mean value and the standard deviation (SD) are often used. However, individual RBCs with individual mechanical parameters can respond to endotoxins in individual manners, due to the combination of their scattered initial values

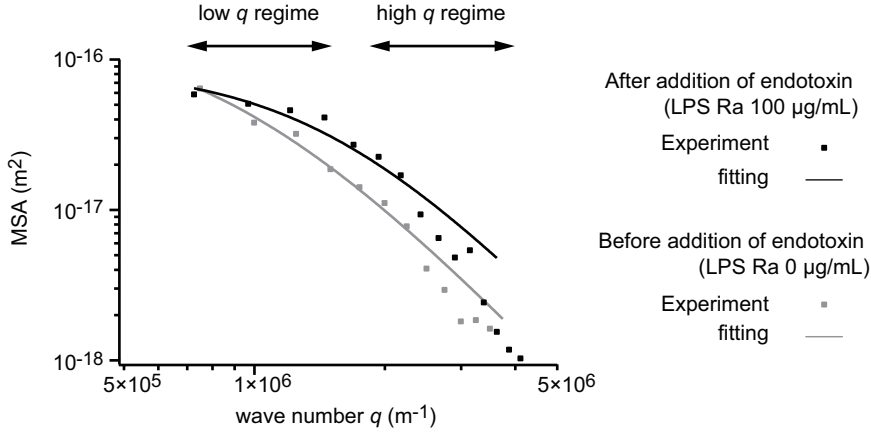


Figure 5.5: Fitting examples of two mean squared amplitudes (MSAs) versus wave number q before (gray) and after (black) the addition of $100 \mu\text{g}/\text{mL}$ LPS Ra. The symbols correspond to the experimental results, and the fitting curves are presented as lines. After the addition of LPS Ra, MSA in the high q regime uniformly increased, while MSA in the low q regime became flatter, indicating decrease in κ and increase in γ at the same time.

and scattered responses. As a result, SD in the ensemble of relative changes cannot describe systematic reliability. Therefore, here we focused on not SD but the correlation coefficient of the ensemble defined as

$$C.C. = \frac{\sum_{i,j=\{cell\}} \Delta x_i \Delta x_j}{N \sum_{i=\{cell\}} \Delta x_i^2} \quad (5.3)$$

where Δx_i denotes a relative change in a mechanical parameter such as bending stiffness of i th RBC ($i = 1, 2, \dots, N$; index of individual cells). This quantity, the normalized auto-covariance of the ensemble, measures the coherency of the individual relative changes in a physical quantity Δx_i by a scholar value ranging $0 \leq C.C. \leq 1$. $C.C. = 1$ means complete matching of all the relative changes, *i.e.*, $\Delta x_1 = \Delta x_2 = \dots = \Delta x_N$, while $C.C. = 0$ means no systematic tendency in the individual relative changes, *i.e.*, $\Delta x_{mean} = 0$.

5.3 Results

5.3.1 Morphological transition

In the first step, we focused on the change in global cell shapes before and after the perfusion of endotoxins (Figure 5.6(a)). As exemplified in the figure, an adult RBC changed its shape after the perfusion of $100 \mu\text{g}/\text{mL}$ LPS Ra and $1 \text{ mg}/\text{mL}$ P19 from (i) normal discocyte shape to (ii) faceted shape and (iii) echinocyte shape under the exposure to endotoxin. Figure 5.6(b) shows the fraction of the faceted cells and echinocytes in adult and neonatal RBCs in the presence of $100 \mu\text{g}/\text{mL}$ lipid A, LPS Re and LPS Ra after 15 min incubations. As presented in Figure 5.6(b), both adult and neonatal discocytes were more transformed to echinocytes when the saccharide head groups of endotoxins became longer, but neonatal RBCs were much more susceptible to endotoxins (Figure 5.6(b), red): The fractions of neonatal RBCs that underwent echinocytosis by the exposure to each endotoxin were more than the double of the corresponding values for adult RBCs. In fact, more than one-half of neonatal RBCs underwent echinocytosis in contact with LPS Re and LPS Ra. It should

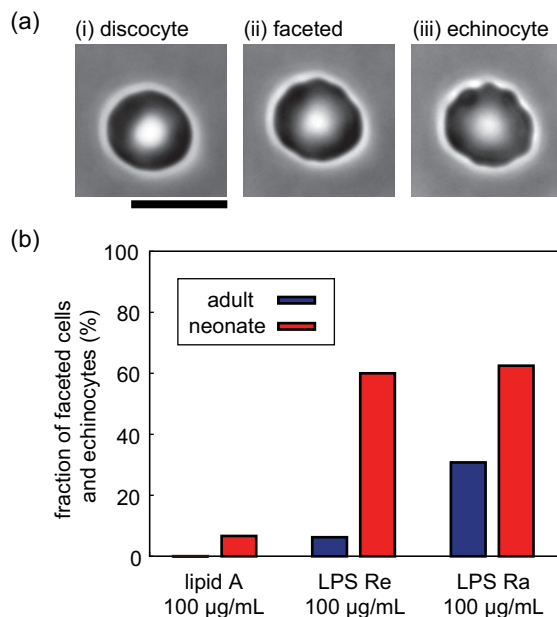


Figure 5.6: (a) Shape variations of a red blood cell after the treatment with endotoxins, ranging from (i) normal discocyte shape to (ii) faceted shape and (iii) echinocyte shape. Note that faceted cells and echinocytes are discriminated from discocytes once the spherical harmonics approximation fails, while there is no clear definition between faceted cells and echinocytes. Scale bar: $10\ \mu\text{m}$. (b) Fractions of the faceted cells and echinocytes in adult (blue) and neonatal (red) red blood cells after the incubation with $100\ \mu\text{g}/\text{mL}$ lipid A, LPS Re, and LPS Ra for $t = 15\ \text{min}$, indicating that neonatal red blood cells are much more susceptible to endotoxins.

be noted that the osmolarity difference of these solutions was not significant: 304.8 ± 10.9 , 298.5 ± 13.0 , and $301.2 \pm 12.1\ \text{mmol}/\text{kg}$ for $100\ \mu\text{g}/\text{mL}$ lipid A, $100\ \mu\text{g}/\text{mL}$ LPS Re, and $100\ \mu\text{g}/\text{mL}$ LPS Ra, respectively (mean \pm SD, $n = 10$).

5.3.2 Quantification of elastic moduli

To elucidate the impacts of endotoxins quantitatively beyond the phenomenological observation of ensembles, we measured the elastic constants of individual RBCs before and after the exposure to endotoxins by flicker spectroscopy. In this study only discocyte-like shape were subjected to the analysis, not only because the rim detection of echinocytes with drastic spicules is difficult but also because the large shape deviation from a smooth shape is no longer suitable for the comparison with the theoretical mean squared amplitude (Eq. (5.2)). Thus, the evaluated values provide with the lower limit of the overall effect of endotoxins on RBCs. To quantify the tendency of scattered mechanical responses of individual cells, which is essential for living matters, we evaluated the relative changes in the mean values of the elastic constants together with their correlation coefficient in the ensembles.

Figure 5.7 shows the individual (gray lines) and the mean (black thick lines) values of spring constant γ , which relates to shear elastic property of the cells, and bending stiffness κ of adult RBCs in the absence and presence of endotoxins, *i.e.*, $100\ \mu\text{g}/\text{mL}$ portions of lipid A, LPS Re, and LPS Ra, respectively. First, lipid A had no impact on the mechanics of

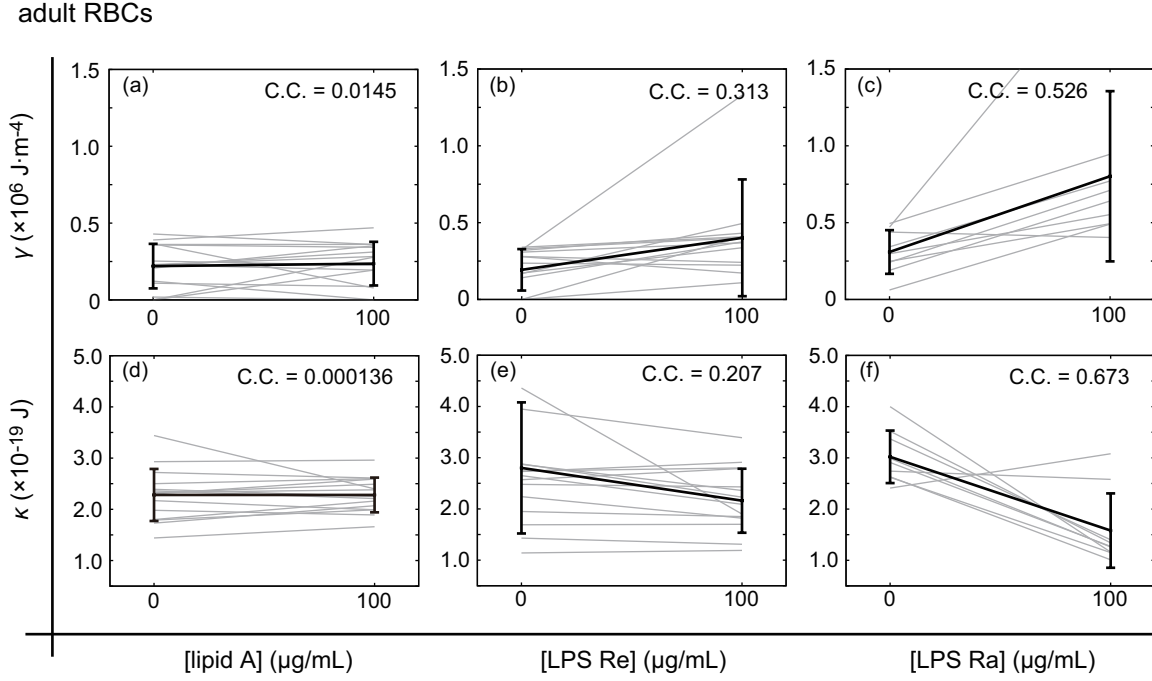


Figure 5.7: Impacts of endotoxins on the elastic properties of adult red blood cells. Individual (gray lines) and the mean (black thick lines) values of the spring constant γ in the absence and presence of $100 \mu\text{g/mL}$ (a) lipid A, (b) LPS Re, and (c) LPS Ra. The errors coincide with the standard deviations. (d–f) Changes in the bending stiffness κ caused by $100 \mu\text{g/mL}$ lipid A, LPS Re and LPS Ra, respectively.

adult RBCs, which seems consistent with our ensemble observation that we found almost no sign of echinocytosis (Figure 5.6(b)). Note that the obtained mean values $\gamma = (2.20 \pm 1.45) \times 10^5 \text{ J/m}^2$, and $\kappa = (2.28 \pm 0.51) \times 10^{-19} \text{ J}$ for the healthy adult RBCs (*i.e.*, no exposure to endotoxin lipid A) were comparable to the previously reported values obtained by fluctuation analyses [95,96]. In contrast, LPSs exhibited an increase in spring constant γ and a decrease in bending stiffness κ , accompanied by larger correlation coefficients. It should be noted that this tendency is much more pronounced for LPS Ra: Relative changes in the mean γ and κ were $\Delta\gamma = +159.2\%$ with the correlation coefficient of the ensemble $C.C. = 0.526$ and $\Delta\kappa = -47.6\%$ with $C.C. = 0.673$, respectively. Our finding implies that adult RBCs exposed to LPSs becomes softer against the bending deformation, meanwhile inflexible in the sense of shear. The increase in cytoskeleton-membrane coupling and thus the shear modulus suggested here qualitatively agrees with the decrease in deformability of RBCs treated with a LPS mutant with intact outer core region (LPS Rd from *Escherichia coli*) measured with a shear stress diffractometer [97]. This suggests that adult RBCs mechanically respond in a different manner against bending and shear stresses. It is notable that changes in the surface tension σ exhibited no systematic tendency in the presence and absence of endotoxins under the present conditions as shown in Fig. 5.8.

Therefore, we focused on the impacts of LPS Ra on spring constant γ and bending stiffness κ in the following discussion.

Parts (a) and (b) of Figure 5.9 show the individual (gray lines) and the mean (black thick lines) values of γ and κ of neonatal RBCs in the presence and absence of $100 \mu\text{g/mL}$ LPS Ra.

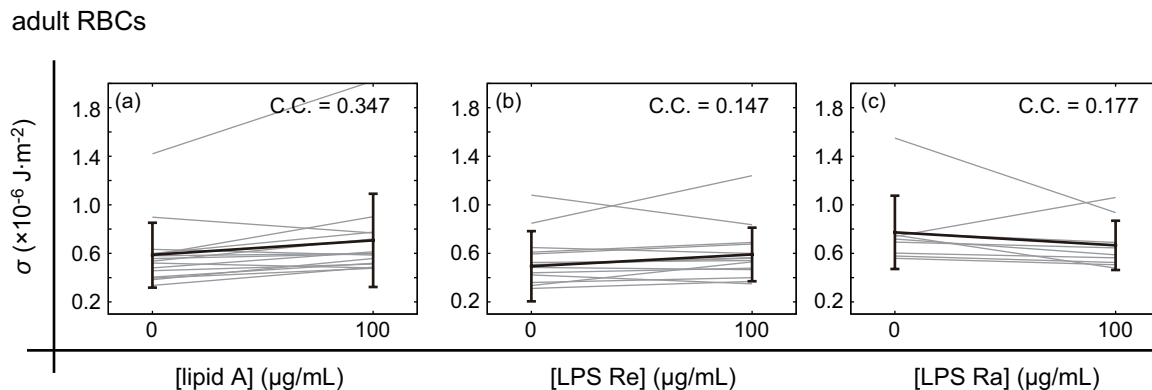


Figure 5.8: Impacts of endotoxins on the surface tension σ of individual adult red blood cells. Individual (gray lines) and the mean (black thick lines) values in the absence and presence of 100 $\mu\text{g}/\text{mL}$ lipid A, (b) LPS Re and (c) LPS Ra. The errors coincide with the standard deviations. There was no systematic tendency in the relative change in the surface tension.

Relative changes in γ and κ exhibited the same tendency as those observed for adult RBCs. However, as shown in Figure 5.9(c), relative changes in γ and κ of neonatal RBCs were more pronounced compared to those of adult RBCs. This finding seems reasonable from the fraction of RBCs undergoing echinocytosis, indicating that neonatal RBCs were more susceptible to endotoxins. The relative changes in the surface tension σ , again, exhibited no systematic tendency in the presence and absence of LPS Ra under the present conditions as shown in Fig. 5.10(a). Therefore, together with the results of adult RBCs, it was found that the surface tension of RBCs is not influenced by endotoxins.

Furthermore, we investigated a possible curative effect of anti-septic peptide P19 after incubation with LPS Ra in a microfluidic diffusion chamber. Figure 5.11(a) shows the fractions of faceted RBCs and echinocytes before and after perfusion of 1 mg/mL P19 peptide accompanied by 100 $\mu\text{g}/\text{mL}$ LPS Ra for adult and neonatal RBCs. The obtained results suggest P19 does not have neither toxicity to the discocyte shape nor curative effects on echinocytosis. However, the calculated mechanical parameters clearly indicate the curative effect of P19. Figure 5.11(b) and 5.11(c) show the relative changes in spring constant γ and bending stiffness κ caused by the perfusion of endotoxins. After perfusion of 1 mg/mL P19, both the relative changes in spring constant and bending stiffness slightly decreased: For adult RBCs $\Delta\kappa$ decreased from -47.6% ($C.C. = 0.673$) to -39.2% ($C.C. = 0.529$), and the corresponding values of neonatal RBCs were from -60.5% ($C.C. = 0.619$) to -61.6% ($C.C. = 0.665$). On the other hand, $\Delta\gamma$ for adult RBCs decreased from $+159.2\%$ ($C.C. = 0.526$) to $+131.5\%$ ($C.C. = 0.506$), and from $+268.2\%$ ($C.C. = 0.599$) to $+179.61\%$ ($C.C. = 0.278$) for neonatal RBCs.

5.4 Discussion

Shape fluctuation and mechanics of cells have been of great interest within the framework of active soft matter physics. Betz *et al.* measured the power spectral density as a function of frequency in the presence and absence of ATP [67]. They reported that the equilibrium description breaks down at a characteristic frequency, and estimated the changes in “ef-

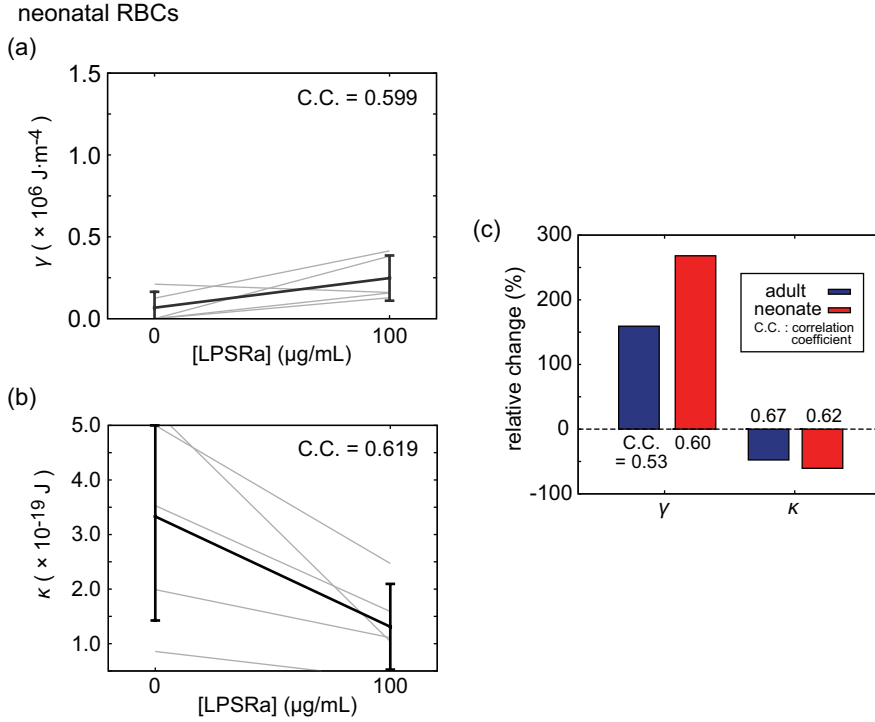


Figure 5.9: Changes in (a) spring constant γ and (b) bending stiffness κ of neonatal red blood cells caused by the additions of $100 \mu\text{g}/\text{mL}$ LPS Ra. The correlation coefficients $C.C.$ are shown in the upper right of the graph. (c) Relative changes in the spring constant and bending stiffness caused by $100 \mu\text{g}/\text{mL}$ LPS Ra, suggesting that the impact of endotoxins (LPS) to the mechanics of discocytes are similar but more pronounced for neonatal red blood cells (red) compared to the adult red blood cells (blue).

fective temperature”. With aid of beads biochemically attached to cell surfaces, nonlinear frequency-response of RBCs can be monitored by fluctuation analysis [98]. In fact, such nonlinear response functions have been reported in various biological systems, such as isolated actomyosin complexes [99] and cytoplasm in living cells [100]. In this study, we analyzed the ATP-dependent coupling between cytoskeletons and cell membranes via spatial fluctuation spectra [66, 67, 71, 101].

5.4.1 Physical mechanism of echinocytosis

As presented in Figure 5.6, we found that both adult and neonatal RBCs undergo a morphological transition from normal discocyte to echinocyte when they are in contact with endotoxin (LPSs). Lim *et al.* explained this morphological transition in terms of the shape-free-energy functional that includes the bending energy of cell membranes, as well as the cytoskeletal elastic energy for stretching and shear [102]. It has been demonstrated that the morphological transition to echinocyte could be reproduced by increasing the area difference between inner and outer leaflets. In our experiments, LPS molecules with six hydro-carbon chains, which are similar or shorter in lengths (C12 and C14) than those of the cell membrane lipids [103], are incorporated into the cell membranes via perfusion from the bulk solution but not from inside, leading to an increase in the area of the outer leaflet [104, 105].

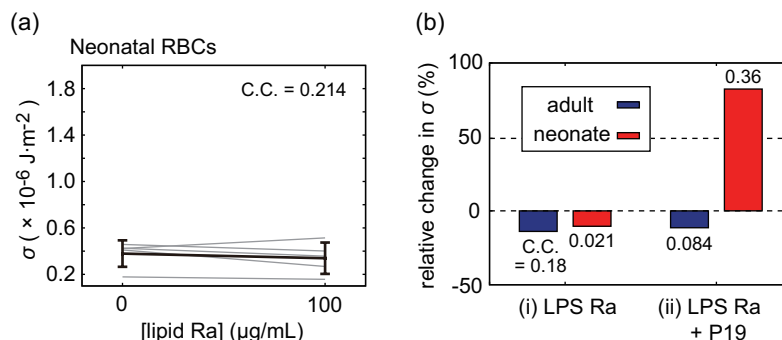


Figure 5.10: (a) Changes in the surface tension of neonatal red blood cells caused by the additions of $100 \mu\text{g}/\text{mL}$ LPS Ra. (b) Relative changes in the surface tension caused by (i) $100 \mu\text{g}/\text{mL}$ LPS Ra and (ii) the addition of $1 \text{ mg}/\text{mL}$ P19, suggesting that for both adult red blood cells (blue) and neonatal red blood cells (red) there was no systematic tendency in the relative change in the surface tension.

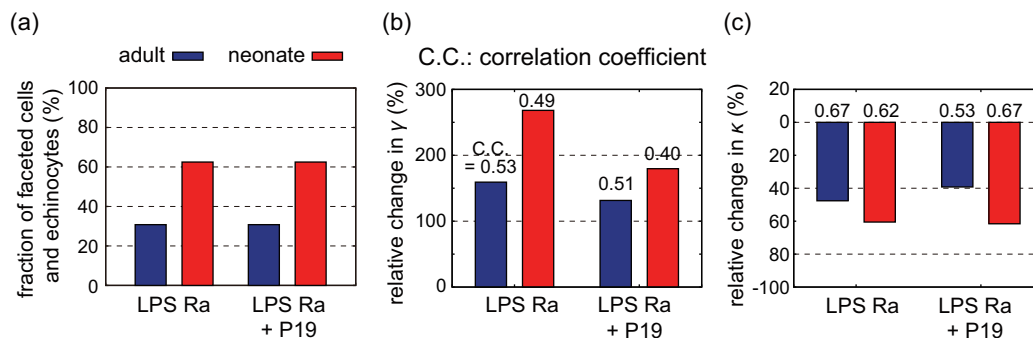


Figure 5.11: Impacts of anti-septic peptide P19 on the elastic properties of adult (blue) and neonatal (red) red blood cells, which were pretreated with $100 \mu\text{g}/\text{mL}$ LPS Ra. (a) Fractions of the faceted cells or echinocytes, relative changes in (b) spring constant γ and (c) bending stiffness κ caused by the addition of P19 ($1 \text{ mg}/\text{mL}$). The correlation coefficients are shown above the corresponding bars.

Since the inner leaflet remains almost intact due to a negligibly little probability for flip-flop in our experimental time window, the difference in surface areas would serve as the driving force of the morphological transition. In fact, there have been several reports on the morphological transition of RBCs accompanied by the abnormality of lipid compositions caused by diseases like sickle cell anemia [106]. Therefore, the decrease in the bending stiffness we observed could be attributed to the lateral expansion of the outer leaflet caused by the incorporation of LPS molecules from the outside.

Previously, Warren *et al.* reported that the interaction of endotoxin and transmembrane band-3 as well as the incorporation of endotoxin molecules into the outer leaflet of RBC membranes could cause echinocytosis [107]. A more recent study demonstrated an elevated level of band-3 phosphorylation in septic mice, suggesting that the exposure to endotoxin increases the level of ATP consumption [108]. Therefore, it is plausible that the endotoxin-induced echinocytosis is a consequence of two effects: (i) the decrease in the bending stiffness κ by asymmetric incorporation of endotoxins into the outer leaflet, and (ii) the increase in

spectrin-membrane coupling γ caused by the binding of endotoxin to band-3. The latter scenario needs to be verified by more precise determination of ATP level during the exposure to endotoxin.

5.4.2 Mechanics of adult and neonatal RBCs

The quantitative fluctuation analysis enables one to calculate the principal parameters describing the mechanics of not only adult (Figure 5.7) but also neonatal RBCs (Figure 5.9), although one cannot completely exclude a possibility that the changes in the parameters of echinocyte RBCs can be larger than those analyzed here for discocyte RBCs. Taking the theoretical model including bending stiffness κ , surface tension σ , and spring constant between membranes and cytoskeletons γ (Eq. (5.2)) [65], we analyzed the experimentally measured mean square amplitude of closed cell membranes by eliminating the smaller wave numbers $\langle r \rangle q < 3$. First, we found that the bending stiffness and surface tension of neonatal RBCs are comparable to those of adult RBCs. On the other hand, the spring constant γ of neonatal RBCs is by 3–5 times smaller than that of adult RBCs. The shear elasticity of RBCs is dominated by that of the spectrin meshwork coupled to the membranes [67, 84]. Since the spring constant γ is directly correlated to the shear modulus of RBCs, $\mu = A\gamma$ [65], where $A \sim 100 \mu\text{m}^2$ is the surface area of a RBC, this finding suggests that the shear modulus of neonatal RBCs is smaller than that of adult RBCs.

On the basis of the fitting in the previous study, Yoon *et al.* reported that the influence of spring constant γ is negligibly smaller compared to bending stiffness κ and surface tension σ . This fact and Eq. (5.2) set an upper limit of spring constant γ for untreated adult RBCs to be $\gamma < 5 \times 10^5 \text{ J/m}^4$, corresponding to the upper limit of shear modulus $\mu < 3 \times 10^{-5} \text{ N/m}$ [65]. Actually, the mean values of γ for untreated adult RBCs that we calculated from the experimental results lies in the order of 10^5 J/m^4 , which coincides with the shear modulus of $\mu \sim A\gamma \sim 10^{-5} \text{ N/m}$. This value is in good agreement with those measured by flicker spectroscopy [95] and by other techniques such as micropipet aspiration [59, 109]. Therefore, we concluded that γ should not be neglected in the fluctuation analysis.

In fact, we confirmed that the values of spring constant γ were properly obtained by performing the additional fittings in the absence of γ in Eq. (5.2), and by comparing the results with those in the presence of γ . Figure 5.12(a–f) shows the additional fitting results for bending stiffness κ and surface tension σ in the absence of γ . As summarized in Fig. 5.12(g)(i) and (g)(ii), bending stiffness κ clearly decreased in both absence and presence of the spring constant γ under the influence of endotoxins according to the elongation of sccharide chains, whereas surface tension σ did not show any clear tendency and the relative changes were much smaller than those of bending stiffness κ . The important point is that the relative changes in spring constant γ systematically increased according to the elongation of sccharide chain length, although surface tension, which was also obtained in the low q regime, was almost constant. Therefore, the measurement of the relative spring constant γ was proved to be independent of the measurement of surface tension σ .

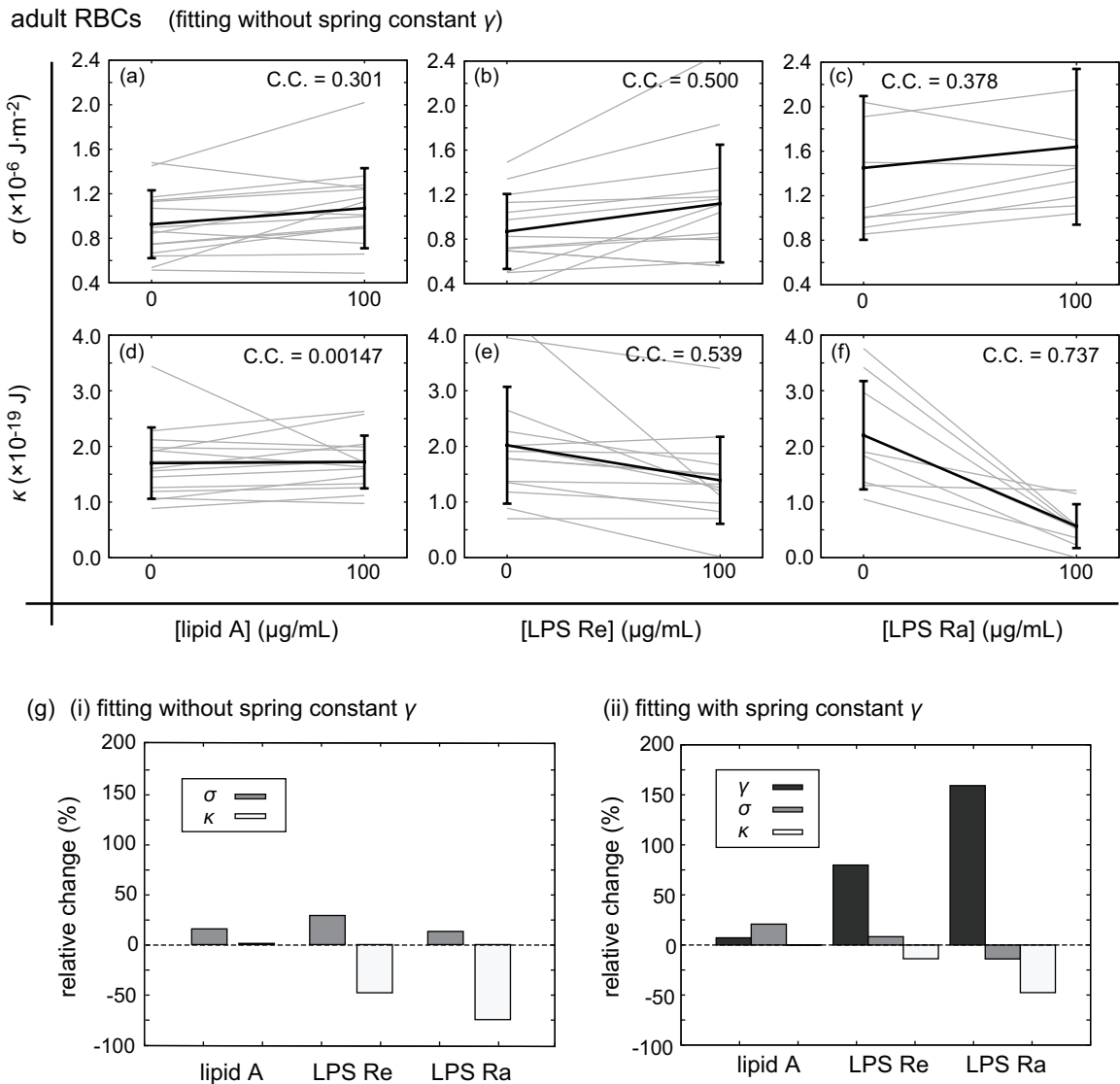


Figure 5.12: Comparison of the fittings with γ and those without γ . (a) Impacts of endotoxins on the elastic properties of adult red blood cells. Individual (gray lines) and the mean (black thick lines) values of the spring constant γ in the absence and presence of $100 \mu\text{g}/\text{mL}$ lipid A, (b) LPS Re and (c) LPS Ra. The errors coincide with the standard deviations. (d-e) Changes in the bending stiffness κ caused by $100 \mu\text{g}/\text{mL}$ lipid A, LPS Re and LPS Ra, respectively. (g) Relative changes in (i) σ and κ in the absence of γ and (ii) γ , σ and κ in the presence of γ . In summary, the impact of endotoxin on σ was not significant compared to those on γ and κ , while γ increased and κ decreased according to the elongation of saccharide chains.

In addition to the above proof, we checked the coefficient of determination to verify the present fittings with the spring constant γ in Eq. (5.2) is sufficiently good. Coefficient of determination was calculated as 1 minus the normalized sum of squares of residuals:

$$\eta_d^2 = 1 - \frac{\sum_m (y_m - \hat{y}_m)^2}{\sum_m (y_m - \langle y \rangle)^2}, \quad (5.4)$$

where y_m , \hat{y}_m , and $\langle y \rangle$ are the experimental value of MSA of m th mode ($m \geq 3$), corresponding theoretical value, and the averaged value of y_m over $m \geq 3$, respectively. The coefficient η_d^2 ranges from 0 (complete failure in matching to Eq. (5.2)) to 1 (complete matching to Eq. (5.2)). All the fittings were accompanied with quite high coefficients of determination (above 0.999). Note that the fitting with γ slightly improves the fitting qualities because of the increase in the number of free parameters.

Table 5.1: Coefficients of determination η_d^2 in the case of fittings with spring constant γ (mean \pm standard deviation)

	0 $\mu\text{g/mL}$	100 $\mu\text{g/mL}$	+ P19 1 mg/mL
lipid A	0.99990 \pm 0.00008	0.99992 \pm 0.00006	-
LPS Re	0.99992 \pm 0.00006	0.99985 \pm 0.00022	-
LPS Ra	0.99929 \pm 0.00152	0.99964 \pm 0.00023	0.99951 \pm 0.00076

Table 5.2: Coefficients of determination η_d^2 in the case of fittings without spring constant γ (mean \pm standard deviation)

	0 $\mu\text{g/mL}$	100 $\mu\text{g/mL}$	+ P19 1 mg/mL
lipid A	0.99984 \pm 0.00013	0.99989 \pm 0.00007	-
LPS Re	0.99988 \pm 0.00008	0.99977 \pm 0.00024	-
LPS Ra	0.99978 \pm 0.00018	0.99926 \pm 0.00047	0.99950 \pm 0.00019

The experimentally obtained mean value for untreated neonatal RBCs, $\gamma \sim 5 \times 10^4 \text{ J/m}^4$, is distinctly smaller than that of adult RBCs [110]. Previously, Linderkamp *et al.* demonstrated that neonatal RBCs are more deformable than adult RBCs with a smaller shear modulus [77, 110]. Here, an increase in deformability coincides with a decrease in shear modulus, since the deformability was defined from the aspect ratio under shear flow. Although the deformability cannot be translated numerically to mechanical parameters, we found that the calculated shear modulus of neonatal RBCs, $\mu \sim 10^{-6} \text{ N/m}$, was actually 3–5 times smaller than that of adult RBCs. Thus, our quantitative experimental finding seems consistent with the cell deformation under micropipet aspiration. The mechanism of this

softness of neonatal RBCs against shear deformation is still an open question. As one factor that could significantly influence the cell mechanics is the cytoskeletal remodeling powered by ATP hydrolysis, the large deformability of neonatal RBCs suggests that neonatal RBCs might contain higher amount of ATP. Previously, Kodama reported that the mean ATP concentration in neonatal blood is slightly lower than that in adult blood up to 4 h after the birth and increases to the comparable level to the adult after 1 d [111]. This suggests that the softness of neonatal RBCs cannot be explained by the ATP concentration difference. Therefore, our experimental finding suggests that ATP concentration is not the dominant factor that causes the difference in stiffness between neonatal and adult RBCs.

5.4.3 Impact of molecular chemistry

If one focuses on the impact of molecular structures of different LPSs on cell mechanics, the changes in the mechanical parameters, *i.e.*, the decrease in κ and the increase in γ , were monotonically magnified according to the elongation of saccharide chain length (Figure 5.7). Our finding, the decrease in κ by the exposure to LPSs, seems contradictory to our previous off-specular neutron scattering study on the LPS multilayers, where we found that the elongation of saccharide head groups of LPSs results in the increase in bending stiffness κ [112]. However, this apparent discrepancy can actually be explained if one takes the symmetry of membranes into account. Pure LPS membranes deposited on solid substrates for neutron scattering are symmetric, and thus the thickening of membranes due to the elongation of saccharide chain length results in an increase in the bending stiffness. On the other hand, LPS molecules are asymmetrically incorporated into the outer leaflet of RBC membranes. The asymmetric incorporation of “bulky” LPS molecules leads to a disordering of membrane lipids, which is supposed to cause a decrease in the bending stiffness. Indeed, the micropipet experiments by Evans and Rawicz demonstrated that the decrease in bending stiffness is caused by the decrease in lateral packing of lipids [42].

If one compares the impact of LPS Ra on the RBC mechanics (Figure 5.9(c)), neonatal RBCs were found to be slightly more susceptible than adult RBCs, which can be characterized by a larger change in the spring constant γ . This finding suggests that LPSs would interact more strongly to neonatal RBCs and interfere with the coupling between spectrin cytoskeleton and cell membranes.

5.4.4 Impact of P19

We extend our approach by investigating the function of the peptide-based antiseptic drug P19. As presented in Figure 5.11, it was found that the coincubation of P19 with LPS Ra slightly reduced the impact of LPS Ra on RBC mechanics. Recently Abuillan *et al.* reported that P19 interacts much more significantly with LPS Ra compared to the naturally occurring cationic antibacterial peptide (herring protamine) [92]. The stoichiometry of the reaction between P19 and LPS Ra determined by grazing incident X-ray fluorescence (about 1:3) was in excellent agreement with that obtained by isothermal titration calorimetry [87, 113, 114]. The previous studies reported that anti-septic peptide P19 has a strong binding capability to endotoxins, resulting in the formation of multilamellar P19-LPS complexes in bulk [87]. Therefore, the added P19 in bulk could result in a slight but distinct protection function against endotoxin insertion into RBC membranes by decreasing the equilibrium concentration of endotoxin molecules in the membranes. Moreover, the shape analysis (Figure 5.11(a)) and the correlation coefficient analysis of relative changes (Figure 5.11, parts (b) and (c))

suggest that the protection functions of P19 were slightly more significant for neonatal RBCs than for adult RBCs. However, it should be noted that the mechanical parameters of RBCs treated with LPS Ra and P19 were clearly different from those of untreated RBCs. Thus, we conclude that the LPS-P19 interaction is not strong enough to keep RBCs completely intact.

5.5 Conclusion

We presented a quantitative modeling of sepsis symptoms by calculating the mechanical properties of human RBCs from its shape fluctuation in the absence and presence of endotoxins (lipid A, LPS Re, LPS Ra) by the combination of noninvasive flicker spectroscopy and a microfluidic diffusion chamber. As sepsis is a life-threatening disease for neonates, we monitored for the first time the mechanical response of neonatal RBCs, in systematical comparison with adult RBCs. First, it was found that adult RBCs undergo a shape change, *e.g.*, morphological transition, from discocytes to echinocytes in the presence of endotoxins. In the next step, we calculated the mechanical parameters (bending stiffness κ , surface tension σ , and spring constant representing membrane-cytoskeleton coupling γ) of RBCs and found that exposure of RBCs with endotoxins leads to an increase in γ and a decrease in κ . Interestingly, the mechanical impact caused by endotoxins monotonically increased with the elongation of saccharide head groups. Neonatal RBCs were more susceptible to these effects of the endotoxins than adult RBCs. We also confirmed that the anti-septic peptide P19 can slightly suppress the effects of the endotoxin. The combination of flicker spectroscopy and a microfluidic device used here can noninvasively extract the elastic properties and their temporal variation by updating the surrounding condition, which allows for the physical diagnosis of suspended cells in contact with drugs and toxins based on mechanics. As a conclusive remark of this results by flicker spectroscopy and microfluidics, the drastic change in spring constant γ clearly highlights the spectrin cytoskeletal function. The confinement effect of spectrin should be taken into account when the RBCs respond to the external stimuli, which is the great ability of biological interfaces.

Part III

Active shape fluctuation and deformation caused by actomyosin

Chapter 6

Active shape fluctuation caused by actomyosin

In Part II, we described the fluctuation and the deformation of a biological interface of a red blood cell under thermal equilibrium. In Part III, we in turn discuss athermal motion of biological interfaces. The active motions, the fluctuation and the deformation, accompanied by internal force generations of the interface is one of the most remarkable characters of living matters. In various biological processes in living organisms, active force generation, which is mainly involved in actin cytoskeleton and myosin molecular motors, plays crucial functional roles. Although the contractile properties of actomyosin have been extensively investigated, their dynamic contribution to a deformable membrane remains unclear because of the cellular complexities and the difficulties associated with *in vitro* reconstitution. Here, by overcoming these experimental difficulties, we demonstrate the dynamic deformation of a reconstituted lipid interface coupled with self-organized structure of contractile actomyosin. Therein, the lipid interface repeatedly oscillates without any remarkable periods. The oscillatory deformation of the interface is caused by the aster-like three-dimensional hierarchical structure of actomyosin inside the droplet, which is revealed that the large amplitude appears stochastically as a Poisson process. Finally, the nature of the generated active forces are discussed.

6.1 Introduction

Eukaryotic cells show a variety of shapes to carry out the highly specific biological functions [2, 115, 116]. In addition, their shapes are not static but successively changing in response to internal and external environmental factors in ordinary biological phenomena [117–119]. As is well known, actomyosin (actin and myosin) proteins play critical roles in these deformations [118, 120–123]. Myosin II protein, a motor protein which runs directionally on an actin filament, is involved in the force generation in cellular morphological changes. In a physiological condition, myosin II molecules assemble into bipolar thick filament. Since each end of the bipolar thick filament runs toward the opposite direction in a cooperative manner, coexistence of actin filaments and myosin thick filaments leads contraction of the network of the actomyosin complex [124, 125]. The rheological and non-equilibrium property of actomyosin network during contraction have been measured by passive- and active-microrheology methods [126–128]. This contractile force generated by the actomyosin must be transmitted to a cellular membrane to exhibit deformation of

the cell shape and migration of the cell body. Although various types of regulation factors concern with the actomyosin, lots of active motion of cell basically originates in the force generation from actomyosin, such as a cleavage furrow induced by contractile ring during cytokinesis [120, 121, 124], membrane protrusion caused by contraction of cell cortex during bleb-driven locomotion [122, 123], and retraction at posterior region of cell during cell migration on a substrate [129–131]. On the other hand, to elucidate the native properties of the actomyosin as a soft material, *in vitro* systems with only a small number of cellular components have been developed. For example, hierarchical structure of actin filaments were presented in two-dimensional motility assay systems, where the actin filaments are driven by myosin motors fixed on a solid substrate [132, 133]. In the case of initially dispersed actin and myosin in a solution, the actin filaments and myosin thick filaments form the actomyosin complex, and further aggregate into an aster-like hierarchical structure in bulk [134] and inside a cell-sized lipid vesicle [135]. As a more realistic model system, Carvalho *et al.* reported that cortex-like structure of actomyosin that is anchored to the inner surface or outer surface of lipid vesicles by biotin-avidin interaction, results in peeling of the actomyosin cortex from the inner or outer surfaces of the vesicles, crushing of the vesicle (outside-geometry), or spherical aggregation inside the vesicle (inside-geometry) [136].

These experiments have verified the active and contractile properties of the system composed of actin and myosin, and their characteristic structural formation under certain boundary conditions. However, the dynamic deformation of membranes caused by the continuous remodeling of the contractile actomyosin, where the actomyosin distribution and contractility should interact with the membrane elasticity and interfacial tension, remains as a crucial open question. It is because of a technical problem: Suitable connection between a lipid membrane and contractile actomyosin was difficult to reconstitute *in vitro*. In addition, the difficulty in encapsulation of biopolymers, such as actin and myosin, at biologically-relevant concentrations of the order of mg/mL inside a lipid bilayer vesicles have been one of the major obstacles [137, 138] to reconstitute a sufficient amount of the connection. In the present study, we have successfully reconstituted a simple model system with a cell-sized deformable lipid interface that is connected to contractile actomyosin in a non-specific manner. We have demonstrated, for the first time, the dynamical repetitive deformation of the spherical interface, which continued for several tens of minutes, coupled with the structural formation of the encapsulated actin and myosin.

6.2 Materials and methods

6.2.1 Cell culture

Mass culture of *Amoeba proteus* was performed as described previously [139]. Briefly, *Amoeba proteus* was cultured in KCM medium (7 mg/L KCl, 8 mg/L CaCl₂, and 8 mg/L MgSO₄·7H₂O) at 25°C and fed with *Tetrahymena pyriformis* twice a week. To avoid contamination of undigested *T. pyriformis*, cells were starved for at least 3 days before use.

6.2.2 Preparation of actomyosin fraction

All the following preparations were performed at 2°C to avoid disfunction of actin and myosin proteins. The actomyosin fraction was prepared by modifying a previously described method [140]. A portion of *A. proteus* (10 g) suspended in a cell washing solution (2 mM O,O'-bis(2-aminoethyl)ethyleneglycol-N,N,N',N'-tetraacetic acid (EGTA), 2

mM MgCl₂, and 20 mM piperazine-1,4-bis(2-ethanesulfonic acid) (PIPES)-KOH, pH 7.0) was first centrifuged at 6000×*g* for 2 min. After the supernatant was removed, the resultant precipitate was centrifuged at 600000×*g* for 20 min to obtain an actin rich solution. Next, the precipitate was suspended in a 3 M KCl solution (3 M KCl, 2 mM MgCl₂, 1 mM threo-1,4,-dimercapto-2,3-butanediol (DTT), 20 mg/mL leupeptin, 20 mg/mL pepstatin A, 0.2 mM phenylmethylsulphonyl fluoride (PMSF), 20 mM imidazole-HCl, pH 7.0) and centrifuged at 400000×*g* for 10 min. The obtained supernatant was dialyzed against 50 mM KCl, 2 mM EGTA, 2 mM MgCl₂, 1 mM DTT, 0.2 mM PMSF, 20 mM imidazole-HCl, pH 7.0, for 5 h. The dialyzed specimen was centrifuged at 20000×*g* for 5 min, and the precipitate was suspended in a 270 mL EMPA solution (5 mM EGTA, 6 mM MgCl₂, 1 mM DTT, 2 mM adenosine-5'-triphosphate (ATP), 30 mM PIPES-KOH, pH 7.0), and the actin rich solution (30 mL) was added. The resultant fraction dissolving the actomyosin contains 4.5 mM EGTA, 5.4 mM MgCl₂, 0.9 mM DTT, 1.8 mM ATP, and 27 mM PIPES. The protein concentration in the actomyosin fraction was determined by Bradford assay [141] with bovine serum albumin as the standard, where the measured concentration of actin and myosin were 3 mg/mL and 6 mg/mL respectively. In addition, we also confirmed the concentrations of these proteins using absorbance at 280 nm and muscle actin/myosin extinction coefficients. The estimated values of actin and myosin concentration were 2.3 mg/mL and 6.2 mg/mL, which corresponded to 2.55 and 2.73 of absorbance of actin and myosin, respectively. The concentration of actin and myosin were calculated from total protein concentration and ratio of actin or myosin to total proteins using SDS-PAGE [142] and the Fiji software package (<http://fiji.sc/wiki/index.php/Fiji>). Actin and myosin were determined by immunoblotting using anti-β-Actin (Poly6221; BioLegend) and anti-Myosin II from *A. proteus*. Horseradish peroxidase (HRP)-conjugated secondary antibodies (Poly4053 and Poly4064; BioLegend). In the experiments with ATP regeneration system, 0.2 mg/mL creatine phosphokinase (Sigma aldrich) and 0 mM to 30 mM phosphocreatine (Nacalai tesque) were added as the final concentrations in the actomyosin fraction.

6.2.3 Preparation and observation of actomyosin droplets

Cell-sized water-in-oil (W/O) droplets with a lipid monolayer were prepared using a previously described method [23, 143]. In brief, 1,2-dioleoyl-3-trimethylammonium-propane chloride (DOTAP; Avanti Polar Lipids) was dissolved in chloroform at a concentration of 10 mM. The chloroform was dried at a bottom of a glass tube under a nitrogen stream and put under vacuum overnight to form a dry film of lipids. Mineral oil (Nacalai tesque) was added to the films and then sonicated at 60°C for 60 min, resulting in dispersed 1 mM DOTAP in oil. Finally, a 3% (v/v) actomyosin fraction was added to the oil solution with lipids, and emulsification was performed by vortexing and pipetting to form cell-sized W/O droplets of actomyosin fraction. The obtained droplets were observed using an optical microscope (Eclipse Ti; Nikon) at room temperature and recorded using a sCMOS camera (ORCA-Flash4.0; Hamamatsu). The distribution of actomyosin fraction inside a droplets was observed by the actin filaments stained with 10 nM Acti-stain 488 phalloidin (Cytoskeleton). Note that the phalloidin prevents actin filaments from depolymerizing. Since the presence and absence of phalloidin did not influence on the oscillatory and wrinkling behaviors, actin polymerization and depolymerization were not crucial in the present repetitive deformations. Time-lapse images of the stained actin filaments were collected using a microscope (IX71; Olympus) equipped with an EM-CCD camera (iXon; Andor) and a confocal scanner unit (CSU-X1; Yokogawa). In experiments of droplets in the absence of

myosin molecules, a mixture of 300 μL EMPA solution and 30 μL actin-rich solution was used in place of the actomyosin fraction in the above-described procedure. To visualize the actomyosin structure near the interface during the non-periodic oscillation regime, actomyosin droplets stained by fluoresceinated lifeact peptide [144] and by fluorescent lipids were fixed by formalin at the oscillatory period to be observed by confocal fluorescence microscope. In detail, equal volumes of formalin (15% (w/w)) and mineral oil were well mixed and centrifuged at $6000\times g$ for 5 min. Supernatant was collected and preserved at 2°C , which was named a fixing oil. The oscillating actomyosin droplets, which stained by 1 $\mu\text{g}/\text{mL}$ Carboxytetramethylrhodamine-lifeact (purchased from Eurofinsgenomics) and 2.5 μM ATTO 488 labeled DOPE (ATTO-TEC), were prepared by above mentioned method and cooled on ice after checking the occurrence of oscillation. Equal volume of fixing oil to the specimen was gently added, mixed and left for 30 min on ice. Then fluorescence of actin and interface were observed with a microscope (IX71; Olympus) equipped with a sCMOS camera (Zyla 4.2; Andor) and a confocal scanner unit (CSU-X1; Yokogawa) at room temperature. The obtained images were processed via Fiji and analyzed via custom routine developed in Igor Pro (WaveMetrics, Portland, OR).

6.3 Results

6.3.1 Reconstitution of actomyosin droplets

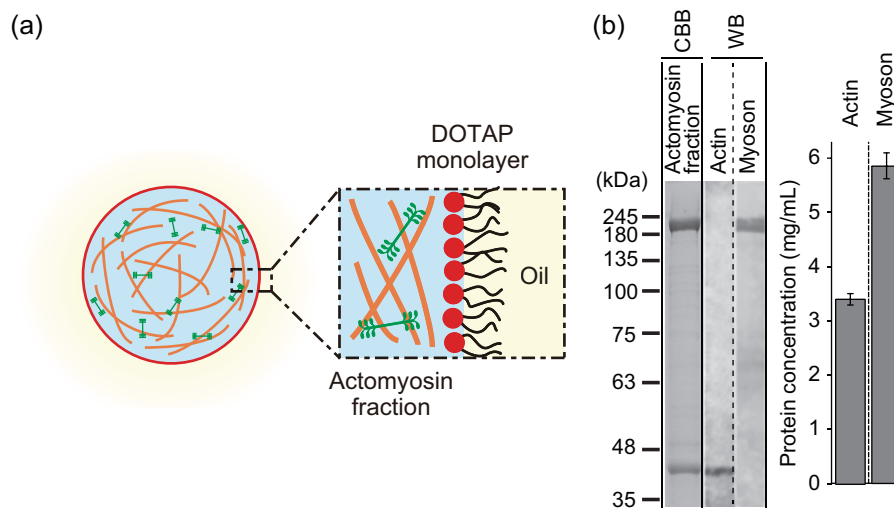


Figure 6.1: (a) Schematic illustration of a cell-sized water droplet of the actomyosin fraction, enclosed with a lipid monolayer. (b) Characterization of the actomyosin fraction; error bars represent the standard error of the mean calculated from 5 experiments ($n = 5$).

Figure 6.1(a) shows a schematic illustration of the present model system, a cell-sized water-in-oil droplet encapsulating actin and myosin II extracted from *Amoeba proteus* as shown in Fig. 6.1(b) (see Methods for detail). As a non-specific interconnection between the actomyosin and the inner surface of the membrane, we adapted electrostatic attrac-

tion between negatively-charged actin together with myosin as an actomyosin complex and positively-charged lipid DOTAP at the oil/water interface. The suitable conditions for the dynamic deformation were examined with respect to the concentrations of actin and myosin, as well as the fraction of DOTAP. The concentration-dependent actin distribution inside a droplet confirmed that 3 mg/mL actin was the most suitable to form the uniform cortex-like structure attracted at the interface by the pure DOTAP monolayer, while the higher concentration of actin than 3 mg/mL led to homogeneous distribution inside the aqueous phase (Fig. 6.2). Accompanied with 3 mg/mL actin, 6 mg/mL myosin caused the interfacial

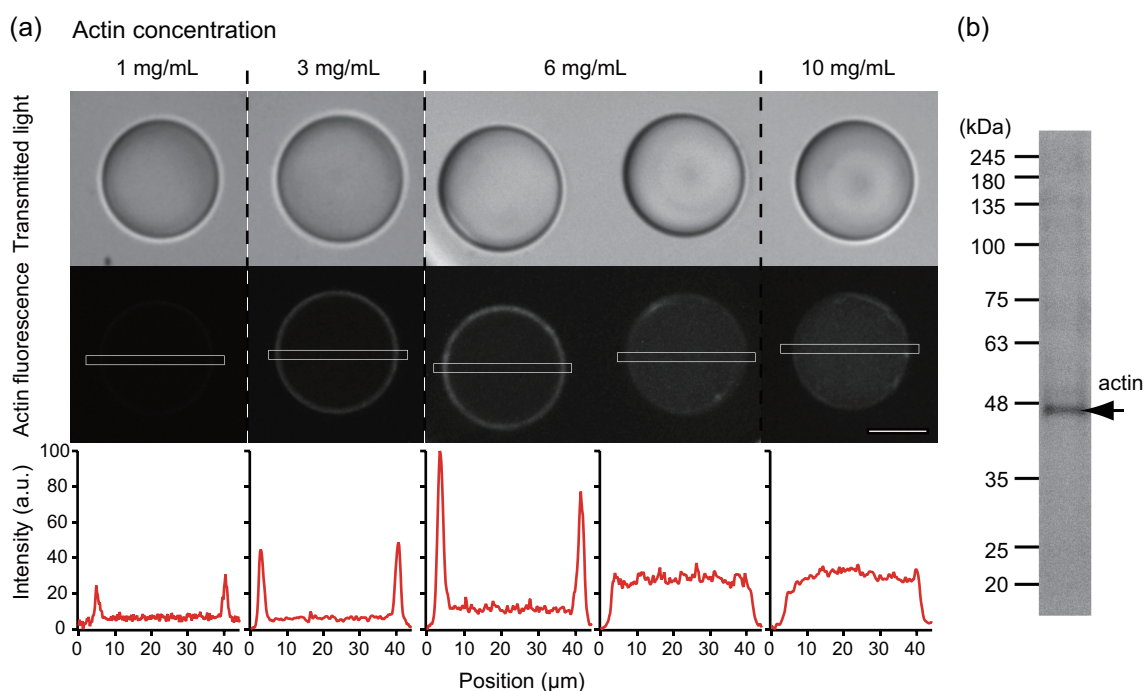


Figure 6.2: (a) Various actin distributions inside the droplets at actin concentrations 1 mg/mL, 3 mg/mL, 6 mg/mL, and 10 mg/mL. (Top) Transmitted light images, (Middle) the corresponding confocal fluorescence images of actin distributions, and (Bottom) the fluorescence intensity distribution in the regions enclosed with the white boxes on the above confocal fluorescence images. 3 mg/mL actin effectively formed actin cortex underlying the interface, while at the higher concentrations actin tends to be homogeneous inside the droplets. Note that the droplets did not deform because myosin was absent. Scale bar is 20 μm . (b) Characterization of actin protein used in (a).

deformation the most efficiently (Fig. 6.3).

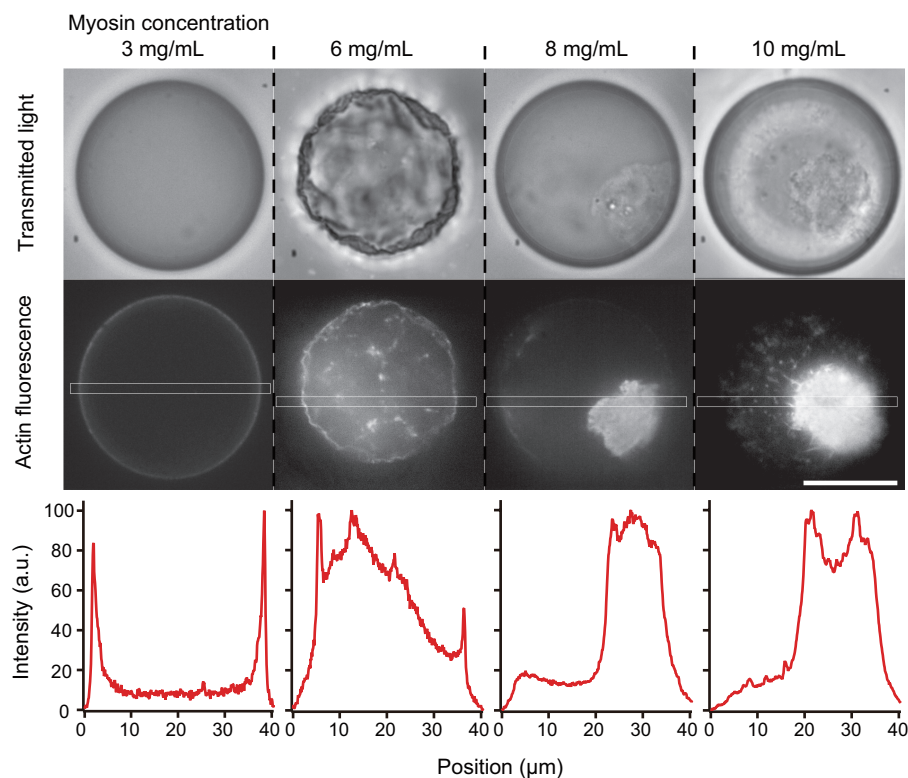


Figure 6.3: Various actin distributions in the presence of myosin at myosin concentrations 3 mg/mL, 6 mg/mL, 8 mg/mL and 10 mg/mL. (Top) Transmitted light images, (Middle) the corresponding confocal fluorescence images of actin distributions and (Bottom) fluorescence intensity distribution at the regions enclosed with the white boxes on the above confocal fluorescence images. Actin concentration was fixed as 3 mg/mL. 6 mg/mL myosin effectively caused contraction and interfacial deformation, while it did not or it detached and aggregated at the aqueous phase in the cases of lower or higher myosin concentrations, respectively. Scale bar is 20 μm .

Compared to the result in the case where myosin was absent (Fig. 6.2), this result means that the driving force of the interfacial deformation was exerted by myosin molecules; the actin polymerization and depolymerization were not significant in the present deformation. Figure 6.4 shows typical time evolution of the transmitted light images of a droplet interface. It should be noted that the deformation in the images visualized by the transmitted light means the deformation emerged not only on the actomyosin cortex-like structure but also on the lipid monolayer at the interface, because the oil/water interface appears with the highest contrast in the transmitted light images. By varying the lipid fraction of positively-charged DOTAP and electrically-neutral phospholipid DOPC, we also confirmed that the pure DOTAP monolayer resulted in the highest percentage of the deformed droplets (Fig. 6.5). Therefore, we set the condition as 3 mg/mL for actin, 6 mg/mL for myosin, and the pure DOTAP lipid monolayer in the following observations.

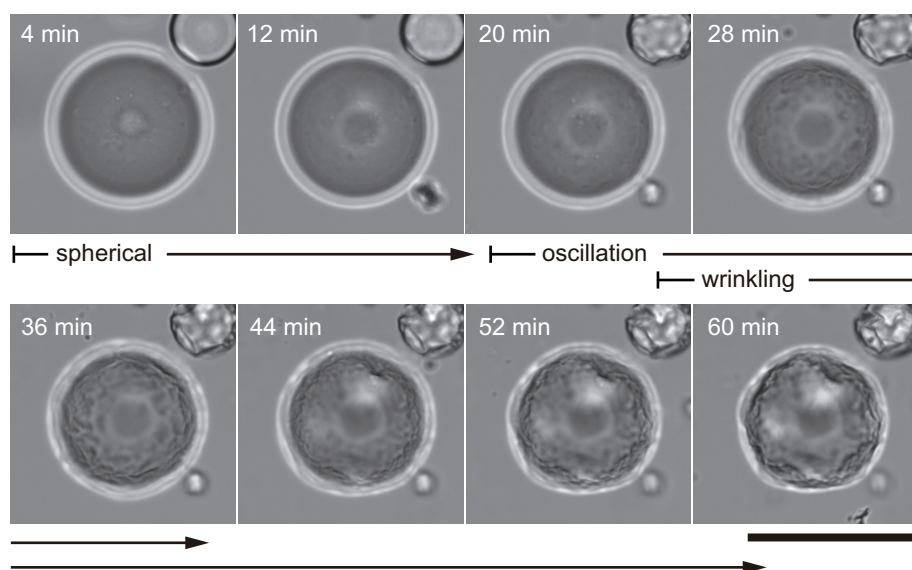


Figure 6.4: Dynamic deformation of the lipid interface owing to the contraction of the confined actomyosin fraction. The interface began to oscillate at around 30 min. After the oscillation started, the wrinkle grew on the interface. Scale bar is $50 \mu\text{m}$.

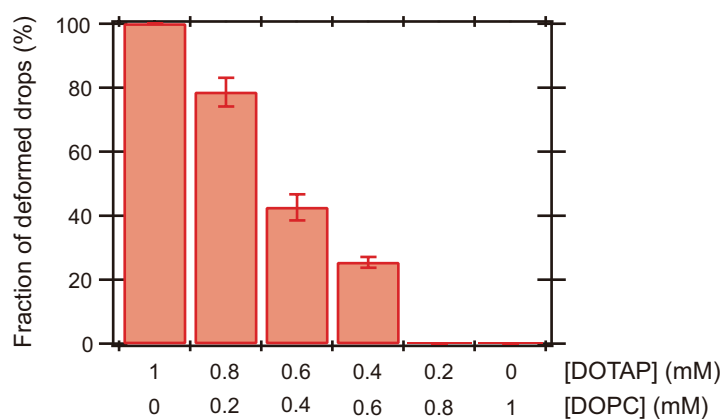


Figure 6.5: Fraction of deformed droplets at the lipid concentrations DOTAP : DOPC = 1 mM : 0 mM, 0.8 mM : 0.2 mM, 0.6 mM : 0.4 mM, 0.4 mM : 0.6 mM, 0.2 mM : 0.8 mM and 0 mM : 1 mM. The total lipid concentration was fixed as 1 mM, Decrease in DOTAP concentration resulted in decrease in the deformation fraction. Error bar represents standard error of the mean calculated from 5 experiments ($n = 5$).

6.3.2 Dynamic interfacial deformation

Next, we investigated the dynamical properties of the obtained interfacial deformation in detail. For a typical case shown in Fig. 6.4, in the initial stage, from the preparation to tens of minutes, the droplet remained spherical due to interfacial tension, as is the case with the behavior of general water droplets. Subsequently, the droplet interface exhibited two modes of characteristic deformation. In mode (i), after approximately 20 min from the preparation, several regions of the interface spontaneously started to deform: the interface repeatedly dented with a characteristic size of approximately $10\ \mu\text{m}$ and restored the original spherical shape. This oscillatory deformation continued for tens of minutes. In mode (ii), after 40 min from the preparation, wrinkles developed on the interface. Although the two deformation modes of (i) the oscillatory behavior and (ii) the wrinkle development tended to occur in this order, the both cases in which the mode (i) and the mode (ii) occurred simultaneously and non-simultaneously were observed in the same sample solution (Figure 6.6), strongly indicating that these phenomena were independent of each other. Hence, the distinct mechanisms that originate from a contractile property of actomyosin should underlie the two different deformation modes. Here, we focus on the dynamic and repetitive interfacial deformation observed as the interfacial oscillation mode (i). To reveal the mechanism that underlies the interfacial oscillation, we confirmed the actin distribution within a droplet using confocal fluorescence microscopy. During the oscillatory deformation, the confocal fluorescence images revealed that initially homogeneous actin filaments within the droplet spontaneously converged into the observable bundles, which further assembled into a three-dimensional aster-like structure in a hierarchical manner (Figs. 6.7(a) and 6.7(b)).

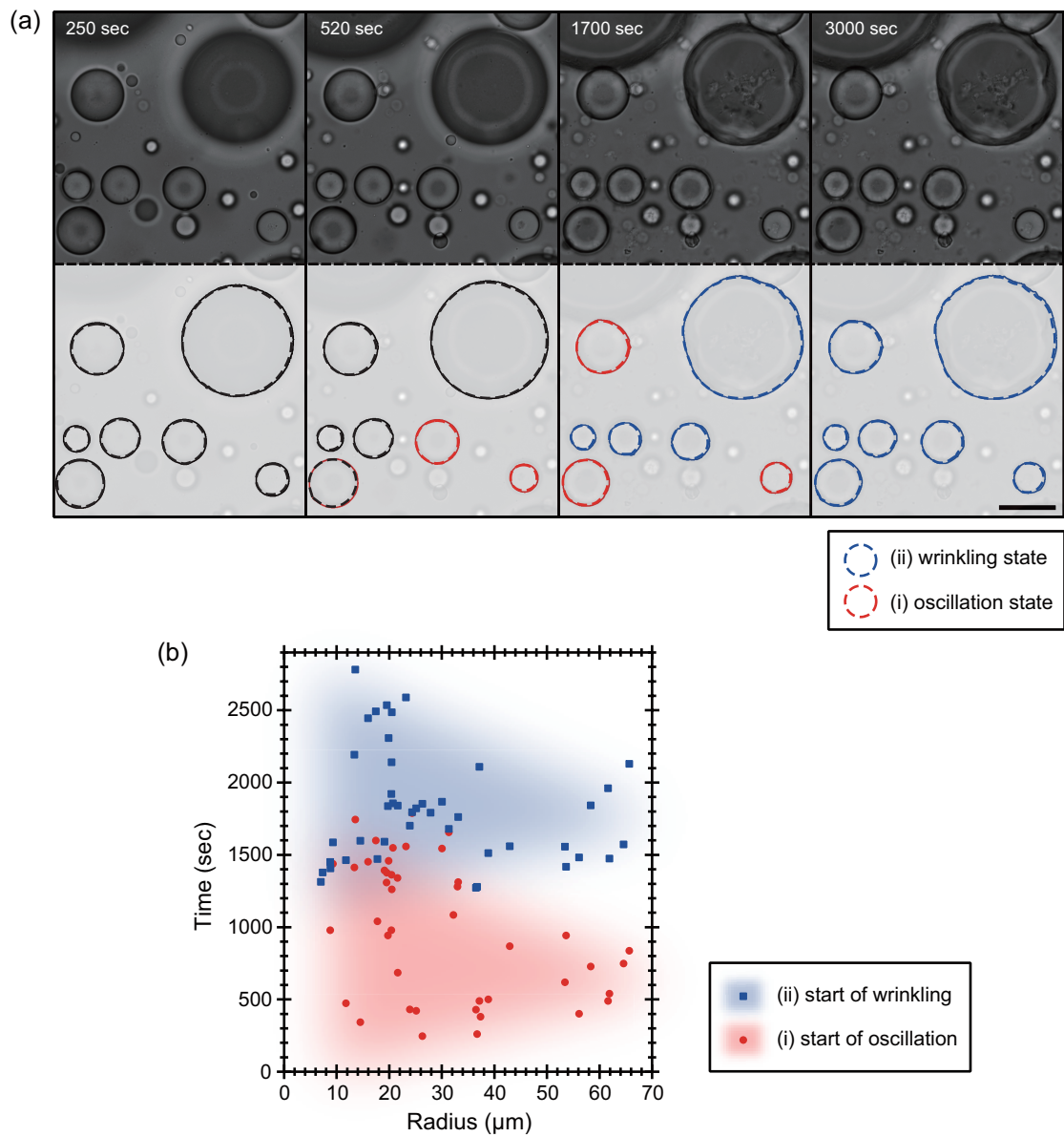


Figure 6.6: (a) Wide view of the transmitted light observation. All the droplets deformed under the appropriate condition: $[\text{actin}] = 3 \text{ mg/mL}$, $[\text{myosin}] = 6 \text{ mg/mL}$, and 1 mM pure DOTAP monolayer. Scale bar is $50 \mu\text{m}$. (b) Beginning times of the two deformation modes (i) oscillation and (ii) wrinkling for various sized droplets.

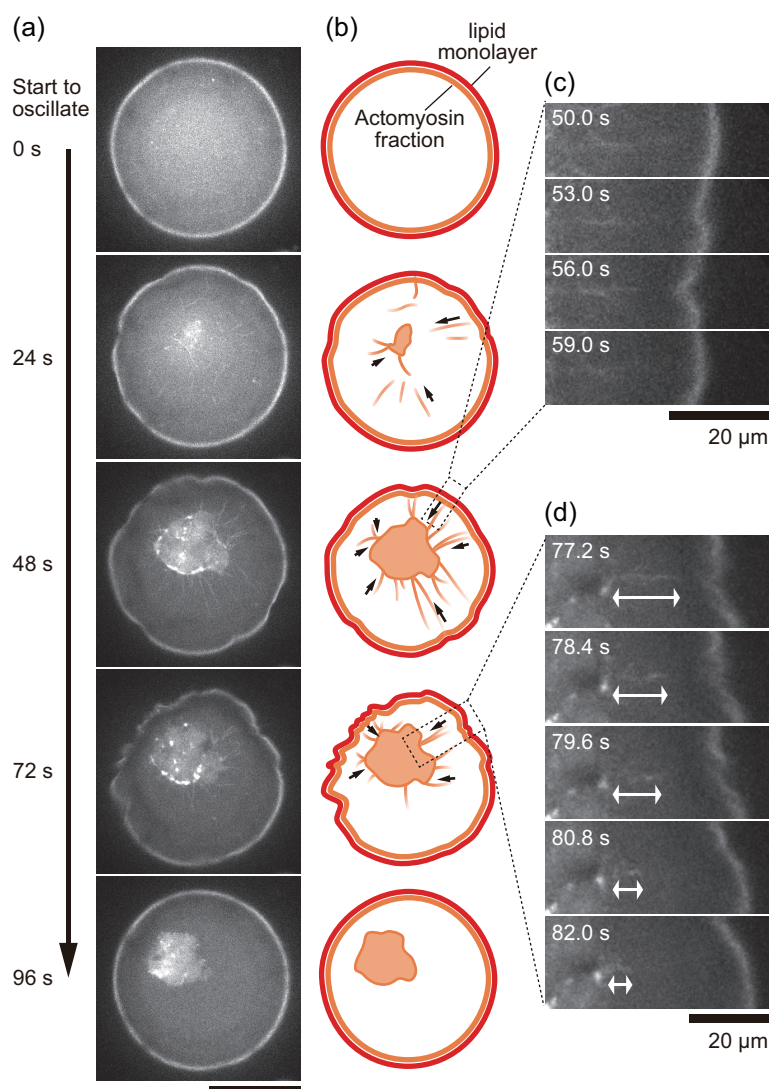


Figure 6.7: Actin distribution during the non-periodic oscillatory deformation. (a) Confocal fluorescence images of the interfacial oscillatory deformation. Actin filaments (fluorescently-labeled) spontaneously form an aster-like structure and pull the lipid interface. Scale bar is $50\ \mu\text{m}$. (b) Schematic illustrations corresponding to the confocal images shown in (a). Red and orange colors denote the lipid interface and actomyosin fraction (fluorescently-labeled in (a)), respectively. The arrows indicate the inward direction of bundle motion. (c) Magnified images of the region enclosed with the connected dashed line in which an actin bundle pulls and distorts the interface. The rectangular images were rotated to put horizontally. Scale bar is $20\ \mu\text{m}$. (d) Magnified images of a region in which the core pulls an actin bundle toward the center of the droplet, leading to the formation of the aster-like structure. The white arrow indicates the length of the actin bundle in the aqueous bulk. Scale bar is $20\ \mu\text{m}$.

Based on this microscopic observation, the actin bundles between the interface and the central core were found to cause interfacial deformation by pulling the interface toward the core (Figs. 6.7(c) and 6.7(d)). The convergence of the actomyosin bundles connected to the significantly deformed part of the interface could be visualized by chemical fixation as shown in Fig. 6.8. The results suggest that the mechanical interconnection between the aster

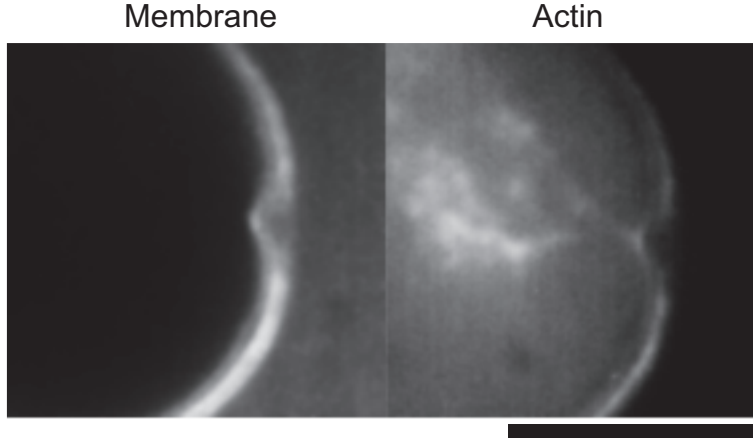


Figure 6.8: Connective behavior between the actomyosin bundles and the cortex underneath the surface of the droplet. The droplets were chemically fixed at the time region of the oscillation and then observed by confocal microscopy. The actomyosin bundles were contacted onto the actomyosin cortex at the deformed part of the droplet. Scale bar is $10 \mu\text{m}$.

structure and the soft interface was mediated by actomyosin network, and the contractile force generated by the mediated actomyosin was converged and transmitted to the lipid interface through the actomyosin bundle as an inward force. Although the formation of an aster-like structure of actomyosin has been previously reported [134, 135], the oscillatory deformation of the interface associated with this active behavior accompanied with the structure development is, to the best of our knowledge, reported for the first time. After the oscillations ceased together with the depletion of the actomyosin bundles bridging the aster core and the interface, the tangential tension of the lipid interface leads to regain its original spherical shape. Thereafter, (ii) wrinkle development started on the lipid interface, where the remaining actomyosin fraction exhibited a cortical shell (Figure 6.7(a), the last image, see also Chapter 7 for detail).

6.3.3 Symmetry breaking of the interfacial fluctuation

It should be noted that the present spherically closed interface provides spontaneous symmetry breaking of the activity of the interface deformation. In the two dimensionally projected polar coordinate (r, θ) exemplified in Fig. 6.9(a), the spatiotemporal map of the fluctuation amplitude became asymmetric, which was accompanied by the displacement of the aster core toward $\theta \simeq 5\pi/4$ in angular position, whereas in the other angles the fluctuation amplitude remained much smaller (Fig. 6.9(b)). Further the distance between the interface and the aster core L became close concurrently with and/or subsequently to the displacement

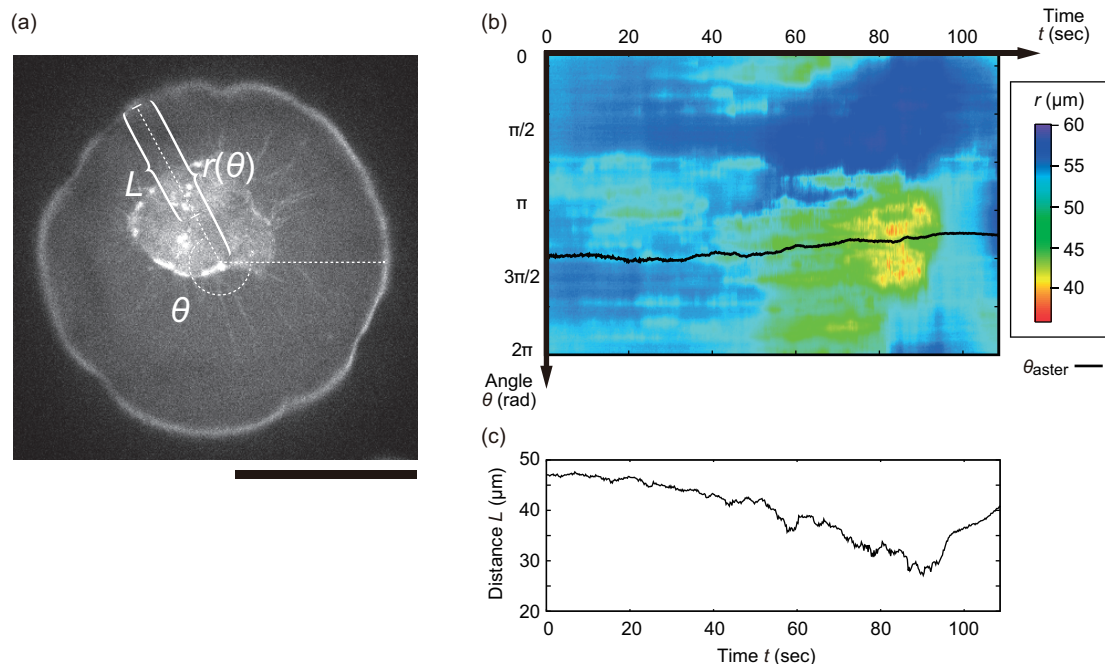


Figure 6.9: (a) Geometrical configuration of the position of the interface and the aster core from the projected droplet center of mass in polar coordinate. Scale bar is $50 \mu\text{m}$. (b) Color map of the spatiotemporal radial position of the interface $r(\theta, t)$. Black line represents the angular position of the aster core θ_{aster} . (c) Corresponding distance L between the radial position of interface $r(\theta_{\text{aster}}, t)$ and the center of core as a function of t .

of the aster (Fig. 6.9(c)). According to the decrease in the distance from the initial state $L(t = 0 \text{ s}) \sim 47 \mu\text{m} \sim r(t = 0 \text{ s})$ to $L(t = 90 \text{ s}) \sim 27 \mu\text{m}$, the interfacial agitation in the vicinity of the aster core increased as shown in Fig. 6.9(b). When the aster core reeled in the bundles ($t > 95 \text{ s}$) after detaching the actomyosin bundles from the interface, the interfacial fluctuation ceased and the interface was restored to the initial spherical shape. Therefore, the experiments suggest that the shorter L results in the stronger attraction with larger fluctuation amplitude. Since the distance L between the core and the interface is also defined by the size of the droplet, the deformation behaviors as a function of the size were also analyzed. First, we confirmed the linear relationship between the normalized intensity of brightness I and the vertical displacement normalized by the droplet radius z/R as shown in Fig. 6.10(a) and 6.10(b). Figure 6.10(c) shows the standard deviation (S.D.) of the normalized oscillatory intensity, which represents the “amplitude” of the oscillation because of the linear relationship between the intensity I and the normalized deviation z/R , as a function of droplet radius R . Here, the normalized deformation amplitude is independent of the droplet radius R , namely, the absolute amplitude is roughly proportional to the radius R , which is consistent with the lower Laplace pressure in larger droplets. Based on the calibration in Fig. 6.10(b), the mean normalized amplitude $\simeq 0.05$ (a.u.) corresponds to the absolute amplitude $\simeq 0.0625R \mu\text{m}$, which agrees well with that seen in Fig. 6.7 ($\sim 5 \mu\text{m}$ amplitude and $50 \mu\text{m}$ radius).

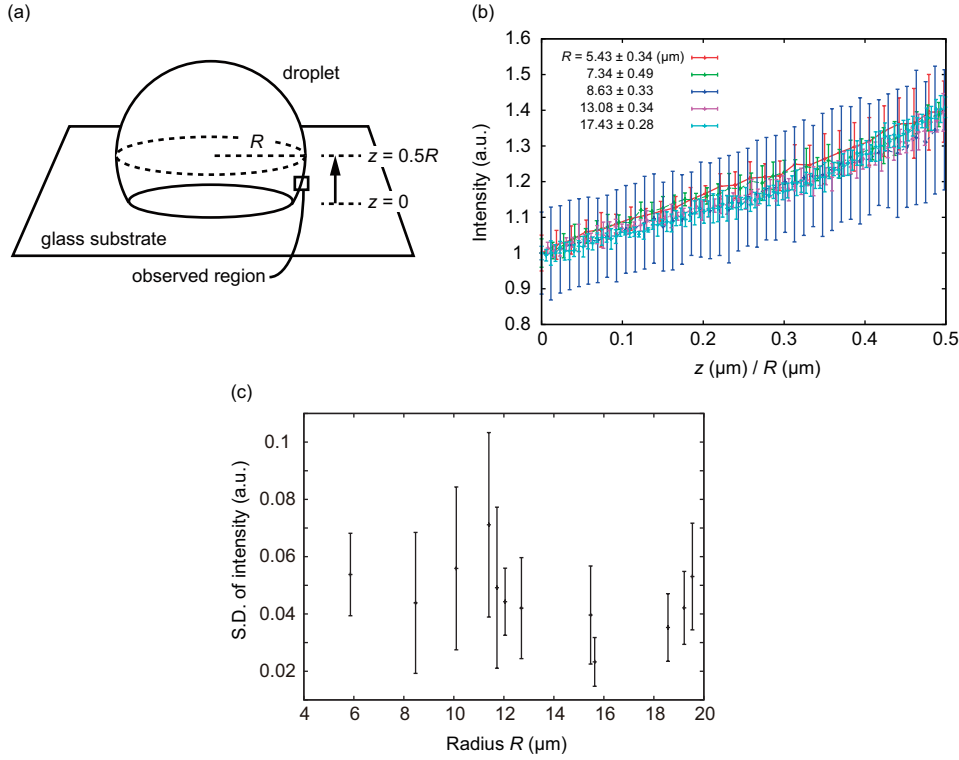


Figure 6.10: (a) Schematic illustration of the calibration measurement for the intensity-deviation relationship. (b) Calibration of the relationship between the normalized intensity of brightness I and the vertical displacement z normalized by each droplet radius R . The range $z/R = 0-0.5$ corresponds to the observed lower hemisphere. The values and error bars represent mean \pm standard deviation (S.D.) coincide with the measurement of three droplets for each radius. The linear intensity-displacement relationship is universal for various droplet sizes. The slope of the master curve is 0.8. (c) S.D. of the normalized oscillatory intensity as a function of droplet radius R .

6.3.4 Molecular contributions to the force generation

It is well known that the contractile force [125, 126] and aster structural formation [134, 135] are induced by motor proteins in the presence of the crosslinkers of actin network. Although our experimental system was mostly composed of actomyosin (Fig. 6.1(b), over 85%), a certain amount of other proteins including actin crosslinker proteins is contained. In addition, highly concentrated myosin bipolar thick filament [145, 146] or myosin strongly bound to actin in ATP depleted condition, *i.e.*, rigor state myosin [126, 135, 147, 148], can also play as effective crosslinkers to generate contractile force in the actin network. Since the myosin concentration in the present study, 6 mg/mL, is much higher than the critical assembling concentration, $\sim 0.5 \mu\text{M}$ (*e.g.*, 0.11 mg/mL of skeletal muscle myosin), myosin thick filaments emerge in the present condition, which were previously confirmed by electron micrograph [140]. To make clear the contribution of ATP depletion in the present system, we checked the behavior in the presence of ATP regeneration system (0 mM, 10 mM, and 30 mM in phosphocreatine concentration) (Fig. 6.11).

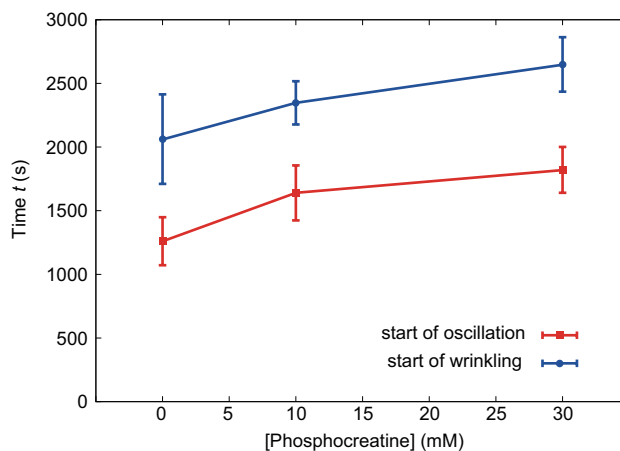


Figure 6.11: Phosphocreatine-concentration dependence of the onset time of the deformation. Squares (red): the onset time of the non-periodic oscillatory deformation; circles (blue): the onset time of the wrinkle development. Error bars represent the standard error of the mean ($n = 5$ for each phosphocreatine concentration)

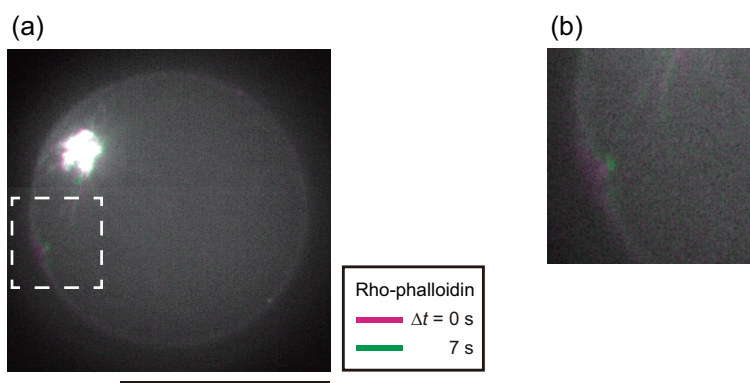


Figure 6.12: Confocal fluorescence image of the oscillatory deformation in the presence of 30 mM phosphocreatine as ATP regenerating system. (a) Overlay of two images taken after $\Delta t = 7$ s. Magenta: $\Delta t = 0$ s; Green: $\Delta t = 7$ s. Two images are processed by rolling average method over ± 3 s, corresponding to the average over 7 images. Scale bar is $50 \mu\text{m}$. (b) Magnified image of a region in which the interfacial deformation is induced by the pulling force by actomyosin bundle, shown in the white dashed box in (a). In the presence of ATP regenerating system, the interfacial deformation is caused by the same mechanism, aster-like structure formation of actomyosin.

Consequently, we confirmed that the time point when the oscillatory deformation starts was clearly delayed according to higher phosphocreatine concentration. In this concentration region, the same mechanism of the oscillatory deformation, *i.e.*, the aster formation inside the droplet, was observed (Fig. 6.12). We also confirmed that the second deformation mode, wrinkle development, was also delayed according to the higher phosphocreatine concentration. The time delay of the oscillatory deformation means that the force generation is correlated to the gradual increase of the amount of rigor state myosin, which possibly acts as one of effective crosslinkers.

6.4 Discussion

The time-evolution shown in Fig. 6.7, again, strongly suggests that (i) the oscillation accompanied by the formation of the aster-like structure occurred independently of (ii) the wrinkling deformation, even though the driving force behind both modes was in common, *i.e.*, actomyosin contraction. The independence of the two modes observed here was also confirmed by checking the time for each mode to start for a number of droplets (Figure 6.6). The result also indicates that start time in each mode and droplet was dispersed especially in smaller droplets. This behavior would correspond to the dispersion of the initial condition, *i.e.*, the encapsulation concentration of the huge macromolecules inside the droplet would be more dispersed in small droplets, whereas that inside the larger droplets converges due to the law of large numbers.

The resultant interfacial deformation indicates that electrostatic attraction is sufficient to maintain the connection between the cortex and the lipid interface, leading to interfacial deformation; furthermore, the result suggests that the force generation and cross-linking between the bundles in the actomyosin core of the aster-like structure are more prominent than those underneath the lipid interface, probably due to the dimensionality of the actomyosin structure, *i.e.*, the aster-like aggregation in the aqueous phase is three-dimensional structure with more cross-links than the cortex-like two-dimensional structure underlying the interface. The more cross-links are formed in the case of the shorter distance between the aster core and interface, which could result in the asymmetric force generation. Regarding the typical energy cost to cause the interfacial deformation, it is remarkable that the energy cost of the deformation in the present interface is 10^3 – 10^4 times higher than that of an elastic lipid bilayer membrane in the case of cell-sized systems [149–151]. By estimating the lower limit of the pulling force in a single indentation that typically exhibits $10\ \mu\text{m}$ in depth from the initial spherical shape, a normal force at least of the order of 10–100 nN is required against the interfacial tension of the order of 1–10 mN/m [150, 151]. Although not only surface tension but also the volume constraint and elasticity of the cortex structure could contribute to the restoring force, the above simple estimation indicates that at least tens or hundreds of thousands of myosin motors are involved in the generation of force in an actomyosin bundle [152]. In the present closed system, this strong force agitates the higher order structure, the aster core inside the droplet. Since the aster structure was attracted to the various directions by the contractile forces of the bundles depending on the distance from the interface, the center position should be unstable fixed point leading to the spontaneous symmetry breaking of the shape and the activity of the interfacial agitation. In other words, the contraction of the actomyosin bundle between the aster core and the corresponding interface resulted in three dimensional “ tug of war ” issue, which determines the central position under the pulling forces toward different directions. Once the pulling

force is reduced in one side, the overall force becomes imbalance, leading to further force imbalance.

6.4.1 Non-periodicity

We here characterized (i) the oscillatory deformation of the interface by analyzing the intensity profiles of the transmitted light images. The intensity of transmitted light reflects the degree of the shape change of the curved surface, whereas confocal fluorescence images (as in Fig. 6.7) are unsuitable for visualization of the present fast dynamics and long-term tracing due to the impact of fluorescence photo-bleaching. Prior to the following analyses, approximately linear relationship between the transmitted light intensity and the interfacial deviation was confirmed (Fig. 6.10(a)). A time-sequential intensity profile along the white line shown in Fig. 6.13(a)(i) is presented as a kymograph (Fig. 6.13(a)(ii)). The rectangular region clipped by a white dotted line indicates the in-focus region in which we analyzed the time course of intensity. The intensity profile at various time points (3 min, 17 min, 31 min, 45min and 59 min after the droplet preparation) clearly shows that the oscillatory deformation occurred for 20 min at around 30 min in this droplet (Fig. 6.13(b)). We calculated the autocorrelations of the temporal oscillatory deformation for 360 degrees by rotating the radial white line shown in Fig. 6.13(a) (i) in increments of 1 degree, and then angularly averaged them. The angularly averaged autocorrelation, which is denoted by $\langle \text{autocorrelation} \rangle$, and its exponential fitting revealed that the relaxation time for one pulse-like oscillation was 7.83 ± 0.03 s (Fig. 6.13(c)). The excellent fitting with exponential indicates that the oscillatory deformation shown here is non-periodic. Thus, we call the present oscillatory deformation mode as non-periodic oscillation. We also obtained the angularly averaged power spectra at each time point from the preparation of the droplet (Fig. 6.13(d)). To grasp the nature of the non-periodic oscillation, we focus on the spectrum at around 31 min (denoted by a green line), when the oscillatory behavior was observed for this droplet. There, both the signal-to-noise ratio and the power spectral magnitude were a few orders of magnitude greater than those in other time regions. The scaling exponent of the power spectrum plotted versus frequency in this region was -2 around the characteristic frequencies of $\omega = 1$ Hz for a single pulse and $\omega \sim 0.1$ Hz for the characteristic time between pulses. Considering the shift to the gentle slope in the low frequency region, the spectrum can be fitted by the Lorentzian as a function of frequency ω .

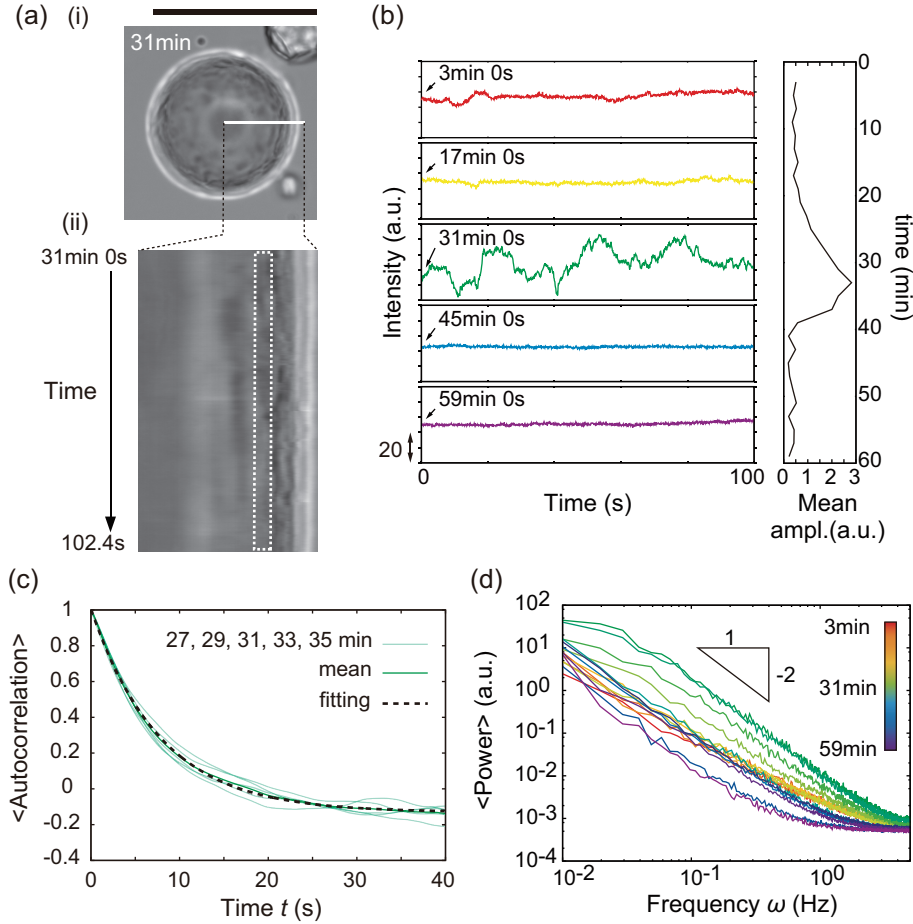


Figure 6.13: Characterization of the time correlation of the dynamic non-periodic oscillation. (a) Example of the time course of the intensity oscillation during the non-periodic oscillatory deformation. (i) Transmitted light images of the droplet at 31 min from the droplet preparation. Scale bar is $50\ \mu\text{m}$. (ii) Spatiotemporal map of a magnified region indicated in (i) by the radial white line. The white broken box in (ii) corresponds to the region in-focus, which were analysed. (b) (left) Time course of the intensity at various time points ranging from 3 min to 59 min. (right) Mean amplitude of the oscillation profiles exemplified in the left graphs. Time-dependent oscillation occurred only around 30 min. (c) Autocorrelation of the oscillatory deformation around 30 min (27, 29, 31, 33, 35 min, and the mean of them). The broken line is the result of exponential fitting of the mean. (d) Temporal variation in power spectra. There is no peak for the broad frequency domain $\omega = 0.01\text{--}5\ \text{s}^{-1}$, indicating the temporal oscillatory deformation is non-periodic.

6.4.2 Non-Gaussianity

To confirm the rarity of the deformation process by the actin bundles, we calculated the probability density distribution of intensity change ΔI versus time lag Δt which is called van Hove self-correlation function (Fig. 6.14). In general, if the deviation is uniformly and

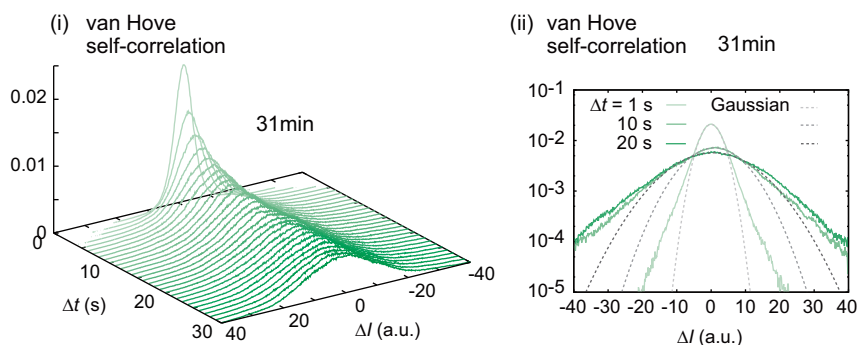


Figure 6.14: van Hove self-correlation function obtained for the oscillatory deformation. (ii) The tails of the distributions are almost linear in single logarithmic plots, *i.e.*, exponential distributions. Gray broken lines are Gaussian distributions corresponding to the green lines with the same brightness. All fittings were conducted around the peaks of the experimental distributions.

thermally activated, *i.e.*, under equilibrium thermal fluctuation, van Hove self-correlation function becomes a Gaussian distribution. However, van Hove self-correlation function shown here is not Gaussian but rather exponential at the tail of the distribution for various lag times Δt , consistent with the rarity of events of extra-large deviations in a Poisson process.

6.4.3 Mechanism of the oscillatory deformation

The above results can be interpreted as follows: The non-periodic oscillatory deformations of the interface are caused by the normal stress exerted by actomyosin bundles, which is a highly random phenomenon identified as a Poisson process dominated by a small number of bundles. The repetitive nature of the deformation is composed of two factors: contraction of the connected actomyosin bundle inward and restoration of the interface outward accompanied by the mechanical detachment of the bundle. Note that the distribution around the mode value is Gaussian, indicating that the generation of the force by the bundles partly detached from the interface, which exhibit small stick-slip type deviations, causes a large number of small random fluctuation of the interface, whereas the complete detachment of the bundle causes a small number of large pulse-like deviations, which yield the exponential decay of the autocorrelation and Lorentzian function of the power spectrum as well as non-Gaussian tail of van Hove self correlation function. A similar distribution for rare events of extra-large deviations has been reported in other complex systems, *e.g.*, anomalously diffusive colloids dispersed in micro-structures such as the actin network, or in jamming states, in which the deviations are controlled by a large number of small thermal deviations and a small number of large non-diffusive jumps due to steric structures [127, 153–155].

In the present study, we have observed for the first time the oscillatory deformation of the interface driven by the connected contractile actomyosin. The non-periodic oscillatory behavior should be realized by the interaction among the force generation of actomyosin, elastic response of the interface, and the intrinsic properties in the system such as the geometric constraint and the bundle detachment. To further understand the physical nature of this interfacial deformation, we developed an equation of motion of the interface based on the experimental results. The exponentially decaying autocorrelation and Lorentzian-type power spectrum, which are the statistical nature of the non-periodic oscillatory deformation of the interface, are generally derived from over-damped Langevin equation of a mass-less area element:

$$\Gamma \frac{dx}{dt} = -kx + \xi(t), \quad (6.1)$$

where the left hand side is damping factor proportional to the interfacial velocity with damping coefficient Γ , the first term in right hand side is restoring force by an effective spring with spring constant k , and $\xi(t)$ is external random force, which satisfies the properties of white noise as $\langle \xi(t) \rangle = 0$ and $\langle \xi(t)\xi(t') \rangle = 2D\delta(t-t')$ (D ; amplitude of the external random force) [156]. x is the deviation length of the area element. The Gaussian peak and the exponential decay in the tale of van Hove self-correlation function (Fig. 6.14) imply that the distribution of $\xi(t)dt$ is composed of not only Gaussian but also Poissonian distribution [157, 158]. The corresponding random force is the linear combination of white Gaussian noise $\xi_G(t)$ (mean; $\langle \xi(t) \rangle = 0$, variance; $\sigma = \text{const.}$) and white Poisson noise $\xi_P(t) \equiv \pm I_P \sum_i \delta(t-t_i)$ (noise intensity; $\pm I_P = \text{const.}$, birth rate; $\lambda = \text{const.}$), which satisfy $\xi(t) = \xi_G(t) + \xi_P(t)$ and still keep the property of white noise as $\langle \xi(t) \rangle = 0$ and $\langle \xi(t)\xi(t') \rangle = 2D\delta(t-t')$, where $2D = \sigma + \lambda I_P^2 = \text{const.}$. In the present non-periodic oscillation, these restoring and damping forces are balanced with the driving force from active actomyosin contraction, which is here assumed to be a white noise term as random force. By solving the above differential equation, we reproduce the exponential decay of the spatial autocorrelation equation

$$\langle x(t)x(t') \rangle = \frac{D}{\Gamma k} e^{-\frac{k}{\Gamma}|t-t'|}. \quad (6.2)$$

By fitting the experimentally obtained autocorrelation function with this theoretical autocorrelation equation, we obtain the ratio between the damping coefficient and the spring constant as $\Gamma/k \sim 10\text{s}$. From a physical viewpoint, the damping term would correspond to viscous friction against the active interfacial velocity. On the other hand, the linear spring term would correspond to the linear-responsive confinement for sufficiently small elastic deviation of an area element from adjacent interfaces. Although the phenomenological viscous-like damping should be observed also in the previously reported bulk systems [126–128], it is remarkable that the emergence of the elastic restoring force is an essential nature of the closed spherical (curved) interface, resulting in a spatial constraint for the deviation (see next chapter for detail).

On the other hand, if we assume that the viscous damping and restoring force are originated from the viscosity of inner and/or outer solution and interfacial tension of the lipid monolayer at the interface, respectively, each parameter can be estimated as $\Gamma \sim \eta l \sim 10^{-8} \text{ Nm}^{-1}\text{s}$ and $k \sim \sigma \sim 10^{-3} \text{ Nm}^{-1}$. Here, $\eta \sim \eta_{\text{oil}} \sim \eta_{\text{water}} \sim 10^{-3} \text{ Pa} \cdot \text{s}$, $l \sim 10^{-5} \text{ m}$, and $\sigma \sim 10^{-3} \text{ Nm}^{-1}$ are viscosity of solution, deviation length, and the interfacial tension of a lipid monolayer at an oil/water interface, respectively. This estimation yields $\Gamma/k \sim 10^{-5} \text{ s}$, which is much smaller time scale compared to the experimentally observed one, $\sim 10\text{s}$. The discrepancy between this estimation and the experiment implies that there is another

inherent time scale in the system. We propose that this time scale is attributed to the correlation time of active force generation [159–161]. In addition to the white noise $\xi(t)$, here we introduce non-Gaussian colored noise $\xi_A(t)$, where the statistical properties are given by mean; $\langle \xi_A(t) \rangle = 0$ and correlation; $\langle \xi_A(t)\xi_A(t') \rangle = f(q)e^{-\frac{|t-t'|}{\tau}}$. $f(q)$ and τ are any function of spatial frequency q and the correlation time of active force generation by myosin motors, respectively. Since we again consider a Poisson event for the birth of the active colored noise, amplitude of the correlation function $f(q)$ includes the birth rate λ_A of this noise. We also assume that there is no correlation between the white noise and the colored active noise: $\langle \xi(t)\xi_A(t') \rangle = 0$. The equation of motion is then described by

$$\Gamma \frac{dx}{dt} = -kx + \xi(t) + \xi_A(t). \quad (6.3)$$

From this equation, the autocorrelation of the deviation x is obtained as

$$\langle x(t)x(t') \rangle = \left[\frac{D}{\Gamma k} - \frac{\Gamma f(q)}{k\tau \left\{ k^2 - \left(\frac{\Gamma}{\tau} \right)^2 \right\}} \right] e^{-\frac{k}{\Gamma}|t-t'|} + \frac{f(q)}{k^2 - \left(\frac{\Gamma}{\tau} \right)^2} e^{-\frac{|t-t'|}{\tau}}. \quad (6.4)$$

This form contains two different time scales, Γ/k and τ . Given the above order estimation of $\Gamma/k \sim 10^{-5}$ s, the experimentally obtained time scale of 10 s would be coincide with τ , the time scale of successive force generation of an actomyosin bundle. In fact, such a successive pulling behavior was observed in our experiment, *e.g.*, see Fig. 6.7(c).

In recent years, the white noise $\xi(t)$ and colored noise $\xi_A(t)$ have also been considered in microrheology in living cells or extracted active gels [127, 128]. Theoretical description of the motion of a probe particle embedded in cytoplasm or the active gels observed in these experiments have been increasingly developed [160, 161]. In these experimental systems, micro-beads in actomyosin network are simultaneously subjected to thermal agitation, spatial confinement by highly-crowded environment, and active forces generated from actomyosin. The overall deviation distribution with respect to a certain time lag have been found to be not Gaussian but exponential at the tail, which agrees with the present van Hove self correlation function. Since our interfacial system does not thermally fluctuate and the radial force is visibly generated by an actomyosin bundle, the present interfacial motion is purely driven by the active force by actomyosin, and there is no other contribution to the fluctuation. This fact and the above order estimation would provide a strong evidence that the active force has the correlation time of the order of 10 s. Actually, the time scale of the emergence of the non-Gaussian behavior in these bulk systems is also of the order of 10 s, which were variously interpreted as a result of jump motion of a particle due to the detachment of myosin [127] (indicating Poissonian shot noise), directed motion [128] (indicating correlated colored noise), etc. Our experimental result and estimation suggest that the colored noise rather than Poisson shot noise is feasible for the reason for the emergence of non-Gaussian nature in van Hove self correlation function.

According to the discussion in this subsection, we concluded that the present non-periodic but oscillatory deformation of the interface is realized by the combination of the closed spherical geometry and the Poisson events of the stochastic contraction and detachments of actomyosin bundles, which would generate pulse-like forces and correlated forces acting on the deformable interface.

6.5 Conclusion

We have reported the dynamic and continual interfacial deformation caused by actomyosin contractility. The initially homogeneous actomyosin solution encapsulated in a cell-sized water-in-oil droplet spontaneously causes the two distinctive deformation of the droplet interface, *i.e.*, non-periodic oscillation and interfacial wrinkling. These phenomena are strongly coupled with structural formation of the actomyosin, aster-like and cortex-like structures, respectively, reflecting the active self-assembly under cell-sized confinement. In our experimental system, it is remarkable that the non-periodic oscillation of the interface is realized by the restoring force due to the closed confinement, stochastic detachments of the actomyosin bundles, as well as the percolation of the stochastic contractile force, *i.e.*, the bridge formation, across the lipid interface and the central actomyosin structure as a Poisson process. As a future work, the elucidation of the detailed molecular mechanisms of the force generation, *e.g.*, crosslinking, actin binding proteins, motor duty ratio, etc. in the present system would be important. Particularly, how much amount of each candidate of crosslinkers, such as myosin bipolar thick filaments, rigor state myosin, and actin crosslinker proteins, contributes to the actual level of crosslinking would be essential information. It should be noted that the present system contained up to 15% unknown proteins, which probably included unspecified actin crosslinker proteins. To determine the amount of the existing actin crosslinker proteins in the present system should lead to better understanding of microscopic contributions to the macroscopic/mesoscopic structure formation and interfacial deformation caused by the emergent contractile force. The resultant dynamic deformation of the interface provides the experimental evidence that both the magnitude of force generation and the structural formation of the components involved in the force generation are crucially important to determine what type of spatiotemporal dynamics appears in a deformable system with force generation and force transduction. Our present findings demonstrate that the percolation of the active forces throughout the cell-sized three-dimensional space by the three-dimensional structural formation of actomyosin can drive the stochastic oscillatory deformation of the interface.

Chapter 7

Active deformation caused by actomyosin

In this chapter, we show the investigation on the second deformation mode of the lipid interface connected to actomyosin contraction. Here, we see that the second deformation mode, slow development of curvature-dependent wrinkled structure, is caused by the cortex-like structure of actomyosin underlying the lipid layer. Through a shape analysis of the wrinkling deformation, we find that the dominant contributor to the wrinkled shape changes from bending elasticity to stretching elasticity of the reconstituted cortex upon increasing the droplet curvature radius of the order of the cell size, *i.e.*, tens of micrometers. The observed curvature dependence is explained by the theoretical description of the cortex elasticity and contractility. Our present results provide a fundamental insight into the deformation of a curved membrane induced by the actomyosin cortex.

7.1 Introduction

Many types of eukaryotic cells have a thin shell-like structure, called the cell cortex, that underlies the cell membrane and consists of actin filaments (F-actin) and type II myosin. Whereas the static stiffness of the actomyosin cortex maintains the cellular shape against external stresses, the active contractile forces of the cortex play crucial roles in a variety of biological processes, such as cell motility [162], cell division [163], embryonic development [123], wound healing [164] and cancer metastasis [165]. The actomyosin cortex is interconnected with the plasma membrane by actin-related proteins, such as ezrin-radixin-moesin (ERM) proteins [166]. However, the mechanism of the consequent membrane deformation caused by force transduction between the cell cortex and the cell membrane remains unclear because the membrane-cortex complex contains highly intricate components and connections [167]. To understand the intricate roles of the actomyosin cortex in cellular processes, bottom-up or reconstitution approaches with a small number of essential components have been adopted. For example, actin polymerization and depolymerization with actin-related proteins in purified systems [168], rheological measurements of purified F-actin solution [169], the motor activity of myosin from the perspective of its interaction with actin [170], and single-molecule analysis [152] have been examined thus far. As reconstitutions of biomimetic artificial systems, the surfaces of giant unilamellar vesicles [171–175] or beads [176,177] have been utilized frequently to investigate the physicochemical properties of interfacial deformation or symmetry breaking of the surrounding actin cortices. On the other hand, actomyosin

encapsulated within a cell-sized confinement exhibits distinct structures, such as network, cortex, and aster formations [135, 136, 174, 178, 179]. However, the fundamental issues regarding the actomyosin cortex, *i.e.*, how the mechanical contractile forces exerted by the actomyosin affect the deformable plasma membrane and its shape, remain poorly understood because of the difficulties of *in vitro* reconstruction, such as those posed by the establishment of effective coupling between actomyosin and membranes [135, 136, 179]. Therefore, we sought to develop a model system that can exhibit the primitive aspects of cell membrane deformation due to the contractile force generated by membrane-coupled actomyosin.

7.2 Materials and methods

All the procedures for culturing *Amoeba proteus*, sample preparations, and observation of water-in-oil droplets are according to the previous chapter.

7.3 Results

7.3.1 Wrinkle development

In the present study, we fabricated a spherical (in its initial state) cell-sized deformable interface composed of a lipid monolayer [19, 21, 143] that encapsulates the actomyosin fraction (Fig. 7.1(a)). As shown in Fig. 7.1(b), the actomyosin fraction used here consists of actin and myosin II extracted from *Amoeba proteus* [140]. The deformation stress on the actin network cross-linked by rigor-state myosins [135] or myosin bipolar thick filaments [140] was exerted by the motive force of active myosin motors through the consumption of ATP, as confirmed by the observation that a droplet in the absence of myosin molecules did not exhibit any deformation. To establish nonspecific interconnection between the actomyosin and the interface, we employed electrostatic attraction [180] using a positively charged lipid, DOTAP. In this solution, the positively charged lipid monolayer attracts negatively charged actin filaments, accompanied by myosin thick filaments as an actomyosin complex. In this situation, we confirmed the suitable experimental conditions that actin and myosin form an actomyosin cortex structure underneath the lipid interface and cause interfacial deformation by the actomyosin contraction, as 3 mg/mL actin, 6 mg/mL myosin, and pure DOTAP lipid monolayer, by tuning the actin concentration, myosin concentration, and DOTAP fraction (see the previous chapter for details). If the myosin concentration is higher than 6 mg/mL, *e.g.*, 8 mg/mL, the actomyosin detaches from the lipid layer and condenses to form an aggregate that is independent of the droplet boundary, as reported in previous studies [135, 136]. The interface of the actomyosin droplet was clearly deformed under the above-confirmed appropriate condition (Fig. 7.1(c)), which should be noted that the energy cost to deform the interface of a micrometer-sized water-in-oil droplet is 10^3 – 10^4 times higher than that for an elastic lipid membrane [149–151]. Nevertheless, it is obvious that the droplet oil/water interface deforms because the wrinkles revealed by the contrast in the transmitted light definitely correspond to the deviation of the lipid layer at the oil/water interface from the initial position. This fact was further proved by fluorescence microscopy with different dyes for the lipid interface and actomyosin as shown in Fig. 7.2 (see below for details). For the typical case shown in Fig. 7.1(c), initially spherical droplet exhibited interfacial wrinkling. The interfacial wrinkling was not accompanied by apparent symmetry breaking, *i.e.*, the strong localization of actomyosin distribution, as otherwise observed in

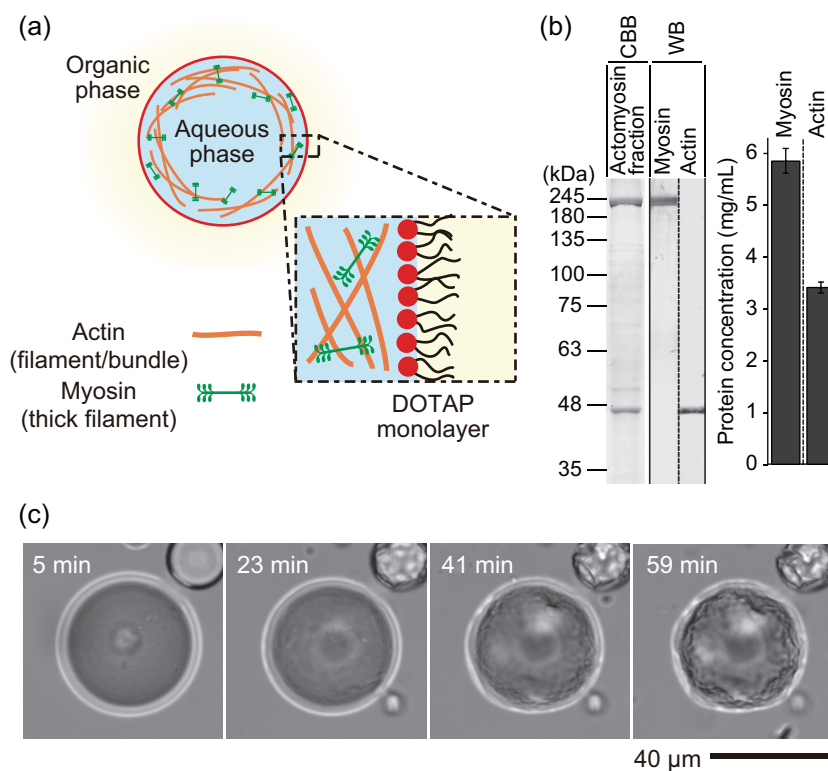


Figure 7.1: (a) Schematic of a cell-sized lipid monolayer encapsulating the actomyosin fraction. (b) Characterization of the actomyosin fraction; error bars represent the standard error of the mean ($n = 5$). (c) Time development of the lipid interface induced by the contraction of the confined actomyosin fraction. The wrinkle grew on the interface. The scale bar corresponds to $40 \mu\text{m}$.

both actin gels around beads [176, 177] and reconstituted [136, 179] or cellular [123, 162] actomyosin, owing to the strong adhesion between the actomyosin and the lipid interface under the present experimental condition.

Figure 7.2(a) shows the time development of wrinkle formation visualized by fluorescently labeled lipid interface and actin with confocal fluorescence microscopy. The actin distribution exhibits that the actomyosin inside the droplet forms a cortex structure underlying the lipid interface. The same fluorescence distributions of the lipid interface and actomyosin cortex structure as shown in the merged images (Fig. 7.2(a), bottom) and the schematics (Fig. 7.2(b)) clearly verify that interfacial wrinkling was directly induced by the underlying actomyosin cortex, which yields lateral contractile force. The comparison between the original spherical interface at the beginning of wrinkle formation $\Delta t = 0\text{s}$ and the wrinkled interface at $\Delta t = 600\text{s}$ revealed apparent dents in the deformed part and slight outward expansion of the entire region at the same time, indicating the volume conservation due to the incompressibility of the inner aqueous solution (Fig. 7.2(c)).

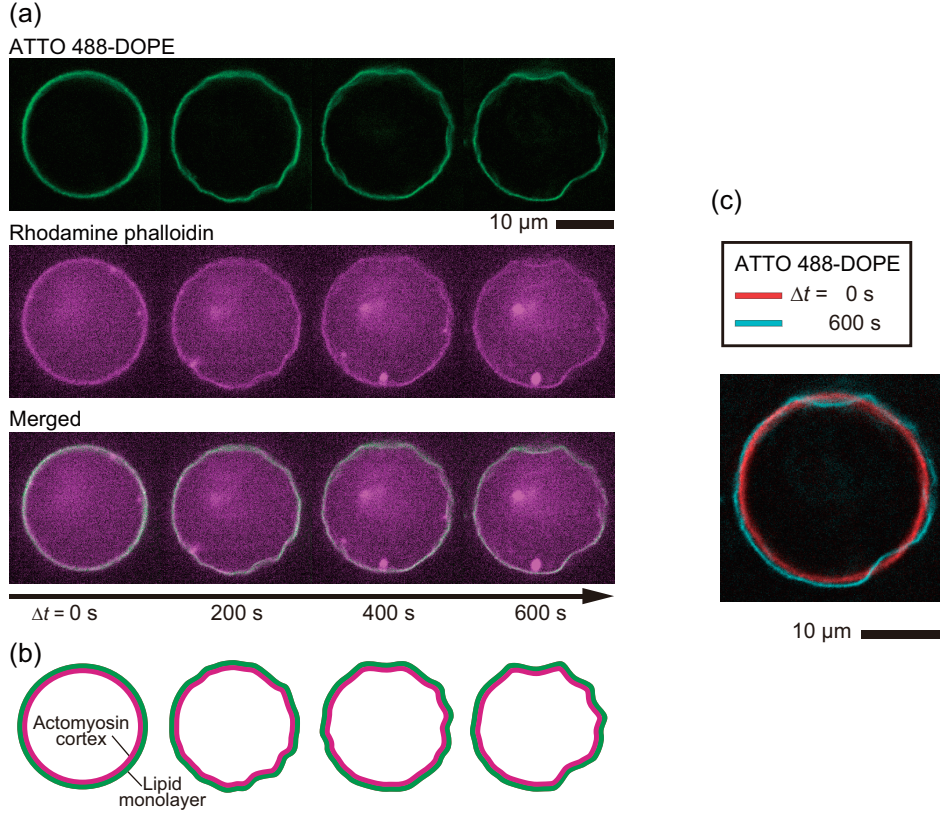


Figure 7.2: (a) Confocal fluorescence images of lipid interface (labeled with ATTO 488-DOPE) and actin filaments (labeled with rhodamine phalloidin) during interfacial wrinkling. $\Delta t = 0$ is defined as the time point at which wrinkling begins. Actin filaments spontaneously form a cortex structure and contract underneath the lipid interface. (b) Schematics corresponding to the confocal images shown in (a). Green and magenta colors denote the lipid interface and actomyosin fraction, respectively. (c) Comparison between the original spherical interface and the wrinkled interface revealed by ATTO 488-DOPE. The original interface ($\Delta t = 0$ s; red) is overlaid on the wrinkled interface ($\Delta t = 600$ s; cyan). The deformation leads to the slight outward expansion of the other part due to the volume conservation of the aqueous phase. All scale bars correspond to 10 μm .

7.3.2 Characterization of actomyosin-induced deformation

To quantify and characterize the intrinsic properties of actomyosin-induced deformation, we analyzed a wrinkled shape as a perturbative shape from the initial spherical shape. Figure 7.3(a) shows a typical example of the confocal fluorescence image of an actomyosin cortex. Based on the droplet equator revealed here, we calculated the radial position x of the deformed cortex, which was taken from the two-dimensional droplet center of mass, as a function of the circumference length L , ranging from 0 to $2\pi R$. The mean radius $R = \langle x \rangle_{\text{angle}}$ was defined as the rotationally averaged radial length. Edge detection was performed by Gaussian fittings of 1024 discrete radial intensity profiles in the vicinity of the cortex, in which the radial positions $x(L)$ were determined as the peak position of each determined

Gaussian function. The red line depicted in Fig. 7.3(a) (right) indicates the detected shape from the original image (left) via this procedure. Figure 7.3(b) shows the graph of radial length x versus circumference length L , *i.e.*, the shape profile of the deformation. From the shape profile, we characterized the actomyosin-induced deformation by calculating the spatial power spectrum and autocorrelation. Gray squares shown in Fig. 7.3(c) are the calculated power spectrum:

$$\left| \frac{2}{N} \sum_{n=0}^{N-1} \{x(n\Delta L) - \langle x(n\Delta L) \rangle\} e^{2\pi i R q n / N} \right|^2, \quad (7.1)$$

where $N = 1024$, q , and $n\Delta L = 2\pi R n / N$, are the sampling number, spatial frequency, and circumference length, respectively. The solid black line is the power-law fitting, in which the exponent shown as the slope in the log-log plot reflects the intrinsic properties of the deformed shape [40, 149]. Figure 7.3(d) shows the autocorrelation $\langle x(L_0)x(L_0 + n\Delta L) \rangle$, where $\langle \rangle$ denotes the average over the arbitrary initial position L_0 and displacement $n\Delta L$. Because of the periodic boundary condition of the shape profile (Fig. 7.3(b)), the autocorrelation becomes negative at a certain displacement $L = n\Delta L$. We can define the correlation length ξ as the smallest length of L that satisfies autocorrelation = 0, so that ξ represents the characteristic width of a concave in the wrinkled shape [181]. For example, in the case of a sine function as a deviation profile from its mean value, the half-length of a convex part, *i.e.*, $\lambda/4$ (λ ; the wavelength of the sine function), appears as ξ in the autocorrelation. This characteristic length of the wrinkles also reflects the underlying mechanism of the actomyosin-induced deformation.

7.3.3 Curvature dependence of the wrinkled shape

We examined the spatial properties of the wrinkle emergence, which we hypothesize was caused by the lateral contractile stress generated by the actomyosin cortex underlying the lipid interface. Note that the distribution of actin observed by fluorescence was laterally homogeneous throughout wrinkle development, except for the effect of the focal depth. Here, we have focused on the curvature dependence of the wrinkling deformation induced by the actomyosin cortex. Following the above-described procedures, the spatial power spectra were calculated for various sizes of droplets. Figure 7.4(a) shows the spatial power spectra of three typical droplets with various radii. Their power-law scaling exponents of spatial frequency q change from -4 for smaller droplets ($R \sim 5 \mu\text{m}$) to -2 for larger droplets ($R > 20 \mu\text{m}$). Figure 7.4(b) exhibits the convergence of the scaling exponents at -2 with the increase in droplet size, ranging from $R = 1.9 \mu\text{m}$ to $53.4 \mu\text{m}$ (Fig. 7.4(b)). These results indicate that the dominant contributor to the deformation exhibits transitional behavior in a size-dependent manner. The crossover size for the appearance of this curvature effect on actomyosin contraction is of the order of $10 \mu\text{m}$. The exponent -2 of a spatial power spectrum is generally observed in the case of interfacial tension-dominated deformation of a planar interface, whereas the exponents -4 and -3 are observed in the bending-energy-dominated deformation of a planar or spherical interface [40, 149]. Therefore, the exponents indicate that the deformed shapes of smaller and larger droplets are predominantly determined by the bending elasticity and contractile interfacial tension of the actomyosin shell, respectively. Here, the width of the concave interfaces should reflect the elastic and contractile properties of the actomyosin interacting with the cell-sized deformable interface. To gain further understanding of the nonspecific interaction between the contractile actomyosin

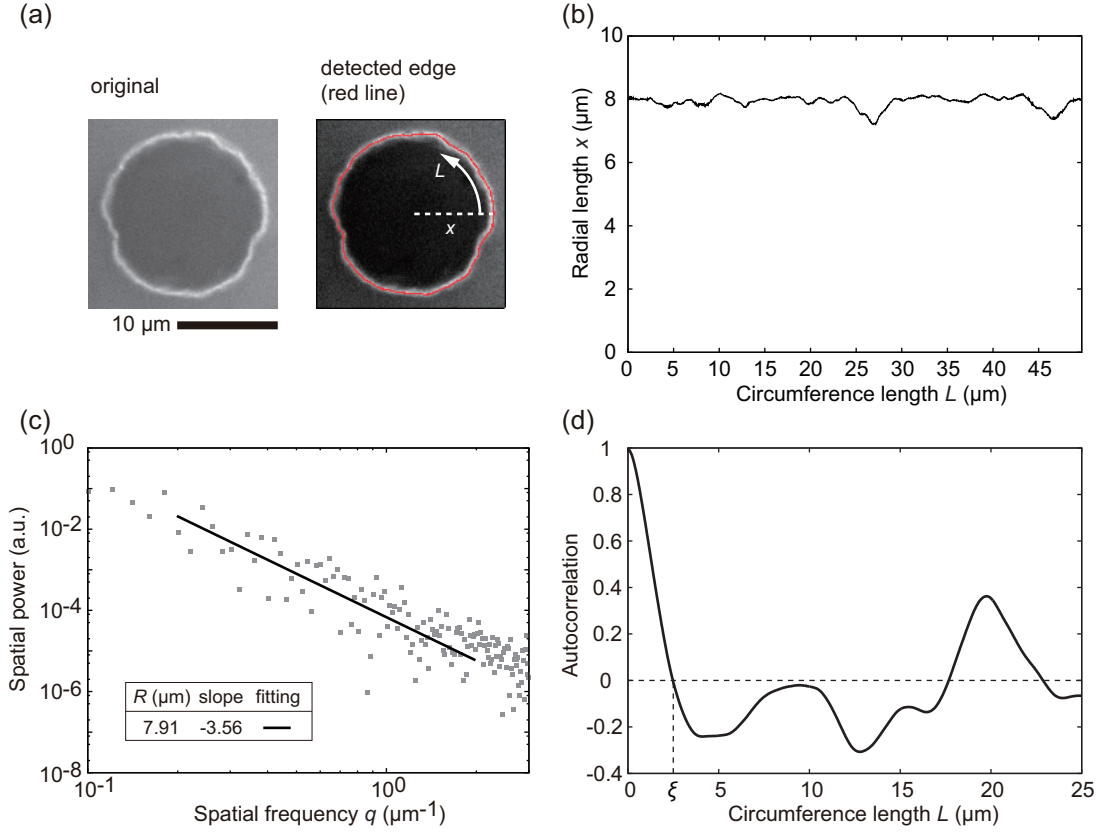


Figure 7.3: Detailed analytical procedure of the spatial power spectrum and autocorrelation for the deformed equator shown by fluorescently labeled actin distribution. (a) Typical example of the original fluorescence image (left) and the detected edge (right; red line). The radial length x is defined as the distance between the two-dimensional center of mass and the detected edge as a function of the circumference length L , ranging from 0 to $2\pi R$ (μm). Scale bar is $10 \mu\text{m}$. (b) Radial length x plotted versus circumference length L . (c) Spatial power spectrum and (d) autocorrelation calculated from the shape profile shown in ((b)). The correlation length ξ is defined as the shortest length at which the autocorrelation equals 0.

cortex and the deformable interface, we developed a theoretical model for the deformation based on the elastic energy of the actomyosin cortex. Comparison between the experimental and the theoretical results should provide insight into the elastic, contractile, and geometric properties of the microscopic actomyosin cortex.

7.4 Discussion

7.4.1 Theoretical model for the onset of wrinkling

Here, we assume that actomyosin forms a homogeneous thin elastic shell-like structure with thickness h and Young's modulus E underneath the surface of the droplet with radius R . We also assume that a part of the spherical interface is slightly distorted from its original spherical shape, with the depth of distortion given as δ (Fig. 7.5(a)). The dent region

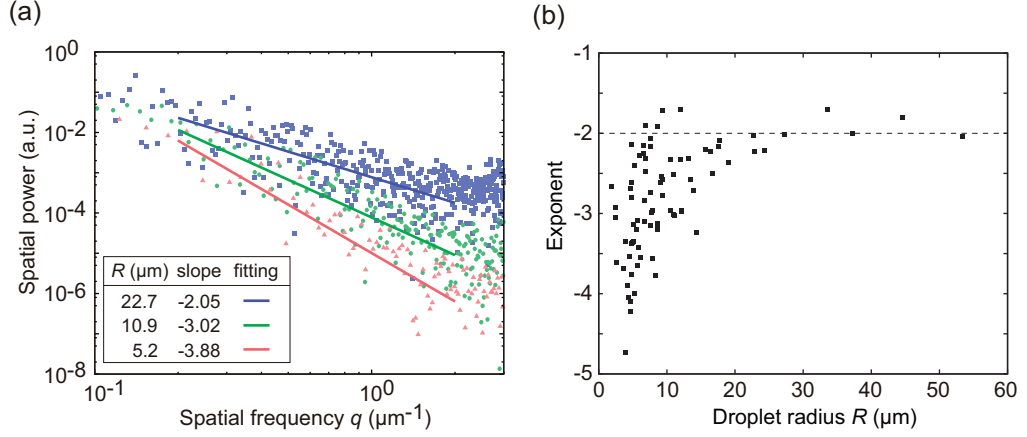


Figure 7.4: (a) Spatial power spectra obtained from the typical equatorial shapes of various-sized droplets represented by pale red, green, and blue (from bottom to top) symbols. The corresponding red, green, and blue (from bottom to top) lines are the power fits of the experimental spectra. (b) Values of the power-law scaling exponents in the power spectra of spatial frequency with respect to the droplet size. Exponents vary from -4 to -2 , in correlation with the droplet size.

stores two types of elastic energy per unit area: bending energy $f_{\text{bend}} \sim Eh^3(\partial^2\delta/\partial x^2)^2 \sim Eh^3\delta^2/r^4$ and stretching energy $f_{\text{stretch}} \sim Ehu_{ab}^2 \sim Eh\delta^2/R^2$, where u_{ab} is a component of the strain tensor of the shell. In the following, we consider the onset of the deformation from the initial spherical shape. The elastic energies over the dent region are obtained as $F_{\text{bend}} \sim r^2 f_{\text{bend}} \sim Eh^3\delta^2/r^2$ and $F_{\text{stretch}} \sim r^2 f_{\text{stretch}} \sim Eh\delta^2 r^2/R^2$. Additionally, we consider the energy cost when the other part stretches outward simultaneously with the partial dent due to the incompressibility of the inner aqueous solution (see Fig. 7.2(c)). When the local interfacial indentation occurs as shown in Fig. 7.5(a), the volume corresponding to the dented part is compensated by the slight outward expansion of the other part of the interfacial shell. Approximating that the stretching of the undeformed part compensates for the dent volume $\Delta V \sim \delta r^2$, the normal stretching length is $\Delta R \sim \delta r^2/R^2$, resulting in the additional energy cost for the distortion: $F_{\text{comp}} \sim Eh(\Delta R/R)^2 \cdot R^2(1 + \sqrt{1 - (r/R)^2}) \sim Eh\delta^2 r^4/R^4$ by neglecting the term of $\mathcal{O}((r/R)^6)$. This energy, up to the order of $(r/R)^4$, is lower compared to F_{stretch} by a factor of r^2/R^2 but should not be neglected because the experimental ratio ξ/R , which corresponds to r/R , shown in Fig. 7.5(b) is not so as low, ranging from 0.15 to 0.83. The interfacial deformation requires a driving force along the normal direction to the interface. In our experimental system, the driving force can be the tangential contraction provided by the contractile actomyosin shell underlying a curved interface [136, 179]. There is a general relationship between the normal stress σ_{rr} and the tangential stress $\sigma_{\perp\perp}$ on a curved surface:

$$\frac{1}{r'^2} \frac{\partial}{\partial r'} (r'^2 \sigma_{rr}) = \frac{2}{r'} \sigma_{\perp\perp}, \quad (7.2)$$

where r' is the radial coordinate [181–183]. By integrating over the shell thickness $r' = R \sim R + h$, the normal stress of the actomyosin shell (per unit area) can be described with the tangential stress as $\sigma_{rr} = 2/R^2 \int_R^{R+h} dr' r' \sigma_{\perp\perp} \sim 2h\sigma_{\perp\perp}/R$, where the same expression is used for the Laplace pressure. Here, the tangential stress $\sigma_{\perp\perp}$ is assumed to be a constant over the shell thickness h . This pressure, which originates from the tangential contraction,

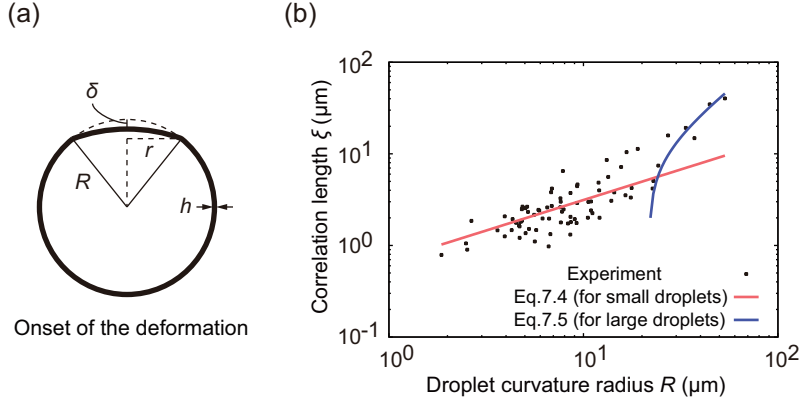


Figure 7.5: (a) Schematic of the situation considered in the model. A portion of the spherical interface is slightly dented, where δ is the depth of the dent, r is the radius of the dent region, R is the initial curvature radius of the droplet, and h is the thickness of the actomyosin shell underlying the droplet interface. (b) Correlation length ξ of the wrinkle shape profile along the circumference, plotted versus the droplet size. Each correlation length is calculated in the final state of wrinkle development. Red and blue lines denote theoretical correlations between the dented radius and the droplet radius described in the text.

causes the interfacial distortion. The work done by the contraction leads to $W_{\text{contraction}} \sim \sigma_{rr} \Delta V \sim h \sigma_{\perp\perp} \delta r^2 / R$.

Thus, we obtain the total energy cost for the deformation:

$$\begin{aligned}
 F_{\text{total}} &= F_{\text{bend}} + F_{\text{stretch}} + F_{\text{comp}} - W_{\text{contraction}} \\
 &\sim \frac{Eh^3 \delta^2}{r^2} + \frac{Eh \delta^2 r^2}{R^2} \left(1 + \frac{r^2}{R^2} \right) - \frac{h \sigma_{\perp\perp} \delta r^2}{R}.
 \end{aligned} \tag{7.3}$$

Let us consider the onset of the deformation. In our experiment, the observed dent radii maintained the same order of magnitude from the onset time to the end of the wrinkling behavior (Fig. 7.2(a)). Therefore, the initial dent radii can be regarded as the experimentally observed dent radii in the wrinkling period. Immediately after the droplet is prepared ($t = 0$ min), the tangential stress is $\sigma_{\perp\perp}(t = 0) = 0$. As time passes, the stress grows inside the shell; consequently, although the energy always permits a small agitation of the interface, of the order of h , the observed macroscopic indentation of the interface begins at a certain time, $t = t_c > 0$. At this time, the signature of F_{total} becomes negative in the range of $0 < r < R$. According to these situations, the critical conditions for the onset of the dent formation require $F_{\text{total}} = 0$ and $\partial F_{\text{total}} / \partial r = 0$. These conditions produce the following correlation between the dent radius and the droplet curvature radius:

$$r = (2h^2)^{\frac{1}{6}} R^{\frac{2}{3}}. \tag{7.4}$$

Here, we verified the corresponding experimental values, *i.e.*, spatial correlation length ξ of the deformed equatorial shapes for various sizes of droplets. ξ was defined as the circumferential length at which the autocorrelation first becomes 0, and thus the length ξ denotes the width of the concave structure along the circumference. Consequently, there is a strong positive correlation between the correlation length ξ and the droplet radius R (Fig. 7.5(b)). The theoretical curvature-radius dependence, indicated by Eq. (7.4), is consistent with the experimental slope in the small-radius region with the fitting parameter

$h = 218$ nm, which is comparable to the observable results (< 500 nm in smaller droplets); furthermore, this value is close to the cortical thickness of living cells [184–186] and previously reconstituted systems [182, 187, 188]. At the same time, the curve, Eq. (7.4), deviates from the experimental data in the larger-radius region of $R > 10$ μm . To elucidate the factors that influence the deviation, we return our discussion to the circumferential power spectra of the deformed shapes for various droplet sizes (Fig. 7.4(b)). The scaling exponents -4 and -3 indicate that the bending elasticity F_{bend} dominates the deformed shape for $R < 10$ μm , whereas the transient distribution and convergence to the exponent -2 indicate that the energies for area stretch (lateral tension), F_{stretch} and F_{comp} , dominate the deformation for 10 $\mu\text{m} < R < 20$ μm and $R > 20$ μm . Because the ratio of the bending term and tension terms is $F_{\text{bend}}/F_{\text{stretch}} = h^2 R^2 / r^4$ or $F_{\text{bend}}/F_{\text{comp}} = h^2 R^4 / r^6$, $F_{\text{bend}} \ll F_{\text{stretch}}$ and $F_{\text{bend}} \ll F_{\text{comp}}$ are realized in the large-radius region ($R > 20$ μm), where r and R are of the same order as in experimental values (Fig. 7.5(a)). Thus, F_{bend} is negligible compared to the tension terms for the large-radius region. Minimizing the energies in the absence of the bending energy, we in turn obtain the following equation for the deformation of larger droplets:

$$r = R^{\frac{3}{2}} \sqrt{\frac{\sigma_{\perp\perp}}{2E\delta} - \frac{1}{2R}}. \quad (7.5)$$

By fitting in the region of $R > 20$ μm (shorter, curved (blue) line in Fig. 7.5(b)), we find $\sigma_{\perp\perp}/2E\delta \sim 0.023$ μm^{-1} . Furthermore, because δ is of the order of 1 μm in our experiment for $R > 20$ μm , the above relation results in the quantification of the ratio between the active force generation $\sigma_{\perp\perp}$ by actomyosin contractility and static elasticity E , *i.e.*, $\sigma_{\perp\perp}/E \sim 0.01$. Note that Eq. (7.5) is only verified under the necessary condition $\sigma_{\perp\perp}/2E\delta - 1/2R > 0$, so that the energy cost, $F_{\text{total}} - F_{\text{bend}}$, has a minimum value. In the case of $\sigma_{\perp\perp}/2E\delta \sim 0.023$ μm^{-1} , this necessary condition results in $R > 20$ μm , which is consistent with the situation of the larger droplets considered here.

Although the wrinkles developed further after the onset of deformation and the dent curvature eventually became negative, the typical pattern of the wrinkled shape was determined in the early stage of the indentation. In the late stage of the deformation, the inner solution of the droplets evaporated or was ejected (data not shown) and the droplets became a bit smaller to release a part of the pressure increase as in Fig. 7.1(c), resulting in the breaking of the volume conservation inside the droplet. In addition to the contractile force of the actomyosin shell, such an increase in the area-to-volume ratio in the late stage could induce complex buckling of the elastic shell as well. While the wrinkled width ξ or r was determined in the early stage considered in the model, to investigate the complex deformation mechanism in the late stage in detail will require future work on this system.

7.4.2 Effect of interfacial tension

In the above discussion, we only have considered the elasticity and contractility of the actomyosin shell. However, the surface tension of the lipid interface may also contribute to the deformation energy cost, because the lipid interface was also deformed to the same shape as the shell, as shown in Fig. 7.2(a). In the same theoretical framework used above, the contribution of the surface tension σ in the dent region can be described as the work done by the Laplace pressure

$$\frac{2\sigma}{R} \Delta V \simeq -\frac{2\pi\sigma\delta r^2}{R}, \quad (7.6)$$

where $\Delta V \simeq \pi\delta r^2$ is the decreased volume by the dent defined as negative. On the other hand, the other region should expand slightly outward due to the incompressibility of the inner aqueous phase, resulting in the radial expansion $\Delta R \sim \frac{\delta r^2}{R^2}$. This contributes to the interfacial energy cost:

$$\sigma\Delta A \simeq \frac{8\pi\sigma\delta r^2}{R}, \quad (7.7)$$

where $\Delta A \simeq 4\pi\{(R + \Delta R)^2 - R^2\}$ is the approximated surface area difference of the droplet before versus after the outward expansion. Therefore, the interfacial energy cost of the deformation becomes $F_{\text{int}} \simeq \frac{8\pi\sigma\delta r^2}{R} - \frac{2\pi\sigma\delta r^2}{R} \sim \frac{\sigma\delta r^2}{R}$. The total energy cost including the elasticity and contractility of the actomyosin shell is then obtained by replacing the lateral stress $\sigma_{\perp\perp}$ by the effective lateral stress $\sigma_{\perp\perp} - \frac{\sigma}{h}$:

$$\begin{aligned} F_{\text{total}} &= F_{\text{bend}} + F_{\text{stretch}} + F_{\text{comp}} - W_{\text{contraction}} + F_{\text{int}} \\ &\sim \frac{Eh^3\delta^2}{r^2} + \frac{Eh\delta^2r^2}{R^2} \left(1 + \frac{r^2}{R^2}\right) - \frac{h\delta r^2}{R} \left(\sigma_{\perp\perp} - \frac{\sigma}{h}\right). \end{aligned} \quad (7.8)$$

The same fitting as that using Eq. 7.3 reads $\frac{\sigma_{\perp\perp} - \frac{\sigma}{h}}{E} \sim 0.01$. Thus, the experimentally observed wrinkling is realized in the case where the contraction exceeds the interfacial tension, namely, $\sigma_{\perp\perp} > \frac{\sigma}{h}$. Our experimental result indicates the lower limit of the ratio between the active contractility $\sigma_{\perp\perp}$ and the static elasticity E as $\frac{\sigma_{\perp\perp}}{E} > 0.01$. Note that $h \sim 200$ nm and $\sigma \sim 10$ mN/m result in $\frac{\sigma}{h} \sim 1$ nN/m².

7.5 Conclusion

Reconstituted actomyosin cortex underlying a deformable lipid interface successfully caused the wrinkling deformation of the interface. This demonstration is, as far as we know, for the first time. Furthermore, the shape analysis and theoretical descriptions revealed the contributions of the bending elasticity, stretching elasticity, and contractility of the reconstituted cortex structure to the interfacial deformation, which anomalously depends on the cell-sized droplet radius, *i.e.*, the interfacial curvature. In other words, we demonstrated the physical basis that even the primitive geometrical coupling between the deformable interface and the confined actomyosin exhibits a rich variety of interfacial deformability. The geometrical origin in our findings should be relevant and taken into consideration for not only purified systems but also living systems such as the contraction of the cell membrane with a contractile cell cortex at the posterior during the amoeboid motion of a cell. Study of the applicability of the present curvature dependence of the contractile cortex in living cells such as *Amoeba proteus* will be one of the most interesting future works. With respect to the objective of reconstituting cellular motility, the spatiotemporal regulation of structural formations should be addressed as the next step in this work by exploring the implementation of the frameworks of actin-related molecules and their signaling networks. Our present findings on how actomyosin behaves within a cell-sized compartment with a deformable interface provides an experimental basis for this purpose, and it takes an important step toward artificial cellular deformation in the step-wise reconstitution of the living state. Together, these investigations may lead to the further clarification of complex biological phenomena involving geometrically coupled actin and myosin functions.

Part IV

Toward reconstitution of an artificial cell

Chapter 8

Dynamics of droplet transfer at an oil/water interface

Because of the strong interfacial tension that appears in the water-in-oil (W/O) droplet system we used in the reconstituted actomyosin droplet in the previous Part, the active deformation was strongly influenced by the geometrical confinement to tend to keep the interfacial area as constant. In this chapter, we introduce the method called droplet transfer method to form much more flexible lipid bilayer vesicles from W/O droplets. Toward the application of the method to fabricate the lipid bilayer vesicles encapsulating actomyosin, we first address the practical difficulty in the method by considering the interesting interfacial dynamics. This interfacial phenomena intrinsic in the method itself is the main subject of this chapter.

Recently, the transfer method has been shown to be useful for preparing cell-sized phospholipid bilayer vesicles, within which desired substances at desired concentrations can be encapsulated, with a desired asymmetric lipid composition. Here, we investigated the transfer process of W/O droplets coated by phospholipid monolayers across an oil/water interface by both experimental observation and theoretical modeling. Real-time experimental observation of the transfer revealed that the transfer process is characterized by three kinetic regimes: a precontact process (approaching regime), an early fast process (entering regime), and a late slow process (relaxation regime). In addition, bigger droplets require much more time to transfer than smaller droplets. We propose a theoretical model to interpret this kinetic process. Our theoretical model reproduces the essential aspects of the transfer kinetics, including its size-dependence.

8.1 Preparation method of cell-sized lipid bilayer vesicles

8.1.1 Conventional preparation method

The synthesis of artificial cells from lipid bilayers (giant unilamellar vesicles; GUVs) has been one of the most attractive targets in the field of soft matter [30, 137, 189–192]. To fabricate physicochemical GUV systems that mimic cell membranes, the natural swelling method [193–196] and electroformation method [197–199] have been widely used [200].

8.1.2 Droplet transfer method

Recently, a method for preparing GUVs from water droplets, called the droplet transfer method, is becoming increasingly adopted [187,200–203]. In this method, GUVs are formed through the transfer of water-in-oil (W/O) droplets coated by lipid monolayers across a lipid monolayer at a planar oil/water interface. The transfer method offers important advantages for the synthesis of GUVs as artificial cell models: 1) it is easy to control the final sizes of GUVs by controlling the sizes of the precursor W/O droplets [204–208], 2) different lipid compositions can be used for the inner and outer leaflets of the lipid bilayers [205,209,210], 3) it is easy to encapsulate an arbitrary solution at a desired concentration [187,191,202,203], and so on. As to the issue of encapsulation, the capability of encapsulating a diversity of solutes and buffers, also physiological ones, is especially of great use since the natural swelling and electroformation methods have suffered from serious limitation for the buffer solution with salt and the formation of complex mixtures. On the other hand, there are still some technical problems with the transfer method; it is empirically known that the transfer method requires too much time to transfer lipid-coated droplets across a planar lipid monolayer without the application of external forces, and it is impractical for the formation of complete GUVs, depending on the experimental conditions such as the lipid compositions, the solution, and the sizes of the droplets. To avoid this problem, a method in which lipid-coated droplets are forced to transfer across the interface through the application of centrifugal force has been commonly used, and has been successful in many practical applications [187,201–203]. However, aspects of this method still need to be improved, such as the stability of the droplets at certain lipid compositions and the uncertain contamination by an oil fraction between the lipid bilayers [201,204,211,212]. For the efficient synthesis of GUVs encapsulating arbitrary biological agents at arbitrary concentrations with biological trans-bilayer asymmetry as artificial cell models, it would be tremendously helpful if we could elucidate the underlying dynamical mechanism of lipid-coated droplet transfer across a lipid monolayer.

In the transfer methods, W/O droplets must transfer across an oil/water interface to form bilayer vesicles. In this case, the fundamental driving force for transfer process is the energetically-favorable adhesion of two lipid monolayers, which is caused by an interfacial free energy difference between two lipid monolayers at oil/water interfaces and the lipid bilayer in the aqueous phase. The adhesion of the two lipid monolayers is the most important factor for the transfer process not only in transfer methods without external forces to push the droplets into the aqueous phase, but also in other types of transfer methods, including centrifuge-dependent methods [187,201–203]. Therefore, studies of the dynamical process of droplet transfer accompanied by adhesion between the monolayers could provide insight into phenomena that commonly underlie all types of transfer methods, which are the best candidates for the bottom-up fabrication of GUVs as a model cell system.

In the present study, we investigated the dynamics of the transfer mechanism in detail by using the spontaneous transfer method, in which droplets transfer across the interface without any external forces [34,135,213]. Since the spontaneous transfer method allows us to continuously observe a droplet throughout the transfer process in a chamber, we can observe the fundamental dynamics of droplets from the beginning of the formation of GUVs by microscopy, which has not been achieved in droplet transfer methods that include centrifugation. In this paper, we report experimental measurements of the kinetic process of the transfer of droplets with various radii and describe the kinetics with a phenomenological model in the context of a reaction-diffusion system. The results of our theoretical model

are qualitatively consistent with the experimental results regarding the dynamics, including the size-dependent transfer behavior of droplets. Furthermore, our model successfully reproduces another size-dependent observation concerning the onset of transfer, as confirmed by a quasi-static experiment.

8.2 Materials and methods

The phospholipid L-alpha-Phosphatidylcholine, dioleoyl (DOPC) was obtained from Wako Pure Chemical Industries, Ltd and Avanti Polar Lipids, Inc. Egg L-alpha-phosphatidylcholine (eggPC) was obtained from Avanti Polar Lipids, Inc. DOPC and eggPC were used without further purification and stored in an organic solvent of chloroform/methanol (2:1, v/v) at -20°C . Mineral oil (density $\sim 0.81\text{ g mL}^{-1}$ with n-alkanes with carbon numbers ranging from C12 to C38, boiling point $> 300^{\circ}\text{C}$) was purchased from Nacalai Tesque, Inc [151]. All aqueous solutions were prepared with Milli-Q distilled water.

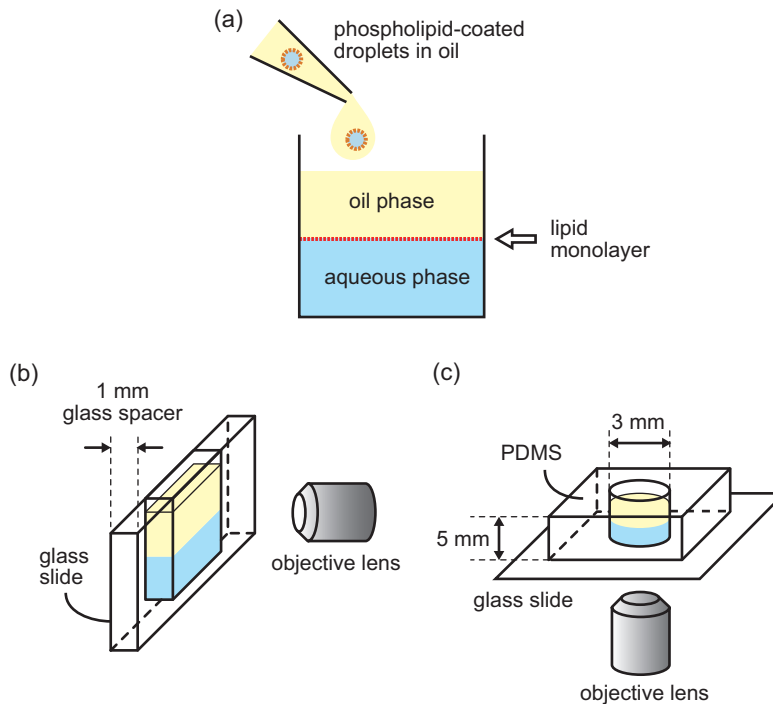


Figure 8.1: Experimental setup for the spontaneous transfer method. (a) Schematic illustration of the transfer method. GUVs are formed from W/O droplets in the oil phase across the planar lipid monolayer between the lower layer of an aqueous phase and the upper layer of an oil phase. The white arrow indicates the position of a planar lipid monolayer. (b) Chamber used for observation from the side to capture dynamic behavior and (c) for observation from the bottom to capture quasi-static behavior.

To obtain an oil solution containing dissolved phospholipids (DOPC or eggPC), first, phospholipids dissolved in the organic solvent were poured into a glass test tube. The

organic solvent was then evaporated under nitrogen flow and dried under vacuum for at least 2 hours to produce a dry lipid film at the bottom of the test tube. Mineral oil was then added to the test tube prior to ultrasonication for 60 minutes at 30-50°C and vortex mixing. In our experiment we prepared oil solutions with 1 mM DOPC, 0.1 mM DOPC, and with 0.5 mM eggPC, which are suitable for the formation of GUVs in the aqueous phase, to observe dynamic and quasi-static behaviors. Characteristic adsorption time of phospholipids at these concentrations onto the oil/water interface is within the order of minute [203].

Figure 8.1 shows a schematic illustration of the experimental setup for the spontaneous transfer method. With this method we can prepare GUVs from cell-sized W/O droplets of arbitrary solutions. In the experiment to observe the dynamics of the transfer process, the lipid monolayers coating the droplets and the planar monolayer between the aqueous phase and oil phase had the same composition of 1 mM DOPC. To perform the transfer method, first, 200 μL distilled water was introduced at the bottom of the chamber (aqueous phase), and then 190 μL mineral oil containing dissolved phospholipid DOPC at a concentration 1 mM was gently placed on the water phase (oil phase). The chamber containing aqueous and oil phases was then incubated for about 2 hours at ambient temperature ($\sim 24^\circ\text{C}$) to form a planar phospholipid monolayer that covered the oil/water interface. Second, cell-sized water droplets dispersed in mineral oil were prepared by adding 5 vol% of distilled water to oil that contained 1 mM phospholipid, and the mixture was then emulsified by tapping, as reported previously [21, 143]. Third, the 10 μL of the emulsion solution was poured on the placed oil phase. Water droplets fall to touch the planar monolayer at the oil/water interface, and then spontaneously transfer across the monolayer, resulting in the formation of GUVs. The transfer process was performed in a narrow observation chamber between two glass slides, as shown in Fig. 8.1(b). The transfer process was observed from the side by use of a hand-made microscope for lateral observation. The interface and gravitationally sinking droplets were checked by fluorescent observation before the measurement. The entire penetration process was then measured by bright field observation. Sequential images were obtained by a CCD camera (EIA W100, Watec) and directly captured by a personal computer through a grabber board (Solios Matrox).

We also performed phase-contrast microscopy from underneath the chamber to obtain the spatial distribution of droplets with various radii. We can recognize whether the equatorial lines of droplets are located in the oil phase or water phase by interfacial contrast. In this experiment, 15 μL of distilled water (aqueous phase) was introduced at the bottom of a cylindrical chamber that consisted of a poly(dimethylsiloxane) (PDMS) sheet on a glass slide, as shown in Fig. 8.1(c), and covered with 7 μL of oil containing 0.1 mM DOPC (oil phase). By using the PDMS cylindrical chamber, we can obtain a relatively-flat mm-scaled oil/water interface. The oil/water interface was then incubated for about 2 hours at ambient temperature as in the case of the dynamic experiment. To obtain W/O droplets, 5 vol% of distilled water was added to the oil containing 0.5 mM eggPC and the mixture was then emulsified by the method described above. Immediately after emulsification, 5 μL of the obtained W/O droplet solution was added to the oil phase. Sixty minutes after the addition of emulsion, we counted droplets by phase-contrast microscopy.

8.3 Results

8.3.1 Observation of transfer kinetics

Figure 8.2(a) exemplifies the dynamics of a droplet crossing the oil/water interface after touching the interface. The droplet radius is $41\ \mu\text{m}$. The phospholipid-coated droplet spontaneously transfers across the interface, where it is covered by a planar phospholipid monolayer, accompanied by adhesion of the two monolayers. As shown, the droplet travels downward, accompanied by transfer at the interface. Figure 8.2(b) shows a spatiotemporal trace of the vertical displacement z of the top of the droplet with time t . $t = 0\ \text{s}$ and $z = 0\ \mu\text{m}$ are defined as when the droplet touches the planar monolayer at the interface. Thus, the vertical displacement z corresponds to the depth of penetration of the droplet into the oil/water interface. The entire transfer process can be characterized by three kinetic regimes: (1) approaching regime, (2) entering regime, and (3) relaxation regime. In the approaching regime ($t < 0$), the droplet approaches the interface at a very slow vertical velocity dz/dt . The velocity becomes almost 0 as the droplet touches the interface due to dissipation of the thinning oil film between the droplet and the planar interface [214]. At the initial velocity $dz/dt \approx 0$ in the entering regime, it starts to transfer across the oil/water interface. In this entering regime, the droplet moves rapidly downward. The driving force of

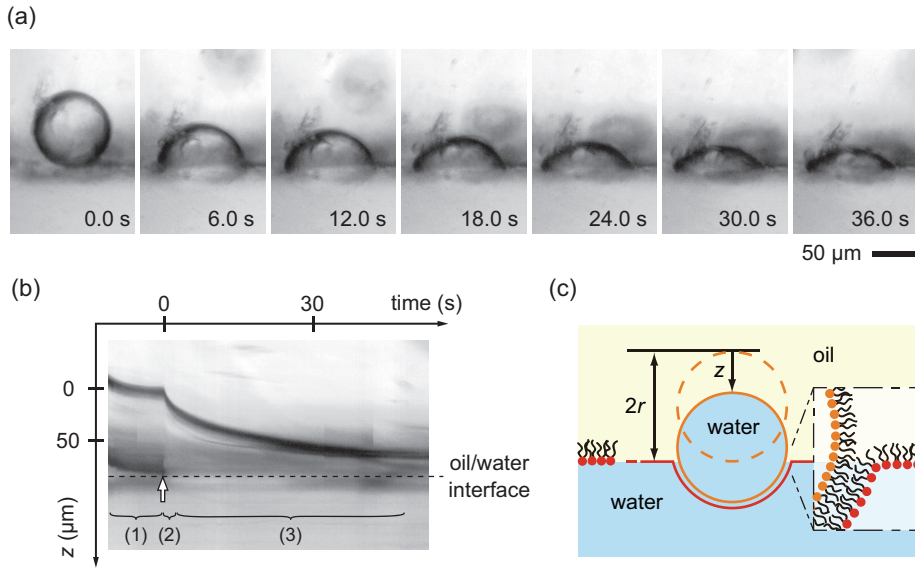


Figure 8.2: Transfer of a droplet in oil into water. A droplet coated by a DOPC monolayer moves across a planar lipid monolayer through the formation of a lipid bilayer in a spontaneous manner. (a) Snapshots of the transfer of a droplet with a radius of $41\ \mu\text{m}$. Time 0 is defined as the point at which it first touches onto the interface. The scale bar corresponds to $50\ \mu\text{m}$. (b) Spatiotemporal diagram of the droplet transfer process. White arrow indicates the onset of transfer. The overall process is characterized by three kinetic regimes: (1) approaching regime, (2) entering regime, and (3) relaxation regime. (c) Schematic illustration of the transfer process.

this motion is the difference in interfacial free energy between two phospholipid monolayers and a bilayer, which is called the adhesive force between the alkyl chains of the two phospholipid monolayers. Some smaller droplets remained at the interface for more than about 10 s before transitioning from the approaching regime to the entering regime, discussed in detail later. After the fast transfer in the entering regime, the velocity decreases as the droplet transfer proceeds in the relaxation regime. The practical problem that droplets tend to stop during transfer is caused by slowness within this relaxation regime. Figure 8.2(c) shows a schematic illustration of a droplet transferring across an oil/water interface, which involves the adhesion of two phospholipid monolayers, where r and z denote the droplet radius and the penetration distance, respectively.

8.3.2 Size dependence of transfer kinetics

Next, we focus on the process corresponding to the entering regime and the relaxation regime after the onset of transfer. The temporal changes in the displacements of the tops of droplets with various radii ranging from $9\ \mu\text{m}$ to $61\ \mu\text{m}$ are shown in Fig. 8.3 ((a) linear, (b) double-logarithmic, and (c) nondimensionalized plots), where the vertical axes $\zeta = z/r$ denote vertical displacements normalized with respect to each droplet radius r . Thus, $\zeta = 0$ and $\zeta = 2$ correspond to the onset and the end of the transfer process, respectively. The radii are classified as $r \leq 20\ \mu\text{m}$ shown by red lines, $20\ \mu\text{m} < r \leq 40\ \mu\text{m}$ by green lines, and $40\ \mu\text{m} < r$ by blue lines. Interestingly, the transit time of droplets across the interface was found to be size-dependent. As shown in Fig. 8.3(a), bigger droplets require much more time to reach a certain position ζ than smaller droplets. This size-dependence is consistent with a previous report [213]. Thus, bigger droplets show a dramatic reduction in the speed of penetration and the transfer process almost stops on a practical time-scale, while smaller droplets easily transfer across the interface completely on this time-scale. Although the size of the droplets has significant effects, a common kinetic process is noted through the scaling procedure, as shown in Fig. 8.3. In the entering regime at less than $t = 1\ \text{s}$, the time evolutions of the normalized displacements ζ of both small and large droplets show an acceleration of penetration with a rough scaling law of $\zeta \sim t^2$, as notably shown in the double-logarithmic plot (Fig. 8.3(b)). The parallel shift of the lines for bigger droplets to a longer time region means that bigger droplets undergo the same transfer process as smaller droplets albeit more slowly. On the other hand, in the later relaxation regime, the slopes of the lines show a slowing of transfer with a rough scaling law of $\zeta \sim t^{0.5}$ or less. Compared to the scaling in the former entering regime ($\zeta \sim t^2$), this decreased time exponent indicates deceleration in the later relaxation regime of the transfer process. This tendency in the droplet transfer process clearly emerges in the nondimensionalized plot shown in Fig. 8.3(c). $\tau = t/t_0$ represents nondimensionalized time, normalized by each characteristic time t_0 determined as the time when $\zeta = 1$. It also exhibits the entering and relaxation regimes, as expressed with the rough scaling laws of $\zeta \sim \tau^2$ and $\zeta \sim \tau^{0.5}$, respectively. Moreover, Fig. 8.3(c) shows that both the qualitative and quantitative behaviors of droplets with various radii are similar in terms of nondimensional displacement ζ and nondimensional time τ . Furthermore, Fig. 8.3(c) shows that the details in the entering regime have somewhat different characteristics depending on the size of the droplets, although they do not affect the comprehensive behaviors; in this regime the slopes of the lines for bigger droplets become less steep than those for smaller droplets.

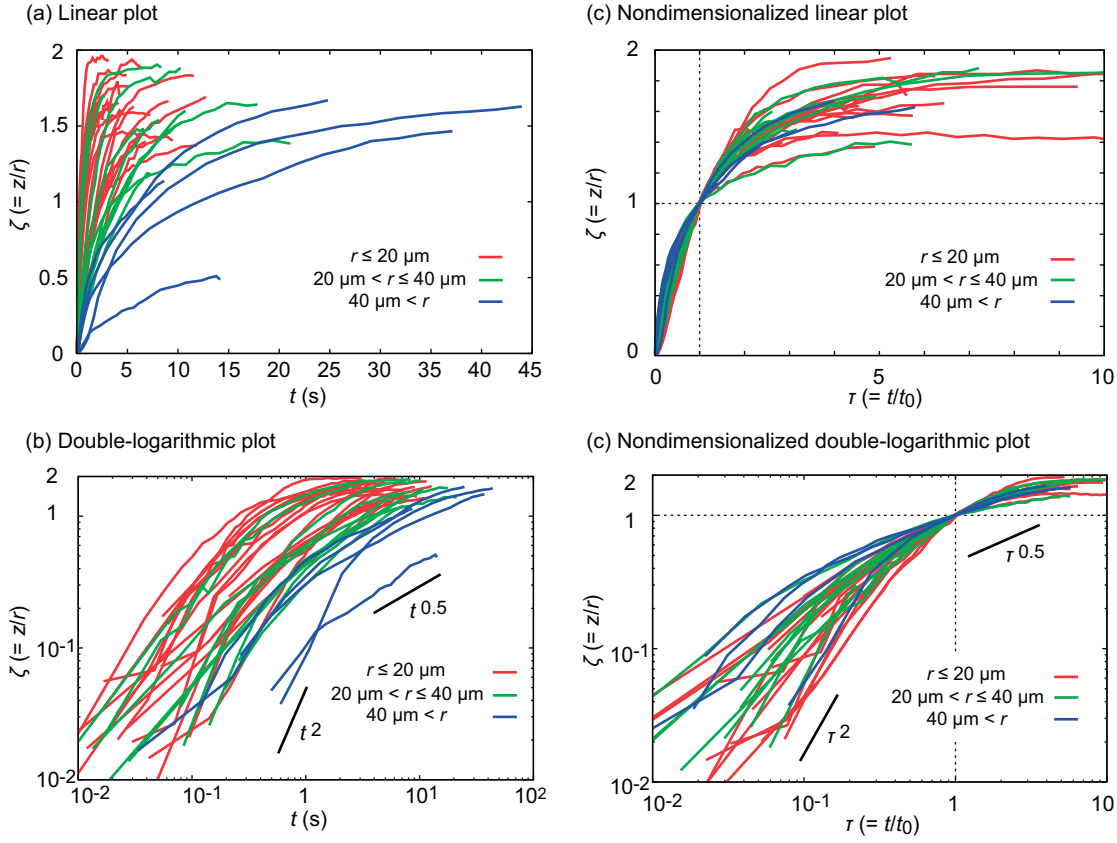


Figure 8.3: Time course of the transfer process of water droplets into an aqueous phase. The total number of analyzed droplets is 32. The radii varied between $9 \mu\text{m}$ and $61 \mu\text{m}$. (a) Positions of the droplets vs. time, where the positions were normalized with respect to the radii; $\zeta = z/r$ (see Fig. 2c). To depict the size-dependence of the transfer process, time courses are shown in different colors; red for $r \leq 20 \mu\text{m}$, green for $20 \mu\text{m} < r \leq 40 \mu\text{m}$, and blue for $40 \mu\text{m} < r$. (b) Double-logarithmic plot of the time courses. (c) Nondimensionalized plot, where each time is nondimensionalized by each characteristic time t_0 , which is the time when $\zeta = 1$. The graphs and the inset show the double-logarithmic and linear plots, respectively. These three plots show the entering and relaxation regimes, as well as the dependence of the transfer process on the droplet size (see the text for details).

8.4 Discussion

8.4.1 Theoretical modeling

Phospholipid-coated droplets transfer through an oil/water interface quickly in the initial entering regime and slowly in the later relaxation regime, where the characteristic scaling laws are $\zeta \sim \tau^2$ and $\zeta \sim \tau^{0.5}$, respectively. To establish a transfer method for the efficient formation of GUVs, it is important that we elucidate the dynamical transfer mechanism from a physicochemical perspective. Therefore, we tried to construct a theoretical framework to interpret the essential features of kinetics in the transfer process.

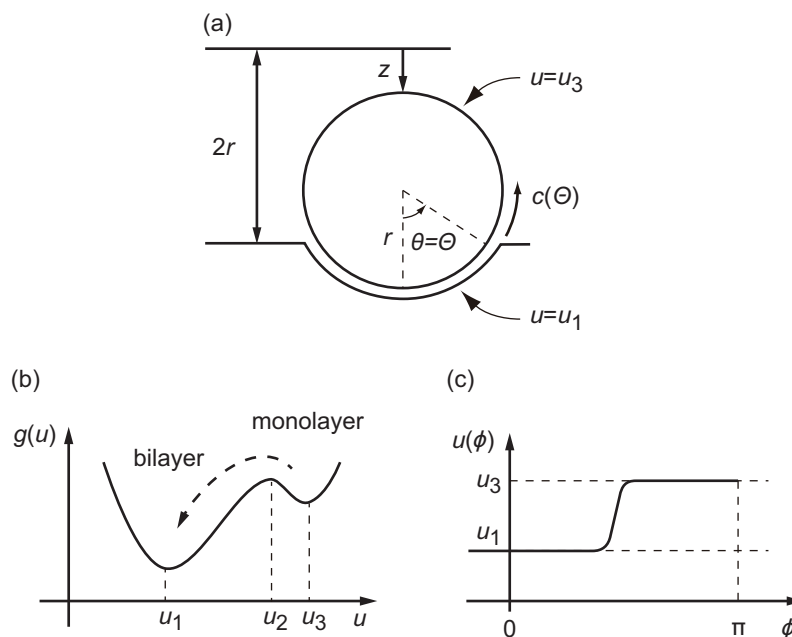


Figure 8.4: (a) Geometric relationships used in the theoretical model. The order parameter u on the surface of a droplet with radius r is either u_1 or u_3 , corresponding to a lipid bilayer or a lipid monolayer, respectively. During the transfer of a droplet across the planar lipid monolayer, the wave front between u_1 and u_3 at polar angle $\theta = \Theta$ travels at a speed $c(\Theta)$. This figure does not show the azimuthal angle because it is symmetric, while we assume that the droplet has a two-dimensional spherical surface. (b) A sketch of the graph of $g(u)$. The order parameter at the traveling wave front $u(\Theta)$ transits from $u = u_3$ to $u = u_1$ as indicated by the dashed arrow. (c) A sketch of the situation in the proper boundary conditions. The traveling wave front exists at a finite ϕ ($-\infty < \phi \leq \pi$)

Here, we consider a phenomenological bistable system described with an order parameter u , which represents the bistable surface state of a droplet as $u = u_1$ for the phospholipid bilayer and $u = u_3$ for the phospholipid monolayer. The geometry is schematically shown in Fig. 8.4(a), where $c(\Theta)$, $\theta = \Theta$, and r are the velocity of the adhesion front of the two phospholipid monolayers, the polar angle of the adhesion front, and the radius of the droplet, respectively. For the sign of $c(\Theta)$, the direction in which the area of the bilayer increases and that of the monolayer decreases is taken as positive (see Fig. 8.4(a)). The two adhering monolayers are the monolayer coating a droplet and that at the planar oil/water interface, as mentioned in the previous section. Thus, the adhesion front is a transition point of order parameter u from $u = u_3$ to $u = u_1$. In our theoretical model, we assume that a phospholipid bilayer and a phospholipid monolayer can transiently coexist and the bilayer region is considered to increase by traveling of the “order parameter wave” on the surface of the droplet with time. For simplicity, the droplet radius r is fixed as a state variable throughout the traveling process. This assumption corresponds to the approximation of an undeformable droplet. Thus, in our theoretical model, the dynamical transfer process of a droplet is described by the kinetics of the traveling wave front of order parameter u .

First, the non-uniform Ginzburg-Landau free energy on the surface of a droplet is given

as

$$F = \int dr \left[g(u) + \frac{K}{2} |\nabla u|^2 \right], \quad (8.1)$$

where $g(u)$ is the quartic surface free energy as a function of u , and K is a positive constant that represents the line tension stored at the triple contact line of the bilayer and the two monolayers in this situation. In our system, the relation $g(u_1) < g(u_3)$ is needed for the surface free energy (see Fig. 8.4(b)). This relationship yields a driving force for the wave front to proceed in the direction $c(\Theta) > 0$, as seen in wetting phenomena [215, 216]. If we assume that the time development of order parameter u on the droplet surface is associated with a decrease in free energy (8.1), we obtain the evolution equation of the system:

$$\frac{\partial u}{\partial t} = -L \frac{\delta F}{\delta u} = f(u) + \frac{D}{r^2} \left(\frac{1}{\tan \theta} \frac{\partial u}{\partial \theta} + \frac{\partial^2 u}{\partial \theta^2} \right), \quad (8.2)$$

where L is a positive kinetic coefficient, $f(u) = -Ldg/du = -a(u - u_1)(u - u_2)(u - u_3)$ ($a > 0$), and $D = LK$ is a positive constant. Equation (8.2) is a one-dimensional reaction-diffusion equation. [217] In this equation, when the variables are transformed using $\phi = \theta - c(\Theta)t$ ($-\infty < \phi \leq \pi$), which is a coordinate seen from the wave front, Eq. (8.2) becomes

$$\frac{D}{r^2} \frac{d^2 u}{d\phi^2} = -f(u) - \left(c(\Theta) + \frac{D}{r^2 \tan \Theta} \right) \frac{du}{d\phi}. \quad (8.3)$$

Here, we replaced $\tan \theta$ by $\tan \Theta$ because $du/d\phi$ is nearly 0, except that $\theta = \Theta$ at the wave front, assuming that the width of the wave front is sufficiently thin (see Fig. 8.4(c)). Equation (8.3) is the fundamental kinetic equation that describes the dynamics of droplet transfer. Next, we solve Eq. (8.3) for $c(\Theta)$, which represents the kinetic behavior of the droplet as it depends on the stage of the transfer $\theta = \Theta$. If we set the boundary conditions as $u(\phi = -\infty) = u_1$, $u(\phi = \pi) = u_3$, and $du/d\phi(u = u_1) = du/d\phi(u = u_3) = 0$, as represented in Fig. 8.4(c), and then assume $du/d\phi = -\alpha(u - u_1)(u - u_3)$ ($\alpha > 0$) as the simplest form of $du/d\phi$ that satisfies the boundary conditions, we can solve Eq. (8.3) for

$$c(\Theta) = \frac{1}{r} \left(\frac{aD}{2} \right)^{\frac{1}{2}} (2u_2 - u_1 - u_3) - \frac{D}{r^2 \tan \Theta}, \quad (8.4)$$

where u_2 is the instability point in $g(u)$ between two stability points u_1 and u_3 . In Eq. (8.4), the first term corresponds to a positive velocity, which is inversely proportional to the curvature radius r , while the second term corresponds to a more potent spherical effect proportional to the inverse square of r and the polar angle of the wave front $\theta = \Theta$. If we consider the geometrical relationship $z = r(1 - \cos \theta)$ and $\zeta = z/r$, we obtain the vertical velocity from Eq. (8.4) as follows:

$$c(\zeta) = \frac{1}{r} \left(\frac{aD}{2} \right)^{\frac{1}{2}} (2u_2 - u_1 - u_3) \{ \zeta(2 - \zeta) \}^{\frac{1}{2}} - \frac{D}{r^2} (1 - \zeta). \quad (8.5)$$

The vertical velocity is negative at the onset of transfer $\zeta = 0$ due to the line tension in the second term. This means that the wave front cannot start before the gain of energy from the surface energy difference between the bilayer and the two monolayers exceeds the energy loss of line tension stored along the circle of the wave front. This negative velocity at the onset of transfer prevents droplets from entering the interface. Indeed, some droplets,

especially smaller droplets, remain on the interface for more than ~ 10 s prior to the onset of transfer in our experiment. This is consistent with the presence of a negative velocity in our theoretical model.

After this energy barrier is overcome by fluctuation of the initial adhesion area of the two phospholipid monolayers, the wave front starts to proceed toward the top of the droplet with a positive velocity. However, this positive velocity of Eq. (8.5) has a non-negligible absolute value even at the end of the transfer process ($\zeta \approx 2$) because the procession of the wave front in the latter half of the process is accompanied by a decrease in the contact line along the wave front, as expressed in the positive second term of Eq. (8.5). With this decrease in the contact line, the velocity will tend to increase. This increase in velocity is not consistent with our experimental result that the velocity decrease in the relaxation regime (see Fig. 8.2). Thus, the adhesion rate, which depends on the contact angle of the two monolayers should also be considered to effectively decelerate the process of adhesion. Since our model is based on the reaction-diffusion equation (8.2) for propagation of the wave front, the adhesion rate can be introduced in an effective diffusion coefficient

$$D = D_0 \exp \left[-\frac{U_{\text{fold}}}{k_{\text{B}}T} \right], \quad (8.6)$$

where U_{fold} , k_{B} , and T are the potential barrier to the adhesion of two monolayers, Boltzmann constant, and absolute temperature, respectively. Here, we use $U_{\text{fold}} = U_{\text{max}}\zeta/2$ as the simplest form to represent an increase in the barrier height with an increase in the contact angle, assuming that it becomes more difficult for the two monolayers to approach and touch each other due to thermal agitation when they increase the distance. To be precise, U_{fold} reflects sensitive features on the molecular-scale contact angle of the liquid-liquid interface with a surfactant. However, here we adopt the simplest linearly increasing form as U_{fold} to extract the essence of the transfer mechanism.

From Eqs. (8.5) and (8.6), we obtain the essential kinetic behavior of the transfer process. Figure 8.5 shows the normalized penetration distance ζ of droplets with three different radii r obtained by integrating the vertical velocity $c(\zeta)$ (Eq. (8.5)) with the effective diffusion coefficient $D(\zeta)$ (Eq. (8.6)), and this corresponds to the experimental result (Fig. 8.3). The fixed parameters are $(a/2)^{1/2}(2u_2 - u_1 - u_3) = 3$, $D_0 = 0.01$, $U_{\text{max}} = 3$, and $k_{\text{B}}T = 1$. $\bar{\tau}$ is the calculation time. Due to the deceleration factor $D(\zeta)$, the velocity decreases in the later process and reproduces well the qualitative behavior of the transfer process, which indicates that the entering regime and the relaxation regime have different scaling relationships, $\zeta \sim \bar{\tau}^2$ and $\zeta \sim \bar{\tau}^{0.5}$, respectively (Fig. 8.5). In addition to the scaling law, Fig. 8.5 well reproduces the size-dependent behavior seen in the present experiment. As shown, it takes a long time for the wave front to travel on the surface of a droplet with a larger radius r , as noted in the previous section. In our model, the transit time $t(\zeta = 2)$ or characteristic time $t_0 = t(\zeta = 1)$ is qualitatively proportional to the square of the droplet radius r due to the contribution of both the circumference, which is proportional to r , and the dominant velocity of the first term, which is inversely proportional to r , in Eq. (8.5). This size-dependence is qualitatively in good agreement with the size-dependence of the characteristic time t_0 in the experiment. In addition, as depicted in the nondimensionalized plot (Fig. 8.5(c)), it is obvious that the slopes of the lines for bigger droplets are not as steep as those for smaller droplets in the short time region corresponding to the entering regime, consistent with the experiment (Fig. 8.3(c)).

Furthermore, in terms of the size-dependence, Eqs. (8.5) and (8.6) predict the initial vertical position ζ where the droplets start to transfer across the interface. As shown by the

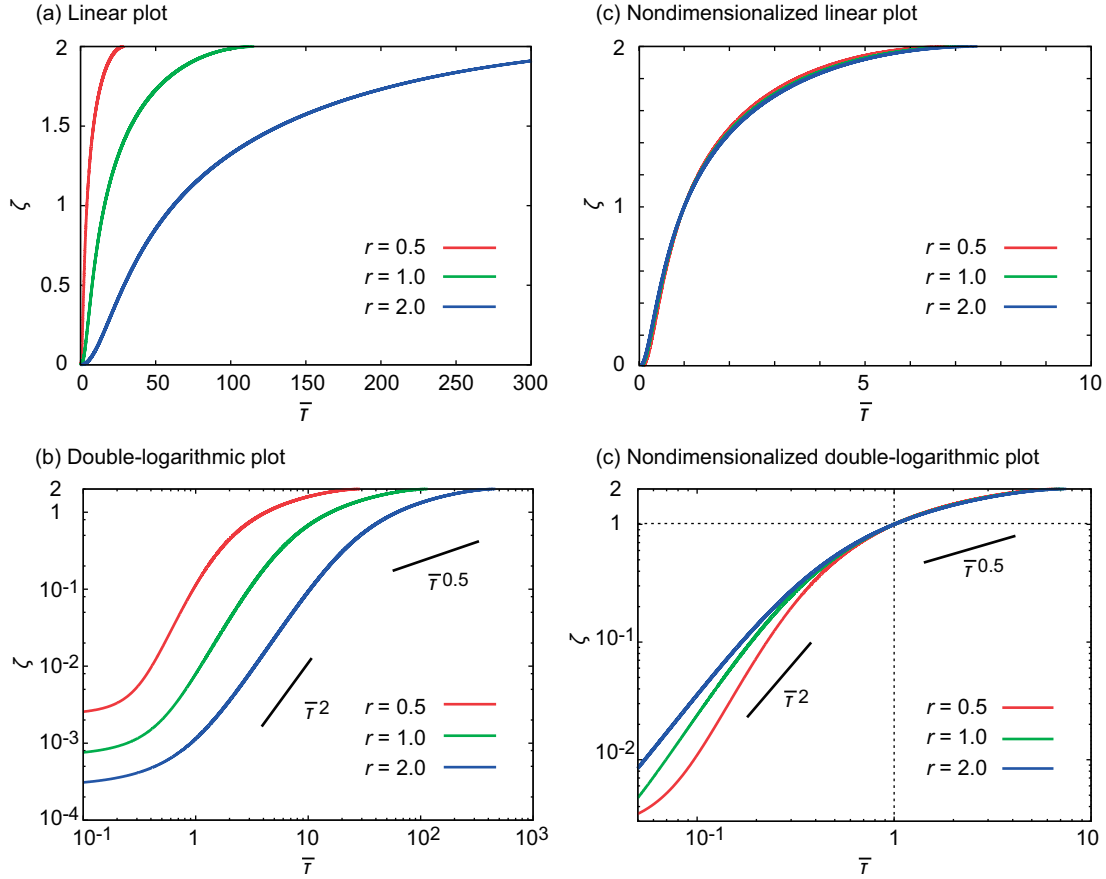


Figure 8.5: Theoretical model of the time-development of the droplet transfer process. The typical behavior of the penetration distance ζ in (a) linear, (b) double-logarithmic, and (c) nondimensionalized plots was obtained by the numerical integration of $c(\Theta)$. $\bar{\tau}$ is an adequate computational time for the integration of Eqs. (8.5) and (8.6) with $(a/2)^{1/2}(2u_2 - u_1 - u_3) = 3$, $D_0 = 0.01$, and $U_{\max} = 3$. The red, green, and blue lines correspond to droplet radii of $r = 0.5$, $r = 1$, and $r = 2$, respectively. The size-dependent outline and the time exponents are qualitatively in good agreement with the experimental results shown in Fig. 3.

double-logarithmic plot (Fig. 8.5(b)), droplets with radii r start to transfer at positions $\zeta \neq 0$ depending on r . These initial positions reflect the transition points $c(\zeta^*) = 0$ from negative to positive. This size-dependence is mainly due to the second term of $c(\zeta)$ (Eq. (8.5)) as proportional to $-r^{-2}(1 - \zeta)$. This term makes the transition point ζ^* for the onset of transfer smaller as the radius r increases. This indicates that bigger droplets readily start to transfer because the initial penetration length ζ^* at which the velocity exceeds $c < 0$ is shorter than that for smaller droplets. Although this initial size-dependence emerges in the transition from the approaching regime to the entering regime and does not emerge in the present experimental analysis for the entering and relaxation regimes shown in Fig. 8.3, it can be confirmed by conducting an independent quasi-static experiment.

Figure 8.6 shows the spatial distribution of droplets classified in terms of three positions: droplets on the interface, those beneath the interface, and those completely transferred into the aqueous phase. Figure 8.6(b) shows a histogram of their proportions at 60 minutes after

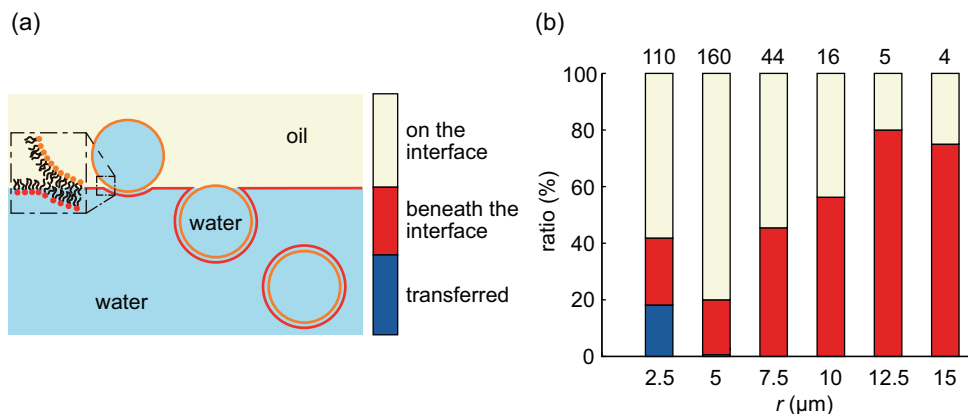


Figure 8.6: Experimental observation of the quasi-static distribution of spatial positions of droplets with various radii. (a) Schematic illustration of the three categories of spatial position corresponding to the histogram in (b). (b) Spatial distribution of droplets with various radii r at 60 minutes after the lipid-coated droplets were placed in the chamber. The number of data points for each size is shown above each bar. The width of individual bar in the histogram is $2.5 \mu\text{m}$, thus, for instance, $10 \mu\text{m}$ means the frequency for the droplets with the radius between 8.75 and $11.25 \mu\text{m}$. The histogram (b) indicates that smaller droplets are likely to settle on the planar monolayer or at the bottom of the aqueous phase, while bigger droplets are likely to stop during transfer, and are suspended under the planar monolayer.

W/O droplets were added to the chamber. The histogram apparently shows that smaller droplets tend to remain on the interface compared to larger droplets, and this tendency is consistent with the experimental observation of the dynamics and the prediction based on the theoretical model. Moreover, the higher number of completely transferred smaller droplets is also consistent with both the experimental dynamics and the model, in that it is easier for smaller droplets to transfer completely than larger droplets once transfer starts because the transit time increases dramatically with the square of the droplet radius r . This result indicates that complete transfer across the interface on a practical time-scale requires an appropriate droplet size: the droplet must be sufficiently large for transfer at the interface to start and sufficiently small so that the transit time is not too long. From Fig. 8.6, for spontaneous transfer, the appropriate size is in the range of $1 \mu\text{m} - 10 \mu\text{m}$.

8.4.2 Potential barrier to the adhesion of two monolayers

As the deceleration factor for the adhesion of two monolayers, we use the potential barrier U_{fold} in our theoretical model. U_{fold} implicitly includes the effects of the deformation of phospholipid monolayers, *i.e.*, the deformation of droplets and an oil/water interface, and the viscous dissipation of flowing oil out of the wedge consisting of two monolayers [214,218]. Indeed, the droplet in Fig. 8.2(a) slightly deforms from a sphere to a stretched shape like a biconvex lens due to the tension of the planar interface. This biconvex-like deformation of droplets corresponds to an increase in the contact angle Θ between the two monolayers, resulting in larger U_{fold} and a slower transfer process, and also an increase in the radius of the sphere r , which also results in a slower transfer. The deformation of a droplet is expected to be size-dependent due to Laplace pressure, which is inversely proportional to the radius r . Since bigger droplets with smaller Laplace pressure are easier to deform than

smaller droplets, a larger U_{fold} can cause a further slowing down compared to the numerical calculation shown in Fig. 8.5. With regard to the effect of viscous dissipation, flowing oil from the confined wedge causes dissipation of the driving force, especially when the contact angle is small. This factor also shifts the potential barrier U_{fold} to higher value at around $\zeta \approx 0$. The theoretical model presented here is a fundamental framework of a mathematical treatment, but in the future we should consider the effects of size-dependent deformation and viscous dissipation. A match in osmolarity between the outer aqueous solution and inner aqueous solution is empirically known to be necessary for efficient transfer. This would mean that the deformation of droplets would be limited and they would retain their initial spherical shape.

In addition, application of the mass density difference between the outer and inner aqueous solutions is also known to be effective for complete transfer as an empirical technique. For instance, equimolar sucroses and glucoses are widely used in inner and outer aqueous solutions for this purpose [34, 187, 203]. The mass density difference is expected to be effective for reducing of the time before the onset of transfer across the interface. Thus, it helps the initial droplets in oil sink into the aqueous phase more deeply and overcome the transition point ζ^* . However, mass density difference is considered to be ineffective during spontaneous transfer because the length scale of GUVs (several tens of μm) is sufficiently small compared to the typical capillary length of $\sim \text{mm}$, within which gravitational force can be ignored compared to interfacial tension in oil/water interfacial phenomena. If there are multiple interfaces in a μm -scaled system, *e.g.*, the lipid monolayer and the lipid bilayer on the surface of a droplet in our system, the difference in interfacial tension is the dominant driving force, and gravitational force is masked except under centrifugation. Thus, the greater efficiency of transfer in the case of a mass density difference would not be due to the gravitational force but rather to the relatively strong adhesion of the lipid monolayers caused by the presence of sugars, which would affect lipid configurations at a molecular scale, although the actual cause is still unclear [219–223]. The effect of aqueous solutions on the transfer process should also be investigated by further experiments.

8.4.3 Relation to the force balance model

In our theoretical model, the driving force of transfer can be explained in terms of phenomenological free energy (Eq. (8.1)). On the other hand, this wetting phenomenon can generally be represented by Young’s law. Recently, the approaching and breaching dynamics of μm -scale colloidal particles at a planar oil/water interface have been reported [214]. The breaching dynamics of such particles, corresponding to the entering regime in our system, can be expressed by the interfacial force balance including a dissipation term from fluid flow near the contact line. On the other hand, we consider a theoretical model that does not include the interfacial tension σ explicitly, and instead adopts a bistable free energy F and potential barrier U_{fold} . The driving force of the difference in interfacial tension described by the Young-Dupré equation corresponds to $g(u_1) < g(u_3)$ in our reaction-diffusion model. Further, the position-dependent term $\sigma \cos \Theta$, which is derived from the planar interface and is important for describing the kinetic behavior in the force balance expression, corresponds to a Laplacian operator on a spherical surface in our model (see Eq. (8.2)). The other interfacial tension $\sigma \sin \Theta$ from the planar interface, which is in a direction normal to the spherical surface, is not treated in either the force balance model or our model due to an approximation of non-deformability, but in our model the term that causes the deformation of a droplet can be included in U_{fold} as mentioned above.

In the transfer method, it has been confirmed empirically that the formation of an intact planar lipid monolayer by placement of the aqueous and oil layers in a chamber for several hours improves the efficiency of transfer. This could be interpreted to the result of tiny interfacial tension $\sigma \sin \Theta$ from the planar monolayer due to complete coverage of the interface with surfactant molecules. $\sigma \sin \Theta$ from the planar monolayer stretches a droplet into a biconvex shape and impedes transfer. Thus, a decrease in σ prevents deformation of the droplet, and consequently the wave front proceeds on a undeformed spherical surface.

Assuming the interfacial force balance in the transfer method [214], the interfacial forces lead to the following two results: the surface area expansion in the lipid bilayer region due to the stretch by the interfacial tension of planar oil/water interface, and the surface state transition from lipid monolayer to bilayer caused by the adhesion of two monolayers. In the present model we considered only the latter factor. Since typical lipid bilayers rupture when the area expansion by stretching reaches 2–4% [224, 225], the droplet-rupture during the transfer across the interface is caused when the velocity of the adhesion front $c(\Theta)$ is slower than the stretching rate. Thus, the adhesion front should proceed at a rate above the stretching rate and below the supply rate of lipid molecules. Successful droplet-to-vesicle transfer indicates that such a proper adhesion rate is feasible, but for instance, defects on the interface could cause alteration of the rate, resulting in a higher probability of the rupture.

8.5 Conclusion

We elucidated the dynamical transfer process of droplets across an oil/water interface. Droplet transfer is accompanied by the adhesion of two lipid monolayers and the formation of lipid bilayer vesicles. Droplets exhibit spontaneous transfer characterized by three different kinetic regimes: an approaching regime where W/O droplets show a decrease in velocity during their approach and touch the oil/water interface, an entering regime where they quickly break into the aqueous phase with a roughly square-dependence of the penetration distance ζ on time t , and a relaxation regime where they show a decrease in velocity with a roughly square root-dependence of ζ on time t . In addition, we found that bigger droplets require more time to transfer than smaller droplets. We have proposed a fundamental theoretical concept to interpret the transfer kinetics based on propagation of the wave front within the framework of reaction-diffusion. Our theoretical model reproduces the essential aspects of the transfer kinetics, including the size-dependence of the transfer process. The present study suggests that the appropriate experimental conditions for transfer are a droplet size of around μm , the formation of a defectless planar monolayer for the suppression of the deformation, a wide basin of attraction for the formation of a bilayer with long alkyl chains, etc. Our theoretical framework may provide a scaffold for further experimental developments of the transfer methods.

Chapter 9

Application of kinetic filtration effect

In this chapter, we report a centrifugal microfluidic method, droplet-shooting and size-filtration (DSSF), for the production of cell-sized liposomes with controlled lipid compositions. This involves the generation of large and small droplets from the tip of a glass capillary and the selective transfer of small droplets through an oil-water interface, thus resulting in the generation of cell-sized liposomes. The DSSF method involves simple microfluidics and is easy to use. In addition, only a small volume (0.5–2 μL) of sample solution is required for the formation of hundreds of cell-sized liposomes. We believe that this method can be applied to generate cell-sized liposomes for a wide variety of uses, such as the construction of artificial cell-like systems.

9.1 Introduction

Cell-sized liposomes [226] have been used in a wide range of fields in biochemistry and biophysics owing to their biological resemblance to cell membranes; however, the bottom-up synthesis of artificial cell-like systems is challenging [202,226,227]. Three liposome properties are required for the construction of artificial cell-like systems: 1) cell-sized diameter (1–30 μm), 2) efficient encapsulation of biochemical reaction systems, such as protein expression systems [202,227–230], and 3) controlled lipid composition to enable the formation of lipid-membrane structures that resemble those in living cells, that is, microdomains as models of lipid rafts [35,231–234] and the asymmetry of inner/outer leaflets in lipid-bilayer membranes [201,207,210,235]. These structures are known to be important for the reconstruction of functional membrane proteins on liposome membranes [236,237]. To date, the droplet transfer method [201,202,210,213,238] and microfluidic approaches [203,206,239–246] have been developed to generate artificial cell-like liposomes that efficiently encapsulate biochemical reaction systems. In the droplet transfer method, control of lipid compositions has been reported, but the size of liposomes cannot be controlled. Microfluidic approaches have the advantage of uniformly sized liposomes; however, technological challenges in the construction of cell-sized liposomes with controlled lipid composition remain [235,245,246].

We present a simple and robust method for the formation of cell-sized liposomes with controlled lipid compositions by using a centrifugal capillary-based microfluidic device [247] coupled with the droplet transfer method (Fig. 9.1(a–c)). This method is based on two physical principles: 1) small (cell-sized) and large water microdroplets are discharged from

the tip of a glass capillary by centrifugation [247] into an oil phase, thereby resulting in the formation of lipid-stabilized water-in-oil (W/O) microdroplets; 2) the small lipid-stabilized W/O microdroplets are spontaneously selected by kinetic size filtration in droplet transfer through an oil-water interface, and the transferred small lipid-stabilized W/O microdroplets form liposomes (Fig. 9.1(b) and 9.1(c)). We call this method “droplet shooting and size filtration” (DSSF). We demonstrate that the DSSF method can produce hundreds of cell-sized liposomes from 1 mL of sample solution and that it can control the lipid compositions. Because the DSSF method is based on the droplet transfer method, efficient encapsulation of biochemical reaction systems was also achieved, and as it has a simple microfluidic configuration it is easy to use. Therefore, we believe that this method will promote the chemical and biomedical use of cell-sized liposomes, as well as the study of artificial cell-like systems.

9.2 Materials and methods

9.2.1 Materials

L- α -phosphatidylcholine (EggPC), dioleoyl phosphatidylcholine (DOPC), dipalmitoyl phosphatidylcholine (DPPC), and cholesterol (Chol) were obtained from Avanti Polar Lipids. Hexadecane, glucose, and sucrose were from Wako Pure Chemical Industries (Osaka, Japan); mineral oil was from Nacalai Tesque Inc (Kyoto, Japan); Span 80 detergent (sorbitan monooleate) was from Tokyo Chemical Industry Co. Ltd (Tokyo, Japan); Rhodamine-Red-labeled dextran (Rho-dextran, 155 kDa, T1287) was from Sigma-Aldrich. Deionized water was obtained from a Millipore Milli-Q system.

9.2.2 Fabrication of a microfluidic device

The microfluidic device (Fig. 9.1(a) and 9.1(d)) was composed of a polyacetal plastic holder, a glass capillary (TST150-6, World Precision Instruments, Inc., Sarasota, FL), and a 1.5 mL polypropylene microtube (MP150-HC; Nikkyo Technos, Co., Tokyo, Japan). Polyacetal plastic plates (2.0 mm in thickness) were milled into three circular plates and assembled with three M2 \times 0.25 screws (Fig. 9.1(e)). The tip of the capillary was sharpened with a PC-10 puller (Narishige Co., Tokyo, Japan) and cut out with an MF-900 microforge (Narishige Co., Ltd.).

9.2.3 Preparation of an oil phase with lipids

Lipids mixture (20 mL of 10 mM in chloroform/methanol (2:1, v/v)) was poured into a glass tube. The lipid composition depended on the experiment. The organic solvent was then evaporated by air flow to form a dry film at the bottom of the glass tube. The tube was placed in a desiccator for 60 min. Mineral oil (200 μ L) was then added to the glass tube. Finally, the glass tube was sonicated in an ultrasonicator at 50°C for 60 min, with vortex mixing. The final lipid concentration was 1 mM.

9.2.4 Generation of cell-sized liposomes

In order to create an oil-water interface in the microtube, an external solution of liposomes (aqueous phase, 30 μ L) was introduced to the microtube, and then covered with oil (170 μ L) containing lipids (1 mM; Fig. 9.1(g)). The lipid composition was DOPC/EggPC, 1:1.

The microtube was then incubated at room temperature ($\sim 25^\circ\text{C}$) for 30 min. The internal liposome solution (1 mL, Rho-dextran (5%, w/v)) was injected into the glass capillary. Internal and external solutions of liposomes depended on the experiment. The glass capillary was placed in a holder then in a microtube. The distance between the tip of the glass capillary and the air-oil interface was 6 mm (Fig. 9.1(h)). The microtube was then centrifuged (1600 *g*, 3 min) in an ATT101 desktop centrifuge (Hi-Tech Co., Tokyo, Japan); liposomes were generated in the microtube. A hole was made in the bottom of the microtube with a pushpin, and liposomes were collected through the hole and poured into another microtube. Liposomes were observed by using an FV1000 confocal laser scanning microscope (Olympus).

9.2.5 Investigation of the size distribution of microdroplets discharged from the glass capillary

Hexadecane (60 mL) containing Span 80 (5%, w/w) was added to the microtube (Supporting Information), then Rho-dextran (1mL, 5%, w/v) was injected into the glass capillary and placed it in the polyacetal holder. The holder was installed in a microtube and centrifuged (1600 *g*, 1–2 s). Images of the surfactant-stabilized W/O microdroplets generated in the microtube were captured in a VHX-2000 digital microscope (Keyence, Osaka, Japan).

9.2.6 Generation of W/O microdroplets by hand tapping, and generation of liposomes by the standard droplet transfer method

An oil phase containing lipids was prepared as described above (DOPC/EggPC, 1:1)., Rho-dextran (1 mL, 5%, w/v) was added to oil (50 mL) containing lipids, and the mixture was emulsified by hand tapping to obtain lipid-stabilized W/O microdroplets. The oil-water interface was prepared as described above. Lipid-stabilized W/O microdroplets were injected into the microtube and centrifuged (1600 *g*, 3 min). Liposomes were collected as described above and observed with the confocal microscope.

9.3 Results

9.3.1 Droplet-shooting and size-filtration (DSSF) method

We generated liposomes by using a microfluidic device (Fig. 9.1(a)) comprised of a glass capillary containing an “internal” solution of liposomes, a capillary holder, and a microtube containing an oil phase and an aqueous phase (an “external” solution of liposomes). In the first experiment, 5% (w/v) Rhodamine Red-labeled dextran (155 kDa; Rho-dextran) was used as the internal solution. We injected 1 mL of internal solution into the glass capillary and placed the glass capillary into the holder (Fig. 9.1(d–f)). An aqueous phase (30 mL of deionized water) was added to the microtube and covered with the oil phase (170 mL) to create an oil-water interface in the microtube. The oil phase was mineral oil containing 1 mm phosphatidylcholine (PC; a 1:1 mixture of dioleoyl phosphatidylcholine (DOPC) and L- α -phosphatidylcholine (EggPC)). We installed the holder with the glass capillary in the microtube (Fig. 9.1(f)) and set the distance between the tip of the glass capillary and the air-oil interface to 6 mm (Fig. 9.1(h)). Finally, we centrifuged the microtube at 1600*g* for 3 min. Hundreds of liposomes were obtained, and these were stable for more than one week (Fig. 9.2(a–c)). From the differential interference contrast (DIC; Fig. 9.2(a))

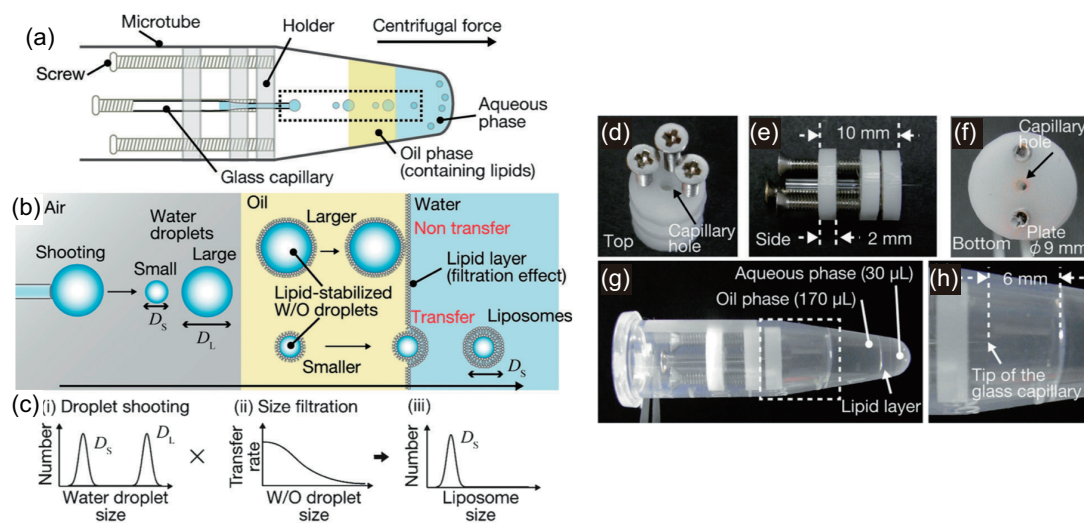


Figure 9.1: Formation of cell-sized liposomes by the DSSF method. (a) Capillary-based microfluidic device. (b) Generation of cell-sized liposomes (within the rectangle shown in (a)). (c) Principle of the DSSF method: (i) small (cell-size) and large droplet formation from the glass capillary; (ii) spontaneous selection of small droplets by kinetic size filtration in the droplet transfer process at the oil-water interface; (iii) generation of cell-sized liposomes. (d) Top, (e) side, and (f) bottom views of the polyacetal plastic holder. (g) Holder with glass capillary installed in the microtube. (h) Detailed view (within the rectangle shown in (g)). The distance between the tip of the glass capillary and the air-oil interface is 6 mm.

and confocal laser scanning microscope (CLSM) images of the generated liposomes, the mean and standard deviation (SD) of liposome diameter were determined as 14.5 and 4.3 μm , respectively (Fig. 9.2(c)), thus demonstrating that liposomes generated by the DSSF method are uniform and cell-sized.

Next, we evaluated the yield of generated liposomes. From DIC images (*e.g.*, Fig. 9.2(a)), we estimated the total number of liposomes generated in a single experiment. The total number of microdroplets generated from the tip of the glass capillary was calculated from the volume of the internal solution (1 mL) introduced into the glass capillary. Liposome yield was obtained by dividing the total number of generated liposomes by the total number of generated microdroplets; 10–20% of the generated microdroplets formed liposomes. Extending the centrifugation time to 10 min did not improve the yield.

9.3.2 Mechanism of cell-sized liposome generation by DSSF method

To investigate the mechanism of liposome generation, we first assessed the size distribution of microdroplets discharged from the tip of the glass capillary. Microdroplets were captured as surfactant-stabilized W/O microdroplets. The microtube contained only an oil phase with a surfactant (Span 80) to stabilize microdroplets. From the microscope image of surfactant-stabilized W/O microdroplets generated from a capillary with a diameter of 10 μm (Fig. 9.3(a) and 9.3(b)), the size distribution exhibits two peaks, attributed to the large and small microdroplets in Fig. 9.3(a). Small microdroplets form when large microdroplets detached from the capillary (Fig. 9.3(c)), as previously reported [247, 248]. The size distribution of the liposomes (Fig. 9.2(c)) was almost the same as that of the small mi-

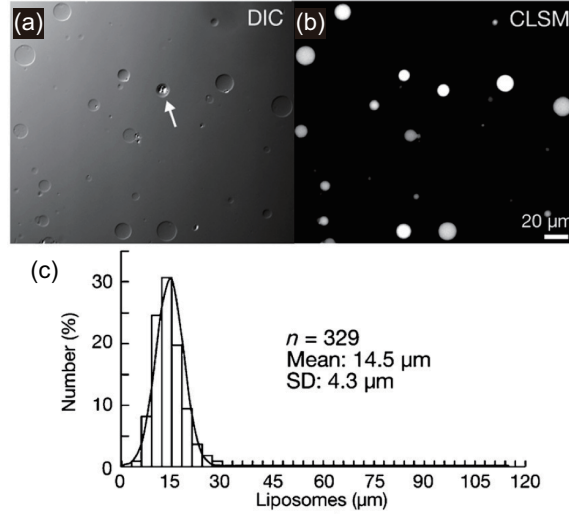


Figure 9.2: Formation of cell-sized liposomes. (a) DIC and (b) CLSM images of cell-sized liposomes encapsulating Rho-dextran. The white arrow identifies a multilamellar liposome. (c) Size distribution of liposomes.

crodroplets (Fig. 9.3(b)), thus indicating that only small microdroplets discharged from the glass capillary were transferred into the aqueous phase and formed liposomes. Several large microdroplets were also transferred into the aqueous phase and formed liposomes; however, most of these stayed on the oil-water interface or disintegrated during the transfer process.

In order to determine the mechanism underlying the dependence of microdroplet sizes on the transfer process at the oil-water interface, we investigated the dependence of microdroplet size on the transfer rate. We first produced lipid-stabilized W/O microdroplets coated with PC (DOPC/EggPC, 1:1) by hand tapping (Fig. 9.4(a)). We centrifuged the lipid-stabilized W/O microdroplets at 1600 g for 3 min and obtained liposomes (Fig. 9.4(b)). Only lipid-stabilized W/O microdroplets smaller than $\sim 30 \mu\text{m}$ in diameter were transferred at the oil-water interface and formed liposomes (compare Fig. 9.4(a) and 9.4(b)). We calculated the relative transfer rate of liposomes for each droplet size (Fig. 9.4(c), circles). To explain the results, a theoretical transfer rate $T(r)$ was calculated by integrating the size-dependent transfer velocity [138]:

$$T(r; \tau) = \frac{1}{2} \int_0^\tau \left[\frac{1}{r} \left(\frac{aD}{2} \right)^{\frac{1}{2}} \left\{ \zeta(t)(2 - \zeta(t)) \right\}^{\frac{1}{2}} - \frac{D}{r^2} (1 - \zeta(t)) \right] dt, \quad (9.1)$$

where $\zeta = z(t)/r$; $z(t)$ is transfer depth, r is droplet radius, D is a position-dependent kinetic coefficient, and a , u_1 , u_2 , and u_3 are positive constants (Supporting Information). We assumed that the transfer rate is proportional to the theoretically predicted penetration depth of the microdroplets into an oil-water interface at a certain time after the start of transfer. The theoretical transfer rate (gray line in Fig. 9.4(c)) indicates that smaller droplets tend to transfer more readily than larger ones, in semi-quantitative agreement with the experimental results. The size-dependent transfer mechanism plays a role in the kinetic filtration effect by which we successfully obtained cell-sized liposomes.

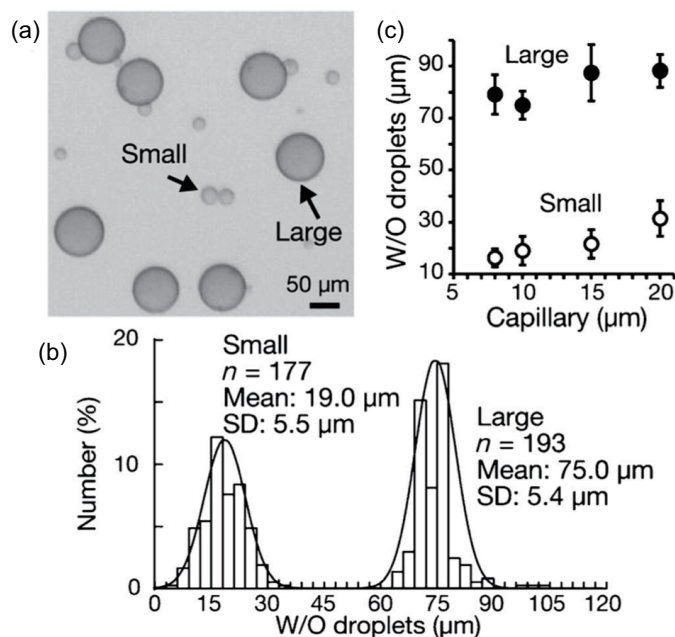


Figure 9.3: Size distribution of precursor microdroplets discharged from the glass capillary. (a) Microscope image. (b) Size distribution of surfactant-stabilized W/O microdroplets encapsulating Rho-dextran (155 kDa) by using a 10 μm capillary. (c) Diameters of small and large surfactant-stabilized W/O microdroplets in each diameter of capillary orifice.

9.4 Conclusion

We present the DSSF centrifugal microfluidic method for the production of cell-sized liposomes (10–20 μm) with controlled lipid composition, by filtration of cell-sized droplets generated by centrifugal droplet shooting. We confirmed that filtration was associated with the kinetic size-dependence of the droplet transfer, and we characterized the unilamellarity of the generated liposome membranes.

These liposomes are suitable for the construction of artificial cell-like systems because of the ability to control lipid compositions as well as efficient encapsulation and unilamellarity of the membrane. Moreover, a very small volume (1 mL) was sufficient to generate hundreds of liposomes without any wasted material. Compared with other microfluidic approaches, the DSSF method therefore has the advantage of producing hundreds of cell-sized liposomes with asymmetric membranes [235, 246].

We anticipate that this method will be easily applied to the construction of cell-sized liposomes with more complex lipid compositions, in order to examine membrane interactions, such as cell adhesion and cell-cell communication. Our results will be useful for the study of the biochemical and physical properties of cells based on model systems. Furthermore, we believe that this technique will also promote the construction of autonomous dynamic biomolecular systems, such as molecular robots [249, 250], based on liposomes with functional bio-macromolecules.

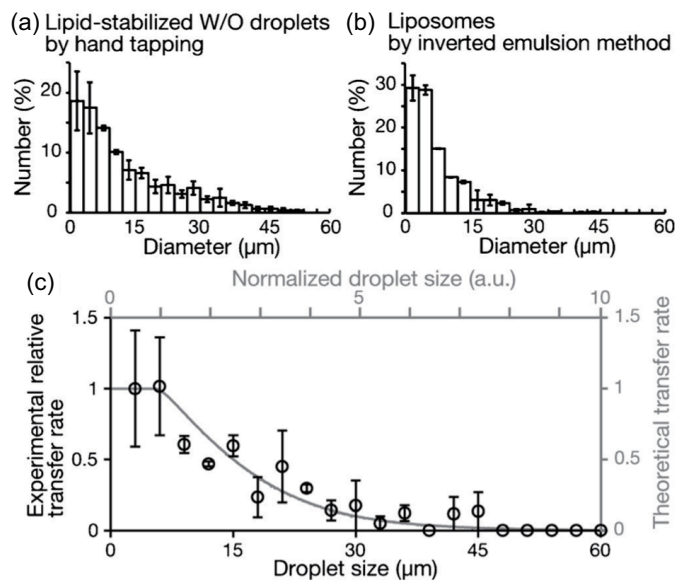


Figure 9.4: Relationship between size of lipid-stabilized W/O microdroplets and transfer rate across the oil-water interface. Size distributions of lipid-stabilized W/O microdroplets obtained by (a) hand tapping ($n = 800$), or (b) the droplet transfer method ($n = 524$). c) Relative transfer rate of lipid-stabilized W/O microdroplets against droplet size (circle) from the experimental results. Theoretical size-dependent transfer rate (gray line) from Eq. (9.1) of the droplet transfer process.

Part V

General conclusion

Chapter 10

General conclusion and future prospects

10.1 General conclusion

Living cells are deformable due to the softness of the interface as well as the spontaneous force generation, in many cases, in the interface, composed of the cell membrane and the underlying cytoskeletal network. We call this dynamic interfaces as “biological interfaces”. In this thesis, we presented experimental studies on the dynamic behaviors of the soft biological interfaces using human red blood cells and reconstituted lipid membranes connected to actomyosin. Throughout the studies, we placed much value on proving the experimental possibilities for the emergence of phenomena and on understanding them in terms of material science by a series of experiments performed in real space.

The shape fluctuation and deformation of human red blood cells are chosen as the simplest system of living cells with the cell membrane and cytoskeleton. In part II (Chapter 5), we reported the effects of additives, endotoxins, to the fluctuation and deformation. By combining the experimental techniques, flicker spectroscopy and microfluidics, we revealed that the endotoxins alter the bending stiffness and spring constant for shape confinement, originated from the cell membrane and the underlying spectrin network, respectively. These effects were proved to be enhanced according to the elongation of endotoxin molecules. Under the influence of the endotoxins, the increase in the mean-shape change from discocytes to unhealthy echinocytes was also observed. The comparison between adult and neonatal red blood cells revealed that the mechanical parameters of neonatal red blood cells are more susceptible to the perturbative effects for bending stiffness and spring constant, as the disease by endotoxins tends to be severer to new-born babies than to adults. Thanks to the microfluidic method, the slight recovery from these effects by the administration of anti-septic peptide P19-2.5 was also experimentally checked, but the deformed mean-shape did not recover. The dramatic change in the spring constant is the direct experimental proof that the cytoskeletal function itself can be attacked by the additives although the spectrin network is hidden beneath the membrane. Together, it was proven that the organization of spectrin should be taken into account for the properties of the shape fluctuation and deformation contrary to the previous work.

Further studies on the out-of-equilibrium fluctuation and deformation of biological interfaces were performed using a novel reconstituted system implementing intrinsic force generation by actin and myosin, which are the well-known cytoskeletal protein and the cor-

responding motor protein, respectively. In Part III, we presented the novel reconstituted system capable of interfacial deformation induced by encapsulated actomyosin. Here the purpose of the work was to elucidate the actual contributions of actin and myosin to the interfacial phenomena as biological soft matters, rather than the complex functions that are sophisticatedly controlled actomyosin in living cells. In this work we achieved the active interfacial fluctuation and deformation induced by actomyosin *in vitro* for the first time. The encapsulated actomyosin, which was distributed homogeneously inside the droplet as an initial condition, self-assembled into two kinds of structure over time: aster structure and cortex structure. The contractile aster structure caused the active interfacial fluctuation by bridging the aster core and the interface (Chapter 6). Moreover, the emergent fluctuating deviation had non-periodicity and non-Gaussianity. These properties indicated the physical law of the interfacial deviation with approximately-linear spring and shot-noise terms, which were from geometrical confinement effect by closed spherical interface and possibly from the properties of the force generation mechanism by myosin, respectively. On the other hand, the contractile cortex structure caused the interfacial wrinkling by its lateral contraction. The experimental analyses revealed that the wrinkled shape profile, which should be determined by the native property of actomyosin contractile cortex, depended on the droplet size, namely the curvature radius of the interface. The theoretical model based on the both elastic and contractile energy of the cortex reproduced the curvature dependence, and the material properties such as feasible cortex thickness and the ratio between elasticity and contractility were quantitatively obtained.

The reconstituted system introduced in Part III was the water-in-oil (W/O) droplet system whose interface was a lipid monolayer at an oil/water interface. In this system the interfacial tension is high enough to suppress large deformation even in the presence of actomyosin contractility. Therefore we explored the experimental method to form a much more flexible lipid bilayer system from the W/O droplet system. For this purpose, the droplet transfer method was introduced in part IV. To address the practical difficulty in the method that cell-sized W/O droplets tend to stop during the transforming into lipid bilayer vesicles, we examined the transfer kinetics and size dependence of the W/O droplets from oil phase to aqueous phase (Chapter 8). By observing the transfer phenomena from the side of the chamber with self-build microscopy, we revealed that larger droplets took much more time to transform into vesicles. We also observed rough scaling laws that characterize the fast regime, in which a droplet touched the interface, and the slow regime, in which the droplet left from the interface. Since the trapping of a droplet at the interface indicates the coexisting state of lipid monolayer interface and lipid bilayer interface, we provided a theoretical model based on reaction diffusion of the order parameter in a phenomenological bistable system. The numerical calculation of this model successfully reproduced the size dependence and the rough scaling in the transfer kinetics. Moreover, the prediction from the model about the onset of the transfer was also confirmed by another experiment, strongly indicating that the model grasp the essential mechanism of the phenomena in the method.

Finally, we extended the droplet transfer method to an automated method by fabricating an easy-to-use device in Chapter 9. In the device, the size dependence revealed in Chapter 8 was applied as a size-filtration mechanism, in which only the small (around $20\ \mu\text{m}$ in diameter) droplets can pass through the interface and transform into bilayer vesicles. In this chapter the size-dependent transfer rate was calculated based on the theoretical model proposed in Chapter 8, and confirmed the consistency with the experimentally obtained transfer rate. The established device can be used for the high throughput production of

lipid bilayer vesicles with a uniform size.

We have studied the fluctuation and deformation of biological interfaces composed not only membranes but also cytoskeletal structures. Through a series of experiments and quantitative analyses in terms of elastic parameters and contractility, it has been clearly revealed that the fluctuation and deformation are crucially affected by the coupling between geometrical effects, *e.g.*, curvature of the interface, and cytoskeletal structures with or without spontaneous force generation. Although many other complex factors should, needless to say, be considered for the complete understanding of the cellular fluctuation and deformation in detail, a rich variety of the interactions between the deformable interfaces and cytoskeletal structures revealed in this thesis would also be taken into account as the start point to consider more complex cellular phenomena, because these results were derived from the material properties.

10.2 Problems and future prospects

There are many future works to be addressed related to the research topics in this thesis. In this section we describe the future works and future prospects.

In Part II, we applied flicker spectroscopy to red blood cell shape fluctuation, but there still remains an open question on the ATP dependence of the fluctuation, as we noted in Part I [66, 67]. It implies that red blood cells may consume ATP during their shape fluctuation under non-equilibrium state, and thus the equipartition theorem may not be applicable. Contributions of ATP to the fluctuation should be clarified in both qualitative and quantitative manner for the future. For example, to measure the fluctuation spectra of exactly the same cells before and after ATP depletion in microfluidic diffusion chamber could provide helpful information. Knockdown of protein 4.1 may also be helpful to clarify whether its phosphorylation can affect the amplitude or not.

Also, it is interesting to see the contributions of the obtained mechanical parameters and their response to endotoxins to the larger deformation, *e.g.*, passing through microcapillary. Because red blood cell dramatically stretched and deformed within microcapillaries in our body's microcirculatory system. We are now measuring the viscoelastic and plastic properties in such larger deformation by combining microfluidics and visual feedback control of the pressure therein as an ongoing work. In this ongoing work, we are seeing interesting dynamics in another time scale of spectrin cytoskeleton, probably related to ATP-consuming cytoskeletal remodeling.

In part III, the active fluctuation and deformation by actin and myosin hierarchical structures were presented. Fabrication of the reconstituted system with interfacial deformation by actomyosin would be the outstanding first step for deeper understanding of the fluctuation and deformation in living systems in bottom up approaches. Further, this could be an epoch-making development in not only biophysics but also other subjects such as biotechnology in creating molecular robots, artificial cells, and so on.

The origin of the non-Gaussian behavior of the active deviation should also be determined by experiments. There are several possibilities that produce the non-Gaussianity: myosin force generation, complete detachments or relatively large detachments of a bundle from the interface, and so on. If it is originated from shot noise of myosin force generation, what can be the origin and how can it contribute to the life phenomena?

Since we adopted microscopic observation in this work, we only focused on the phenomena in mesoscopic scale (1–100 μm in length scale). However, phenomena in the smaller

length scale are still unclear. To elucidate the fundamental mechanisms of the spontaneous hierarchical ordered structures such as aster and cortex, the microscopic information in molecular scale would be necessary in the future. What kind of molecular interaction between actin filaments, *e.g.*, nematic interaction, corresponds to the higher order structure in the confined space would be an interesting question. As another question, how the specific actin binding proteins such as α -actinin, filamin, etc. or related factors such as calcium ions can contribute to the higher order structures and force geometry in the confined space, would also be interesting. In living cells, spatiotemporal distribution of actin and myosin are precisely controlled by these related factors.

In Part IV, we observed the transfer kinetics and reproduced it by phenomenological modeling. To make the fullest possible use of the model to develop the experimental method, the quantitative and exact correspondence between the phenomenological-bistable energy profile and the material parameters in the experiment should be elucidated, although the qualitative correspondences are imagined, *e.g.*, long acyl chains of lipids may correspond to the wide basin for the energy minimum.

The most interesting application of the droplet transfer method in our work is to fabricate the cell-sized lipid bilayer vesicles encapsulating actomyosin. This is ongoing work and will be published elsewhere in the near future.

Acknowledgements

First of all, I would like to express my appreciation to Dr. Masatoshi Ichikawa for his lots of advice from his broad scientific interests throughout my PhD course. In addition, his kind and tolerant supervision had strongly helped me enter the new collaborations with other research fields. He certainly broaden my scientific interests and I really grateful to a lot of opportunities he prepared for us. I also would like to appreciate my former supervisor Prof. Kenichi Yoshikawa, who is now at Doshisha University, for introducing interesting scientific field, physics of life phenomena, to me. Also, he gave me many insightful comments from his panoramic perspective through physics, chemistry, and biology. He had told how to enjoy science and always encouraged me. I am also deeply grateful to Prof. Motomu Tanaka at University of Heidelberg and Institute for Integrated Cell-Material Sciences (iCeMS), Kyoto University. He had kindly hosted me in his group in Heidelberg, Germany, several times and supervised me in a part of my PhD course. Through the collaboration with him, including his group and his many collaborators, I was highly impressed by his attitude to scientific research as well as his passion and creativity that dynamically cross into broad research fields.

I would also like to thank the senior members of Yoshikawa-Ichikawa group, Prof. Hideki Seto (KEK), Assoc. Prof. Hiroyuki Mayama (Asahikawa Medical University), Assoc. Prof. Shin-ichiro M. Nomura (Tohoku University), Dr. Kanta Tsumoto (Mie University), Prof. Damien Baigl (ENS), Dr. Ayako Yamada (Curie Institute), Dr. Shio Inagaki, Dr. Takafumi Iwaki (Oita University), Dr. Norifumi Yamada (KEK), Assoc. Prof. Hiroyuki Kitahata (Chiba University), Assoc. Prof. Tsutomu Hamada (JAIST), Dr. Natsuhiko Yoshinaga (WPI-AIMR, Tohoku University), Assoc. Prof. Yusuke T. Maeda (Kyushu University), Mr. Shun N. Watanabe, Dr. Yoshiko Takenaka (AIST), Dr. Yutaka Sumino (Tokyo University of Science), Dr. Ken H. Nagai (JAIST), Dr. Mafumi Hishida (University of Tsukuba), Assoc. Prof. Miho Yanagisawa (Tokyo University of Agriculture and Technology), Dr. Naofumi Shimokawa (JAIST), Dr. Yuji Higuchi (Tohoku University), Dr. Makito Miyazaki (Waseda University), Mr. Toru Yamanaka, Dr. Ayako Kato, Dr. Fumi Takabatake (Tohoku University), Dr. Akihisa Yamamoto (WPI-iCeMS, Kyoto University), Ms. Yoju Lee, Mr. Eachy Liu, Mr. Hitoshi Hayashi, and Ms. Seiko Hirota for fruitful discussions on my researches and their lots of instructive advice during my PhD. In the laboratory, workshops, conferences, I have learned a lot from communications with them.

I would also like to thank Prof. Masahiro Takagi (JAIST) and Mr. Shou Kato for the experiment of droplet transfer method, Assoc. Prof. Masahiro Takinoue (Tokyo Institute of Technology) and Dr. Masamune Morita (Tokyo Institute of Technology) for inviting me to the fabrication of the device for the transfer method, Dr. Takahiro Fujiwara (WPI-iCeMS) for his professional advice and helps for the microscopic observation, Assoc. Prof. Syuji Fujii (Osaka Institute of Technology) for discussion and sample preparation, Mr. Tomohiko

G. Sano (YITP, Kyoto University) for his helpful comments on the active fluctuation of actomyosin droplets, Assoc. Prof. Seiji Sonobe (University of Hyogo) for his creative sample preparation method of actin and myosin, and Prof. Makoto Kaneko (Osaka University) for valuable comments on red blood cell experiments. My researches in PhD course owe a huge debt to their supports on each aspect of experiments, analyses, and theoretical.

During my several stays in Heidelberg, Germany, I was greatly supported by Dr. Tamas Haraszti (Heidelberg University) for his instruction of optical tweezers, Dr. Kota Miura (The European Molecular Biology Laboratory; EMBL) for lending a precious objective lens, Dr. Bastian E. Rapp (Karlsruhe Institute of Technology), Ms. Elisabeth Wilhelm (Karlsruhe Institute of Technology), and Mr. Christiane Richter née Neumann (Karlsruhe Institute of Technology) for preparing greatly high accuracy microfluidic chips, Prof. Klaus Brandenburg (Research Center Borstel) and Dr. Thomas Gutschmann (Research Center Borstel) for purification of endotoxin molecules and anti-septic peptide, Prof. Johannes M. B. Pöschl (University of Heidelberg), Dr. Navina Kuss (University of Heidelberg) and the medical doctors in Frühkindliche individuelle Pflegestation (FIPS) in Heidelberg University Hospital, especially Ms. Sina Waldherr, Mr. Hannes Hudalla, Ms. Saskia Bredt, for giving insightful comments from a medical aspect and for kind helps to collect samples for my experiment.

Also, I would like to express my gratitude to the members and visitors of Motomu Tanaka group, and would like to thank Dr. Stefan Kaufmann, Dr. Ali Macky (Pierre and Marie Curie University - Paris 6), Dr. Hiroshi Yoshikawa (Saitama University), Dr. Cornelia Monzel (Curie Institute), Dr. Wasim Abuillan, Dr. Alexander Körner, Dr. Alexandra Burk, Dr. Nataliya Frenkel, Mr. Harden Rieger, Mr. Rami Mandow, Mr. Benjamin Flörich, Mr. Shigeto Inoue (from Kao Company), Mr. Taichi Habe (from Kao Company), Mr. Takahisa Matsuzaki (from Saitama University), and Prof. Takahiro Kenmotsu (from Doshisha University) for many supports for my research project there as well as supports for my daily life in Heidelberg. I would also like to appreciate the members of Motomu Tanaka group in Kyoto (WPI-iCeMS), Dr. Marcel Höning, Dr. Akihisa Yamamoto, Dr. Ryo Suzuki, Mr. Florian Gibert (from Heidelberg), and Mr. Benjamin Flörich (from Heidelberg) for the active discussions and helps on experiments.

It would not be possible to study in my PhD here without invaluable helps, encouragements, and stimulating daily discussions with the members of Ichikawa group, Dr. Yukinori Nishigami, Mr. Masahiro Makuta, Mr. Daiki Kado, Mr. Yoshitsugu Kubo, Ms. Tomo Kurimura, Mr. Shunsuke F. Shimobayashi, Mr. Masaki Konosu, Mr. Shunsuke Tsuda, Mr. Takahiro Umeki, Mr. Takuya Ohmura, Mr. Kanta Eto, Mr. Hiroaki Hasegawa, and Mr. Hisanori Fujiwara as colleagues in every aspect of my PhD life.

Last but certainly not least, I give a special thanks to my family and friends for their warm supports every time throughout my research life.

I acknowledge the financial supports from Grant-in-Aid for JSPS research Fellowship for Young Scientists (13J01297).

Bibliography

- [1] E. Schrödinger. *What is life?* University Press, (1967).
- [2] B. Alberts, A. Johnson, J. Lewis, D. Morgan, M. Raff, K. Roberts, and P. Walter, editors. *Molecular Biology of the Cell*, 6th ed. Garland Science, (2014).
- [3] S. J. Singer and G. L. Nicolson, “The fluid mosaic model of the structure of cell membranes”, *Membranes and Viruses in Immunopathology*, pages 7–47 (1972).
- [4] L. D. Frye and M. Edidin, “The rapid intermixing of cell surface antigens after formation of mouse-human heterokaryons”, *J. Cell Sci.*, **7**, 319–335 (1970).
- [5] D. Lingwood and K. Simons, “Lipid rafts as a membrane-organizing principle”, *Science*, **327**, 46–50 (2010).
- [6] A. Kusumi, T. K. Fujiwara, N. Morone, K. J. Yoshida, R. Chadda, M. Xie, R. S. Kasai, and K. G. N. Suzuki, “Membrane mechanisms for signal transduction: The coupling of the meso-scale raft domains to membrane-skeleton-induced compartments and dynamic protein complexes”, *Semin. Cell Dev. Biol.*, **23**, 126–144 (2012).
- [7] K. Simons and E. Ikonen, “Functional rafts in cell membranes”, *Nature*, **387**, 569–572 (1997).
- [8] P. Sharma, R. Varma, R. C. Sarasij, Ira, K. Gousset, G. Krishnamoorthy, M. Rao, and S. Mayor, “Nanoscale organization of multiple gpi-anchored proteins in living cell membranes”, *Cell*, **116**, 577–589 (2004).
- [9] C. Eggeling, C. Ringemann, R. Medda, G. Schwarzmann, K. Sandhoff, S. Polyakova, V. N. Belov, B. Hein, C. von Middendorff, A. Schönle, and S. W. Hell, “Direct observation of the nanoscale dynamics of membrane lipids in a living cell”, *Nature*, **457**, 1159–1162 (2009).
- [10] F. Spira, N. S. Mueller, G. Beck, P. von Olshausen, J. Beig, and R. W.-Söldner, “Patchwork organization of the yeast plasma membrane into numerous coexisting domains”, *Nat. Cell Biol.*, **14**, 640–648 (2012).
- [11] A. Toulmay and W. Prinz, “Direct imaging reveals stable, micrometer-scale lipid domains that segregate proteins in live cells”, *J. Cell Biol.*, **202**, 35–44 (2013).
- [12] F. Gittes, B. Mickey, J. Nettleton, and J. Howard, “Flexural rigidity of microtubules and actin filaments measured from thermal fluctuations in shape”, *J. Cell Biol.*, **120**, 923–934 (1993).

-
- [13] S.-C. Liu, L. H. Derick, and J. Palek, “Visualization of the hexagonal lattice in the erythrocyte membrane skeleton”, *J. Cell Biol.*, **104**, 527–536 (1987).
- [14] V. Bennett, “The spectrin-actin junction of erythrocyte membrane skeletons”, *Biochim. Biophys. Acta*, **988**, 107–121 (1989).
- [15] J. N. Israelachvili. *Intermolecular and Surface Forces: Revised Third Edition*. Academic press, (2011).
- [16] T. Thorsen, R. W. Roberts, F. H. Arnold, and S. R. Quake, “Dynamic pattern formation in a vesicle-generating microfluidic device”, *Phys. Rev. Lett.*, **86**, 4163–4166 (2001).
- [17] S. Okushima, T. Nisisako, T. Torii, and T. Higuchi, “Controlled production of monodisperse double emulsions by two-step droplet breakup in microfluidic devices”, *Langmuir*, **20**, 9905–9908 (2004).
- [18] D. T. Chiu, R. M. Lorenz, and G. D. M. Jeffries, “Droplets for ultrasmall-volume analysis”, *Anal. Chem.*, **81**, 5111–5118 (2009).
- [19] M. Hase and K. Yoshikawa, “Structural transition of actin filament in a cell-sized water droplet with a phospholipid membrane”, *J. Chem. Phys.*, **124**, 104903 (2006).
- [20] M. Hase, A. Yamada, T. Hamada, D. Baigl, and K. Yoshikawa, “Manipulation of cell-sized phospholipid-coated microdroplets and their use as biochemical microreactors”, *Langmuir*, **23**, 348–352 (2007).
- [21] A. Kato, E. Shindo, T. Sakaue, A. Tsuji, and K. Yoshikawa, “Conformational transition of giant dna in confined space surrounded by a phospholipid membrane”, *Biophys. J.*, **97**, 1678–1686 (2009).
- [22] M. Negishi, M. Ichikawa, M. Nakajima, M. Kojima, T. Fukuda, and K. Yoshikawa, “Phase behavior of crowded like-charged mixed polyelectrolytes in a cell-sized sphere”, *Phys. Rev. E*, **83**, 061921 (2011).
- [23] A. Kato, M. Yanagisawa, Y. T. Sato, K. Fujiwara, and K. Yoshikawa, “Cell-sized confinement in microspheres accelerates the reaction of gene expression”, *Sci. Rep.*, **2**, 283 (2012).
- [24] A. D. Bangham and R. W. Horne, “Negative staining of phospholipids and their structural modification by surface-active agents as observed in the electron microscope”, *J. Mol. Biol.*, **8**, 660–IN10 (1964).
- [25] G. Staneva, M. Seigneuret, K. Koumanov, G. Trugnan, and M. I. Angelova, “Detergents induce raft-like domains budding and fission from giant unilamellar heterogeneous vesicles: A direct microscopy observation”, *Chem. Phys. Lipids*, **136**, 55–66 (2005).
- [26] T. Hamada, Y. Miura, K. Ishii, S. Araki, K. Yoshikawa, M. Vestergaard, and M. Takagi, “Dynamic processes in endocytic transformation of a raft-exhibiting giant liposome”, *J. Phys. Chem. B Lett.*, **111**, 10853–10857 (2007).

BIBLIOGRAPHY

- [27] I. Koltover, J. O. Rädler, and C. R. Safinya, “Membrane mediated attraction and ordered aggregation of colloidal particles bound to giant phospholipid vesicles”, *Phys. Rev. Lett.*, **82**, 1991–1994 (1999).
- [28] Y. Yu and S. Granick, “Pearling of lipid vesicles induced by nanoparticles”, *J. Am. Chem. Soc.*, **131**, 14158–14159 (2009).
- [29] M. Schulz, A. Olubummo, and W. H. Binder, “Beyond the lipid-bilayer: Interaction of polymers and nanoparticles with membranes”, *Soft Matter*, **8**, 4849–4864 (2012).
- [30] T. Hamada, M. Morita, M. Miyakawa, R. Sugimoto, A. Hatanaka, M. C. Vestergaard, and M. Takagi, “Size-dependent partitioning of nano/microparticles mediated by membrane lateral heterogeneity”, *J. Am. Chem. Soc.*, **134**, 13990–13996 (2012).
- [31] A. Kato, A. Tsuji, M. Yanagisawa, D. Saeki, K. Juni, Y. Morimoto, and K. Yoshikawa, “Phase separation on a phospholipid membrane inducing a characteristic localization of DNA accompanied by its structural transition”, *J. Phys. Chem. Lett.*, **1**, 3391–3395 (2010).
- [32] K. Kurihara, M. Tamura, K. Shohda, T. Toyota, K. Suzuki, and T. Sugawara, “Self-reproduction of supramolecular giant vesicles combined with the amplification of encapsulated DNA”, *Nat. Chem.*, **3**, 775–781 (2011).
- [33] P. Girard, J. Prost, and P. Bassereau, “Passive or active fluctuations in membranes containing proteins”, *Phys. Rev. Lett.*, **94**, 088102 (2005).
- [34] M. Yanagisawa, M. Iwamoto, A. Kato, K. Yoshikawa, and S. Oiki, “Oriented reconstitution of a membrane protein in a giant unilamellar vesicle: Experimental verification with the potassium channel KcsA”, *J. Am. Chem. Soc.*, **133**, 11774–11779 (2011).
- [35] M. Morita, T. Hamada, Y. Tendo, T. Hata, and M. C. Vestergaard and M. Takagi, “Selective localization of Alzheimer’s amyloid beta in membrane lateral compartments”, *Soft Matter*, **8**, 2816–2819 (2012).
- [36] H. Bouvrais, F. Cornelius, J. H. Ipsen, and O. G. Mouritsen, “Intrinsic reaction-cycle time scale of Na^+ , K^+ -ATPase manifests itself in the lipid-protein interactions of nonequilibrium membranes”, *Proc. Natl. Acad. Sci. U.S.A.*, **109**, 18442–18446 (2012).
- [37] C. S. Scheve, P. A. Gonzales, N. Momin, and J. C. Stachowiak, “Steric pressure between membrane-bound proteins opposes lipid phase separation”, *J. Am. Chem. Soc.*, **135**, 1185–1188 (2013).
- [38] P. B. Canham, “The minimum energy of bending as a possible explanation of the biconcave shape of the human red blood cell”, *J. Theoret. Biol.*, **26**, 61–81 (1970).
- [39] W. Helfrich, “Lipid bilayer spheres: Deformation and birefringence in magnetic fields”, *Phys. Lett.*, **43A**, 409–410 (1973).
- [40] W. S. R. M. Helfrich and R.-M. Servuss, “Undulations, steric interaction and cohesion of fluid membranes”, *Il Nuovo Cimento D*, **3**, 137–151 (1984).

- [41] E. Evans and D. Needham, “Physical properties of surfactant bilayer membranes: Thermal transitions, elasticity, rigidity, cohesion, and colloidal interactions”, *J. Phys. Chem.*, **91**, 4219–4228 (1987).
- [42] E. Evans and W. Rawicz, “Entropy-driven tension and bending elasticity in condensed-fluid membranes”, *Phys. Rev. Lett.*, **64**, 2094–2097 (1990).
- [43] W. Rawicz, K. C. Olbrich, T. McIntosh, D. Needham, and E. Evans, “Effect of chain length and unsaturation on elasticity of lipid bilayers”, *Biophys. J.*, **79**, 328–339 (2000).
- [44] M. P. do Carmo. *Differential geometry of curves and surfaces*, volume 2. Prentice-hall Englewood Cliffs, (1976).
- [45] U. Seifert, “Configurations of fluid membranes and vesicles”, *Advances in Physics*, **46**, 13–137 (1997).
- [46] U. Seifert, L. Miao, H.-G. Döbereiner, and M. Wortis. “Budding transition for bilayer fluid vesicles with area-difference elasticity”. In *The Structure and Conformation of Amphiphilic Membranes*, pages 93–96. Springer, (1992).
- [47] W. Wuese, W. Harbich, and W. Helfrich, “Budding of lipid bilayer vesicles and flat membranes”, *J. Phys.: Condens. Matt.*, **4**, 1647 (1992).
- [48] B. Bozic, S. Svetina, B. Zeks, and R. E. Waugh, “Role of lamellar membrane structure in tether formation from bilayer vesicles”, *Biophys. J.*, **61**, 963 (1992).
- [49] L. Miao, U. Seifert, M. Wortis, and H.-G. Döbereiner, “Budding transitions of fluid-bilayer vesicles: The effect of area-difference elasticity”, *Phys. Rev. E*, **49**, 5389–5407 (1994).
- [50] B. Audoly and Y. Pomeau. *Elasticity and Geometry: From Hair Curls to the Non-linear Response of Shells*. Oxford University Press, (2010).
- [51] S. T. Milner and S. A. Safran, “Dynamical fluctuations of droplet microemulsions and vesicles”, *Phys. Rev. A*, **36**, 4371–4379 (1987).
- [52] F. Brochard and J. F. Lennon, “Frequency spectrum of the flicker phenomenon in erythrocytes”, *J. Phys. (Fr.)*, **36**, 1035–1047 (1975).
- [53] W. Häckl, U. Seifert, and E. Sackmann, “effects of fully and partially solubilized amphiphiles on bilayer bending stiffness and temperature dependence of the effective tension of giant vesicles”, *J. Phys. II France*, **7**, 1141–1157 (1997).
- [54] E. Sackmann, “Membrane bending energy concept of vesicle- and cell-shapes and shape-transitions”, *FEBS Lett.*, **346**, 3–16 (1994).
- [55] M. A. Peterson, “Shape dynamics of nearly spherical membrane bounded fluid cells”, *Mol. Cryst. Liq. Cryst.*, **127**, 257–272 (1985).
- [56] H. Strey, M. Peterson, and E. Sackmann, “Measurement of erythrocyte membrane elasticity by flicker eigenmode decomposition”, *Biophys. J.*, **69**, 478–488 (1995).

BIBLIOGRAPHY

- [57] M. A. Peterson, “Linear response of the human erythrocyte to mechanical stress”, *Phys. Rev. A*, **45**, 4116–4132 (1992).
- [58] R. M. Hochmuth, N. Mohandas, and P. L. Blackshear Jr., “Measurement of the elastic modulus for red cell membrane using a fluid mechanical technique”, *Biophys. J.*, **13**, 747–762 (1973).
- [59] R. Waugh and E. A. Evans, “Thermoelasticity of red blood cell membrane”, *Biophys. J.*, **26**, 115–131 (1979).
- [60] D. E. Discher, N. Mohandas, and E. A. Evans, “Molecular maps of red blood cell deformation: Hidden elasticity and *in situ* connectivity”, *Science*, **266**, 1032–1035 (1994).
- [61] V. Heinrich, K. Ritchie, N. Mohandas, and E. Evans, “Elastic thickness compressibility of the red cell membrane”, *Biophys. J.*, **81**, 1452–1463 (2001).
- [62] H. Engelhardt, H. Gaub, and E. Sackmann, “Viscoelastic properties of erythrocyte membranes in high-frequency electric fields”, *Nature*, **307**, 378–380 (1984).
- [63] N. Gov, A. G. Zilman, and S. Safran, “Cytoskeleton confinement and tension of red blood cell membranes”, *Phys. Rev. Lett.*, **90**, 228101 (2003).
- [64] J. Pécrcéaux, H.-G. Döbereiner, J. Prost, J.-F. Joanny, and P. Bassereau, “Refined contour analysis of giant unilamellar vesicles”, *Eur. Phys. J. E*, **13**, 277–290 (2004).
- [65] Y.-Z. Yoon, H. Hong, A. Brown, D. C. Kim, D. J. Kang, V. L. Lew, and P. Cicuta, “Flickering analysis of erythrocyte mechanical properties: Dependence on oxygenation level, cell shape, and hydration level”, *Biophys. J.*, **97**, 1606–1615 (2009).
- [66] S. Tuvia, A. Almagor, A. Bitler, S. Levin, R. Korenstein, and S. Yedgar, “Cell membrane fluctuations are regulated by medium macroviscosity: Evidence for a metabolic driving force”, *Proc. Natl. Acad. Sci. U.S.A.*, **94**, 5045–5049 (1997).
- [67] T. Betz, M. Lenz, J.-F. Joanny, and C. Cykes, “ATP-dependent mechanics of red blood cells”, *Proc. Natl. Acad. Sci. U.S.A.*, **106**, 15320–15325 (2009).
- [68] E. Ling, Y. N. Danilov, and C. M. Cohen, “Modulation of red cell band 4.1 function by cAMP-dependent kinase and protein kinase C phosphorylation”, *J. Biol. Chem.*, **263**, 2209–2216 (1988).
- [69] S. Manno, Y. Takakuwa, K. Nagao, and N. Mohandas, “Modulation of erythrocyte membrane mechanical function by β -spectrin phosphorylation and dephosphorylation”, *J. Biol. Chem.*, **270**, 5659–5665 (1995).
- [70] S. Manno, Y. Takakuwa, and N. Mohandas, “Modulation of erythrocyte membrane mechanical function by protein 4.1 phosphorylation”, *J. Biol. Chem.*, **280**, 7581–7587 (2005).
- [71] N. S. Gov and S. A. Safran, “Red blood cell membrane fluctuations and shape controlled by ATP-induced cytoskeletal defects”, *Biophys. J.*, **88**, 1859–1874 (2005).

- [72] J. Prost, J.-B. Manneville, and R. Bruinsma, “Fluctuation-magnification of non-equilibrium membranes near a wall”, *Eur. Phys. J. B*, **1**, 465–480 (1998).
- [73] O. Lüderitz, M. A. Freudenberg, C. Galanos, V. Lehmann, E. T. Rietschel, D. H. Shawn, B. Felix, and K. Arnost, “Lipopolysaccharides of gram-negative bacteria”, *Current Topics in Membranes and Transport*, **17**, 339 (1982).
- [74] C. R. Raetz, R. J. Ulevitch, S. D. Wright, C. H. Sibley, A. Ding, and C. F. Nathan, “Gram-negative endotoxin: An extraordinary lipid with profound effects on eukaryotic signal transduction”, *FASEB J.*, **5**, 2652–2660 (1991).
- [75] J. M. B. Pöschl and O. Linderkamp, “Effect of lipid a on the deformability, membrane rigidity and geometry of human adult red blood cells”, *Eur. J. Clin. Invest.*, **22**, 625–629 (1992).
- [76] J. M. B. Pöschl, C. Leray, P. Ruef, J. P. Cazenave, and O. Linderkamp, “endotoxin binding to erythrocyte membrane and erythrocyte deformability in human sepsis and *in vitro*”, *Crit. Care Med.*, **31**, 924–928 (2003).
- [77] O. Linderkamp, J. Pöschl, and P. Ruef, “Blood cell deformation in neonate who have sepsis”, *Neoreviews.*, **7**, 517–523 (2006).
- [78] J. M. B. Pöschl, P. Ruef, M. Schnauffer, S. Pohl, H. G. Sonntag, and O. Linderkamp, “Group b streptococcus impairs erythrocyte deformability in neonates more than in adults”, *Arch. Dis. Child.*, **74**, F187–F190 (1996).
- [79] S. Suresh, J. Spatz, J. P. Mills, A. Micoulet, M. Dao, C. T. Lim, M. Beil, and T. Seufferlein, “Connections between single-cell biomechanics and human disease state: Gastrointestinal cancer and malaria”, *Acta Biomater.*, **1**, 15–30 (2005).
- [80] J. Sleep, D. Wilson, R. Simmons, and W. Gratzer, “Elasticity of the red cell membrane and its relation to hemolytic disorders: An optical tweezers study”, *Biophys. J.*, **77**, 3085–3095 (1999).
- [81] J. Guck, S. Schinkinger, B. Lincoln, F. Wottawah, S. Ebert, M. Romeyke, D. Lenz, H. M. Erickson, R. Ananthakrishnan, D. Mitchell, J. Käs, S. Ulvick, and C. Bilby, “Optical deformability as an inherent cell marker for testing malignant transformation and metastatic competence”, *Biophys. J.*, **88**, 3689–3698 (2005).
- [82] J. Guck, R. Ananthakrishnan, T. J. Moon, C. C. Cunningham, and J. Käs, “The optical stretcher: A novel laser tool to micromanipulate cells”, *Biophys. J.*, **84**, 767–784 (2001).
- [83] J. Guck, R. Ananthakrishnan, T. J. Moon, C. C. Cunningham, and J. Käs, “Optical deformability of soft biological dielectrics”, *Phys. Rev. Lett.*, **84**, 5451–5454 (2000).
- [84] M. A. Peterson, H. Strey, and E. Sackmann, “Theoretical and phase contrast microscopic eigenmode analysis of erythrocyte flicker: Amplitudes”, *J. Phys. II France*, **2**, 1273–1285 (1992).
- [85] H. Engelhardt and E. Sackmann, “On the measurement of shear elastic moduli and viscosities of erythrocyte plasma membranes by transient deformation in high frequency electric fields”, *Biophys. J.*, **54**, 495–508 (1985).

- [86] S. Vrhovec, M. Mally, B. Kavcic, and J. Derganc, “A microfluidic diffusion chamber for reversible environmental changes around flaccid lipid vesicles”, *Lab Chip*, **11**, 4200–4206 (2011).
- [87] K. Brandenburg, J. Andrä, P. Garidel, and T. Gutschmann, “Peptide-based treatment of sepsis”, *Appl. Microbiol. Biotechnol.*, **90**, 799–808 (2011).
- [88] C. Galanos, O. Lüderitz, and O. Westphal, “A new method for the extraction of R lipopolysaccharides”, *Eur. J. Biochem.*, **9**, 245–249 (1969).
- [89] K. Brandenburg and U. Seydel, “Physical aspects of structure and function of membranes made from lipopolysaccharides and free lipid A”, *Biochim. Biophys. Acta*, **775**, 225–238 (1984).
- [90] E. Th. Rietschel, editor. *Handbook of Endotoxin: Chemistry of Endotoxin*. Elsevier, Amsterdam, (1984).
- [91] T. Schuerholz, K. Brandenburg, and G. Marx, “Antimicrobial peptides and their potential application in inflammation and sepsis”, *Crit. Care*, **16**, 207 (2012).
- [92] W. Abuillan, E. Schneck, A. Körner, K. Brandenburg, T. Gutschmann, T. Gill, A. Vorobiev, O. Konovalov, and M. Tanaka, “Physical interactions of fish protamine and antiseptic peptide drugs with bacterial membranes revealed by combination of specular X-ray reflectivity and grazing-incidence X-ray fluorescence”, *Phys. Rev. E*, **88**, 012705 (2013).
- [93] A. Waldbaur, B. Carneiro, P. Hettich, E. Wilhelm, and B. Rapp, “Computer-aided microfluidics (CAMF): From digital 3D-CAD models to physical structures within a day”, *Microfluid. Nanofluid.*, **15**, 625–635 (2013).
- [94] P. Thévenaz, T. Blu, and M. Unser, “Interpolation revisited”, *IEEE Trans. Med. Imaging*, **19**, 739–758 (2000).
- [95] J. P. Hale, P. Winlove, and P. G. Petrov, “Effect of hydroperoxides on red blood cell membrane mechanical properties”, *Biophys. J.*, **101**, 1921–1929 (2011).
- [96] L. G. Mesquita, U. Agero, and O. N. Mesquita, “Defocusing microscopy: An approach for red blood cell optics”, *Appl. Phys. Lett.*, **88**, 133901 (2006).
- [97] J. M. B. Pöschl, P. Ruef, M. Schnauffer, and O. Linderkamp, “The effect of different Escherichia Coli endotoxins on red blood cell deformability”, *Clin. Hemorheol.*, **15**, 749–753 (1995).
- [98] Y.-Z. Yoon, J. Kotar, A. T. Brown, and P. Cicuta, “Red blood cell dynamics: From spontaneous fluctuations to non-linear response”, *Soft Matter*, **7**, 2042–2051 (2011).
- [99] F. C. Mackintosh and A. J. Levine, “Nonequilibrium mechanics and dynamics of motor-activated gels”, *Phys. Rev. Lett.*, **100**, 018104 (2008).
- [100] M. Guo, A. J. Ehrlicher, M. H. Jensen, M. Renz, J. R. Moore, R. D. Goldman, J. Lippincott-Schwartz, F. C. Mackintosh, and D. A. Weitz, “Probing the stochastic, motor-driven properties of the cytoplasm using force spectrum microscopy”, *Cell*, **158**, 822–832 (2014).

- [101] Y. Park, C. A. Best, T. Auth, N. S. Gov, S. A. Safran, G. Popescu, S. Suresh, , and M. S. Feld, “Metabolic remodeling of the human red blood cell membrane”, *Proc. Natl. Acad. Sci. U.S.A.*, **107**, 1289–1294 (2010).
- [102] H. W. G. Lim, M. Wortis, and R. Mukhopadhyay, “Stomatocyte-discocyte-echinocyte sequence of the human red blood cell: Evidence for the bilayer-couple hypothesis from membrane mechanics”, *Proc. Natl. Acad. Sci. U.S.A.*, **99**, 16766–16769 (2002).
- [103] L. L. M. van Deenen, J. A. F. Op den Kamp, B. Roelofsen, and K. W. A. Wirtz, “On membrane phospholipids and protein-lipid association”, *Pure Appl. Chem.*, **54**, 2443–2454 (1982).
- [104] M. P. Sheetz and S. J. Singer, “Biological membranes as bilayer couples. A molecular mechanism of drug-erythrocyte interactions”, *Proc. Natl. Acad. Sci. U.S.A.*, **71**, 4457–4461 (1974).
- [105] T. Fujii, T. Sato, A. Tamura, M. Wakatsuki, and Y. Kanaho, “Shape changes of human erythrocytes induced by various amphipathic drugs acting on the membrane of the intact cells”, *Biochem. Pharmacol.*, **28**, 613–620 (1979).
- [106] B. Lubin, D. Chiu, J. Bastacky, B. Roelofsen, and L. L. M. van Deenen, “Abnormalities in membrane phospholipid organization in sickled erythrocytes”, *J. Clin. Invest.*, **67**, 1643–1649 (1981).
- [107] J. R. Warren, A. S. Harris, and C. H. Wallas, “Transformation of human erythrocyte shape by endotoxic lipopolysaccharide”, *Infect. Immun.*, **39**, 431–434 (1983).
- [108] M. R. Condon, E. Feketova, G. W. Machiedo, E. A. Deitch, and Z. Spolarics, “Augmented erythrocyte band-3 phosphorylation in septic mice”, *Biochim. Biophys. Acta*, **1772**, 580–586 (2007).
- [109] R. M. Hochmuth, “Solid and liquid behavior of red cell membrane”, *Annu. Rev. Biophys. Bioeng.*, **11**, 43–55 (1982).
- [110] O. Linderkamp, G. B. Nash, P. Y. K. Wu, , and H. J. Meiselman, “Deformability and intrinsic material properties of neonatal red blood cells”, *Blood*, **67**, 1244–1250 (1986).
- [111] C. Kodama, “Clinical studies on ATP concentration in the blood of mother and newborn infant, especially on the relationship with the infant jaundice”, *Adv. Obstet. Gynecol.*, **23**, 196–215 (1971).
- [112] E. Schneck, R. G. Oliveira, F. Rehfeldt, B. Demé, K. Brandenburg, U. Seydel, and M. Tanaka, “Mechanical properties of interacting lipopolysaccharide membranes from bacteria mutants studied by specular and neutron scattering”, *Phys. Rev. E*, **80**, 041929 (2009).
- [113] T. Gutschmann, I. Razquin-Olazarán, I. Kowalski, Y. Kaonis, J. Howe, R. Bartels, M. Hornef, T. Schürholz, M. Rössle, S. Sanchez-Gómez, I. Moriyon, G. M. de Tejada, , and K. Brandenburg, “New antiseptic peptides to protect against endotoxin-mediated shock”, *Antimicrob. Agents Chemother.*, **54**, 3817–3824 (2010).

BIBLIOGRAPHY

- [114] Y. Kaconis, I. Kowalski, J. Howe, A. Brauser, W. Richter, I. Razquin-Olazarán, M. I nigo Pestaña, P. Garidel, M. Rössle, G. M. de Tejada, T. Gutschmann, , and K. Brandenburg, “Biophysical mechanisms of endotoxin neutralization by cationic amphiphilic peptides”, *Biophys. J.*, **100**, 2652–2661 (2011).
- [115] D. S. Bailey, A. Cook, G. McAllister, M. Moss, and N. Mian, “Structural and biochemical differentiation of the mammalian small intestine during foetal development”, *J. Cell. Sci.*, **72**, 195–212 (1984).
- [116] K. Keren, Z. Pincus, G. M. Allen, E. L. Barnhart, G. Marriott, A. Mogilner, and J. A. Theriot, “mechanism of shape determination in motile cells”, *Nature*, **453**, 475–480 (2008).
- [117] F. A. Barr, H. H. W. Silljé, and E. A. Nigg, “Polo-like kinases and the orchestration of cell division”, *Nat. Rev. Mol. Cell Biol.*, **5**, 429–440 (2004).
- [118] T. D. Pollard and J. A. Cooper, “Actin, a central player in cell shape and movement”, *Science*, **326**, 1208–1212 (2009).
- [119] S. Kadir, J. W. Astin, L. Tahtamouni, P. Martin, and C. D. Nobes, “Microtubule remodelling is required for the front-rear polarity switch during contact inhibition of locomotion”, *J. Cell. Sci.*, **124**, 2642–2653 (2011).
- [120] I. Mabuchi and M. Okuno, “The effect of myosin antibody on the division of starfish blastomeres”, *J. Cell. Biol.*, **74**, 251–263 (1977).
- [121] A. De Lozanne and J. A. Spudich, “Disruption of the dictyostelium myosin heavy chain gene by homologous recombination”, *Science*, **236**, 1086–1091 (1987).
- [122] G. T. Charras, J. C. Yarrow, M. A. Horton, L. Mahadevan, and T. J. Mitchison, “Non-equilibration of hydrostatic pressure in blebbing cells”, *Nature*, **435**, 365–369 (2005).
- [123] H. Blaser, M. Reichman-Fried, I. Castanon, K. Dumstrei, F. L. Marlow, K. Kawakami, L. Solnica-Krezel, C.-P. Heisenberg, and E. Raz, “Migration of zebrafish primordial germ cells: A role for myosin contraction and cytoplasmic flow”, *Dev. Cell*, **11**, 613–627 (2006).
- [124] M. A. Conti, S. Kawamoto, and R. S. Adelstein. “Non-muscle myosin II”. In *Myosins*, pages 223–264. Springer, (2008).
- [125] P. M. Bendix, G. H. Koenderink, D. Cuvelier, Z. Dogic, B. N. Koeleman, W. M. Briehar, C. M. Field, L. Mahadevan, and D. A. Weitz, “A quantitative analysis of contractility in active cytoskeletal protein networks”, *Biophys. J.*, **94**, 3126–3136 (2008).
- [126] D. Mizuno, C. Tardin, C. F. Schmidt, and F. C. MacKintosh, “Nonequilibrium mechanics of active cytoskeletal networks”, *Science*, **315**, 370–373 (2007).
- [127] T. Toyota, D. A. Head, C. F. Schmidt, and D. Mizuno, “Non-gaussian athermal fluctuations in active gels”, *Soft Matter*, **7**, 3234–3239 (2011).

- [128] B. Stuhmann, M. S. e Silva, M. Depken, F. C. MacKintosh, and G. H. Koenderink, “Nonequilibrium fluctuations of a remodeling *in vitro* cytoskeleton”, *Phys. Rev. E*, **86**, 020901 (2012).
- [129] R. J. Eddy, L. M. Pierini, F. Matsumura, and F. R. Maxfield, “Ca²⁺-dependent myosin II activation is required for uropod retraction during neutrophil migration”, *J. Cell Sci.*, **113**, 1287–1298 (2000).
- [130] F. Sánchez-Madrid and J. M. Serrador, “Bringing up the rear: Defining the roles of the uropod”, *Nat. Rev. Mol. Cell Biol.*, **10**, 353–359 (2009).
- [131] M. Vicente-Manzanares, X. Ma, R. S. Adelstein, and A. R. Horwitz, “Non-muscle myosin II takes centre stage in cell adhesion and migration”, *Nat. Rev. Mol. Cell Biol.*, **10**, 778–790 (2009).
- [132] V. Schaller, C. Weber, C. Semmrich, E. Frey, and A. R. Bausch, “Polar patterns of driven filaments”, *Nature*, **467**, 73–77 (2010).
- [133] R. Butt, T. Mufti, A. Humayun, P. B. Rosenthal, S. Khan, S. Khan, and J. E. Molloy, “Myosin motors drive long range alignment of actin filaments”, *J. Biol. Chem.*, **285**, 4964–4974 (2010).
- [134] F. Backouche, L. Haviv, D. Groswasser, and A. Bernheim-Groswasser, “Active gels: Dynamics of patterning and self-organization”, *Phys. Biol.*, **4**, 264–273 (2006).
- [135] K. Takiguchi, M. Negishi, Y. Tanaka-Takiguchi, M. Homma, and K. Yoshikawa, “Transformation of actoHMM assembly confined in cell-sized liposome”, *Langmuir*, **27**, 11528–11535 (2011).
- [136] K. Carvalho, F.-C. Tsai, E. Lees, R. Voituriez, G. H. Koenderink, and C. Sykes, “Cell-sized liposomes reveal how actomyosin cortical tension drives shape change”, *Proc. Natl. Acad. Sci. U.S.A.*, **110**, 16456–16461 (2013).
- [137] P. Stano, P. Carrara, Y. Kuruma, T. P. de Souza, and P. L. Luisi, “Compartmentalized reactions as a case of soft-matter biotechnology: Synthesis of proteins and nucleic acids inside lipid vesicles”, *J. Mater. Chem.*, **21**, 18887–18902 (2011).
- [138] H. Ito, T. Yamanaka, S. Kato, T. Hamada, M. Takagi, M. Ichikawa, and K. Yoshikawa, *Soft Matter*, **9**, 9539–9547 (2013).
- [139] E. Nishihara, E. Yokota, A. Tazaki, H. Orii, M. Katsuhara, K. Kataoka, H. Igarashi, Y. Moriyama, T. Shimmen, and S. Sonobe, “Presence of aquaporin and V-ATPase on the contractile vacuole of *Amoeba proteus*”, *Biol. Cell*, **100**, 179–188 (2008).
- [140] Y. Nishigami, M. Ichikawa, T. Kazama, R. Kobayashi, T. Shimmen, K. Yoshikawa, and S. Sonobe, “Reconstruction of active regular motion in amoeba extract: Dynamic cooperation between sol and gel states”, *PloS one*, **8**, e70317 (2013).
- [141] M. M. Bradford, “A rapid and sensitive method for the quantitation of microgram quantities of protein utilizing the principle of protein-dye binding”, *Anal. Biochem.*, **72**, 248–254 (1976).

BIBLIOGRAPHY

- [142] U. Laemmli, “Cleavage of structural proteins during the assembly of the head of bacteriophage T4”, *Nature*, **227**, 680–685 (1970).
- [143] H. Ito, M. Yanagisawa, M. Ichikawa, and K. Yoshikawa, “Emergence of a thread-like pattern with charged phospholipids on an oil/water interface”, *J. Chem. Phys.*, **136**, 204903 (2012).
- [144] J. Riedl, A. H. Crevenna, K. Kessenbrock, J. H. Yu, D. Neukirchen, M. Bista, F. Bradke, D. Jenne, T. A. Holak, Z. Werb, et al., “Lifeact: A versatile marker to visualize F-actin”, *Nat. Methods*, **5**, 605–607 (2008).
- [145] T. Thoresen and M. Gardel, “Reconstitution of contractile actomyosin bundles”, *Biophys. J.*, **100**, 2698–2705 (2011).
- [146] M. S. e Silva, M. Depken, B. Stuhmann, M. Korsten, F. C. MacKintosh, and G. H. Koenderink, “Active multistage coarsening of actin networks driven by myosin motors”, *Proc. Natl. Acad. Sci. U.S.A.*, **108**, 9408–9413 (2011).
- [147] M. Miyazaki, M. Chiba, H. Eguchi, T. Ohki, and S. Ishiwata, “Cell-sized spherical confinement induces the spontaneous formation of contractile actomyosin rings *in vitro*”, *Nat. Cell Biol.*, **17**, 480–489 (2015).
- [148] D. Humphrey, C. Duggan, D. Saha, D. Smith, and J. Käs, “Active fluidization of polymer networks through molecular motors”, *Nature*, **416**, 413–416 (2002).
- [149] G. Popescu, T. Ikeda, K. Goda, C. A. Best-Popescu, M. Laposata, S. Manley, R. R. Dasari, K. Badizadegan, and M. S. Feld, “Optical measurement of cell membrane tension”, *Phys. Rev. Lett.*, **97**, 218101 (2006).
- [150] Q.-Z. Zhou, L.-Y. Wang, G.-H. Ma, and Z.-G. Su, “Preparation of uniform-sized agarose beads by microporous membrane emulsification technique”, *J. Colloid Interface Sci.*, **311**, 118–127 (2007).
- [151] M. Yanagisawa, T. Yoshida, M. Furuta, S. Nakata, and M. Tokita, “Adhesive force between paired microdroplets coated with lipid monolayers”, *Soft Matter*, **9**, 5891–5897 (2013).
- [152] A. Nagy, Y. Takagi, N. Billington, S. A. Sun, D. K. T. Hong, E. Homsher, A. Wang, and J. R. Sellers, “Kinetic characterization of nonmuscle myosin IIb at the single molecule level”, *J. Biol. Chem.*, **288**, 709–722 (2013).
- [153] M. T. Valentine, P. D. Kaplan, D. Thota, J. C. Crocker, T. Gisler, R. K. Prud’homme, M. Beck, and D. A. Weitz, “Investigating the microenvironments of inhomogeneous soft materials with multiple particle tracking”, *Phys. Rev. E*, **64**, 061506 (2001).
- [154] P. Chaudhuri, L. Berthier, and W. Kob, “Universal nature of particle displacements close to glass and jamming transitions”, *Phys. Rev. Lett.*, **99**, 060604 (2007).
- [155] N. Yamamoto, M. Ichikawa, and Y. Kimura, “Local mechanical properties of a hyper-swollen lyotropic lamellar phase”, *Phys. Rev. E*, **82**, 021506 (2010).
- [156] Van Kampen and N. Godfried, editors. *Stochastic Processes in Physics and Chemistry*, 2th ed. Elsevier, (2007).

-
- [157] K. Kanazawa, T. G. Sano, T. Sagawa, and H. Hayakawa, “Minimal model of stochastic athermal systems: Origin of non-Gaussian noise”, *Phys. Rev. Lett.*, **114**, 090601 (2015).
- [158] K. Kanazawa, T. G. Sano, T. Sagawa, and H. Hayakawa, “Asymptotic derivation of langevin-like equation with non-Gaussian noise and its analytical solution”, *J. Stat. Phys.*, **160**, 1294–1335 (2015).
- [159] E. Ben-Issac, Y. K. Park, G. Popescu, F. L. H. Brown, N. S. Gov, and Y. Shokef, “Effective temperature of red-blood-cell membrane fluctuations”, *Phys. Rev. Lett.*, **106**, 238103 (2011).
- [160] É. Fodor, M. Guo, N. S. Gov, P. Visco, D. A. Weitz, and F. van Wijland, “Activity-driven fluctuations in living cells”, *Eur. Phys. Lett.*, **110**, 48005 (2015).
- [161] E. Ben-Issac, É. Fodor, P. Visco, F. van Wijland, and N. S. Gov, “Modeling the dynamics of a tracer particle in an elastic active gel”, *Phys. Rev. E*, **92**, 012716 (2015).
- [162] G. Charras and E. Paluch, “Blebs lead the way: How to migrate without lamellipodia”, *Rev. Mol. Cell Biol.*, **9**, 730–736 (2008).
- [163] J. Sedzinski, M. Biro, A. Oswald, J.-Y. Tinevez, G. Salbreux, and E. Paluch, “Polar actomyosin contractility destabilizes the position of the cytokinetic furrow”, *Nature*, **476**, 462–466 (2011).
- [164] M. Zhao, “Electrical fields in wound healing—An overriding signal that directs cell migration”, *Semin. Cell Dev. Biol.*, **20**, 674–682 (2009).
- [165] M. F. Olson and E. Sahai, “The actin cytoskeleton in cancer cell motility”, *Clin. Exp. Metastasis*, **26**, 273–287 (2009).
- [166] A. Bretscher, K. Edwards, and R. G. Fehon, “ERM proteins and merlin: Integrators at the cell cortex”, *Nat. Rev. Mol. Cell Biol.*, **3**, 586–599 (2002).
- [167] M. Biro, Y. Romeo, S. Kroschwald, M. Bovellan, A. Boden, J. Tcherkezian, P. P. Roux, G. Charras, and E. K. Paluch, “Cell cortex composition and homeostasis resolved by integrating proteomics and quantitative imaging”, *Cytoskeleton*, **70**, 741–754 (2013).
- [168] L. Blanchoin, K. Amann, and H. Higgs, “Direct observation of dendritic actin filament networks nucleated by Arp2/3 complex and WASP/Scar proteins”, *Nature*, **404**, 1007–1011 (2000).
- [169] I. Kunita, K. Sato, Y. Tanaka, Y. Takikawa, H. Orihara, and T. Nakagaki, “Shear banding in an f-actin solution”, *Phys. Rev. Lett.*, **109**, 248303 (2012).
- [170] S. M. Heissler and D. J. Manstein, “Comparative kinetic and functional characterization of the motor domains of human nonmuscle myosin-2C isoforms”, *J. Biol. Chem.*, **286**, 21191–21202 (2011).
- [171] W. Häckl, M. Bärmann, and E. Sackmann, “Shape changes of self-assembled actin bilayer composite membranes”, *Phys. Rev. Lett.*, **80**, 1786–1789 (1988).

BIBLIOGRAPHY

- [172] H. Miyata, S. Nishiyama, K. Akashi, and K. Kinoshita, “Protrusive growth from giant liposomes driven by actin polymerization”, *Proc. Natl. Acad. Sci. USA*, **96**, 2048–2053 (1999).
- [173] A. P. Liu, D. L. Richmond, L. Maibaum, S. Pronk, P. L. Geissler, and D. A. Fletcher, “Membrane-induced bundling of actin filaments”, *Nat. Phys.*, **4**, 789–793 (2008).
- [174] S. Köhler, V. Schaller, and A. R. Bausch, “Structure formation in active networks”, *Nat. Mater.*, **10**, 462–468 (2011).
- [175] S. K. Vogel and P. Schwille, “Minimal systems to study membrane-cytoskeleton interactions”, *Curr. Opin. Biotechnol.*, **23**, 758 (2012).
- [176] J. van der Gucht, E. Paluch, J. Plastino, and C. Sykes, “Stress release drives symmetry breaking for actin-based movement”, *Proc. Natl. Acad. Sci. USA*, **102**, 7847–7852 (2005).
- [177] E. Paluch, J. van der Gucht, and C. Sykes, “Cracking up: Symmetry breaking in cellular systems”, *J. Cell. Biol.*, **175**, 687–692 (2006).
- [178] F.-C. Tsai, B. Stuhmann, and G. H. Koenderink, “Encapsulation of active cytoskeletal protein networks in cell-sized liposomes”, *Langmuir*, **27**, 10061–10071 (2011).
- [179] E. Shah and K. Keren, “Symmetry breaking in reconstituted actin cortices”, *Elife*, **3**, e01433 (2014).
- [180] L. Limozin, A. Roth, and E. Sackmann, “Microviscoelastic moduli of biomimetic cell envelopes”, *Phys. Rev. Lett.*, **95**, 178101 (2005).
- [181] Y. Sumino, H. Kitahata, H. Seto, and K. Yoshikawa, “Dynamical blebbing at a droplet interface driven by instability in elastic stress: A novel self-motile system”, *Soft Matter*, **7**, 3204–3212 (2011).
- [182] V. Noireaux, R. M. Golsteyn, E. Friederich, J. Prost, C. Antony, D. Louvard, and C. Sykes, “Growing an actin gel on spherical surfaces”, *Biophys. J.*, **78**, 1643–1654 (2000).
- [183] K. Sekimoto, J. Prost, J. Jülicher, H. Boukellal, and A. Bernheim-Grosswasser, “Role of tensile stress in actin gels and a symmetry-breaking instability”, *Eur. Phys. J. E*, **13**, 247–259 (2004).
- [184] G. T. Charras, C.-K. Hu, M. Coughlin, and T. J. Mitchison, “Reassembly of contractile actin cortex in cell blebs”, *J. Cell Biol.*, **175**, 477–490 (2006).
- [185] B. Maugis, J. Brugués, P. Nassoy, N. Guillen, P. Sens, and F. Amblard, “Dynamic instability of the intracellular pressure drives bleb-based motility”, *J. Cell Sci.*, **123**, 3884–3892 (2010).
- [186] G. Salbreux, G. Charras, and E. Paluch, “Actin cortex mechanics and cellular morphogenesis”, *Trends Cell Biol.*, **22**, 536–545 (2012).
- [187] L.-L. Pontani, J. van der Gucht, G. Salbreux, J. Heuvingh, J.-F. Joanny, and C. Sykes, “Reconstitution of an actin cortex inside a liposome”, *Biophys. J.*, **96**, 192–198 (2009).

- [188] D. Ershov, M. C. Stuart, and J. van der Gucht, “Mechanical properties of reconstituted actin networks at an oilwater interface determined by microrheology”, *Soft Matter*, **8**, 5896 (2012).
- [189] Pier Luigi Luisi, “Chemical aspects of synthetic biology”, *Chem. Biodivers.*, **4**, 603–621 (2007).
- [190] S. M. Nomura, S. Kondoh, W. Asayama, A. Asada, S. Nishikawa, and K. Akiyoshi, “Direct preparation of giant-liposomes by in vitro membrane protein synthesis”, *J. Biotechnol.*, **133**, 190–195 (2008).
- [191] Allen P. Liu and Daniel A. Fletcher, “Biology under construction: in vitro reconstitution of cellular function”, *Nat. Rev. Mol. Cell. Biol.*, **10**, 644–650 (2009).
- [192] V. Noireaux, Yusuke T. Maeda, and A. Libchaber, “Development of an artificial cell, from self-organization to computation and self-reproduction”, *Proc. Nat. Acad. Sci. USA*, **108**, 3473–3480 (2011).
- [193] A. D. Bangham, M. M. Standish, and J. C. Watkins, “Diffusion of univalent ions across the lamellae of swollen phospholipids”, *J. Mol. Biol.*, **13**, 238–252 (1965).
- [194] J. P. Reeves and R. M. Dowben, “Formation and properties of thin-walled phospholipid vesicle”, *J. Cell. Physiol.*, **73**, 49–60 (1969).
- [195] M. Hishida, H. Seto, N. L. Yamada, and K. Yoshikawa, “Hydration process of multi-stacked phospholipid bilayers to form giant vesicles”, *Chem. Phys. Lett.*, **455**, 297–302 (2008).
- [196] K. Tsumoto, H. Matsuo, M. Tomita, and T. Yoshimura, “Efficient formation of giant liposomes through the gentle hydration of phosphatidylcholine films doped with sugar”, *Colloids Surf. B*, **68**, 98–105 (2009).
- [197] Miglena I. Angelova and Dimiter S. Dimitrov, “Liposome electroformation”, *Faraday Discuss. Chem. Soc.*, **81**, 303–311 (1986).
- [198] M. Le Berre, A. Yamada, L. Reck, Y. Chen, and D. Baigl, “Electroformation of giant phospholipid vesicles on a silicon substrate: Advantages of controllable surface properties”, *Langmuir*, **24**, 2643–2649 (2008).
- [199] T. Shimanouchi, H. Umakoshi, and R. Kuboi, “Kinetic study on giant vesicle formation with electroformation method”, *Langmuir*, **25**, 4835–4840 (2009).
- [200] P. Walde, K. Cosentino, H. Engel, and P. Stano, “Giant vesicles: Preparations and applications”, *ChemBioChem*, **11**, 848–865 (2010).
- [201] S. Pautot, Barbara J. Frisken, and D. A. Weitz, “Engineering asymmetric vesicles”, *J. Am. Chem. Soc.*, **100**, 10718–10721 (2003).
- [202] V. Noireaux and Albert Libchaber, “A vesicle bioreactor as a step toward an artificial cell assembly”, *J. Am. Chem. Soc.*, **101**, 17669–17674 (2004).
- [203] M. Abkarian, E. Loiseau, and G. Massiera, “Continuous droplet interface crossing encapsulation (cDICE) for high throughput monodisperse vesicle design”, *Soft Matter*, **7**, 4610–4614 (2011).

BIBLIOGRAPHY

- [204] Shelley L. Anna and Hans C. Mayer, “Microscale tipstreaming in a microfluidic flow focusing device”, *Phys. Fluids*, **18**, 121512 (2006).
- [205] H. Kim, Dawei L. Link, David A. Weitz, M. Marquez, and Z. Cheng, “Controlled production of emulsion drops using an electric field in a flow-focusing microfluidic device”, *Appl. Phys. Lett.*, **91**, 133106 (2007).
- [206] S. Matosevic and Brian M. Paegel, “Stepwise synthesis of giant unilamellar vesicles on a microfluidic assembly line”, *J. Am. Chem. Soc.*, **133**, 2798–2800 (2011).
- [207] Peichi C. Hu, Su Li, and Noah Malmstadt, “Microfluidic fabrication of asymmetric giant lipid vesicles”, *ACS Appl. Mater. Interfaces*, **3**, 1434–1440 (2011).
- [208] Y. Chen, L. Wu, and C. Zhang, “Emulsion droplet formation in coflowing liquid streams”, *Phys. Rev. E*, **87**, 013002 (2013).
- [209] Philippe F. Devaux, “Static and dynamic lipid asymmetry in cell membranes”, *Biochemistry*, **30**, 1163–1173 (1991).
- [210] T. Hamada, Y. Miura, Y. Komatsu, Y. Kishimoto, M. Vestergaard, and M. Takagi, “Construction of asymmetric cell-sized lipid vesicles from lipid-coated water-in-oil microdroplets”, *J. Phys. Chem. B*, **112**, 14678–14681 (2008).
- [211] E. Kubatta and H. Rehage, “Characterization of giant vesicles formed by phase transfer processes”, *Colloid Polym. Sci.*, **287**, 1117–1122 (2009).
- [212] D. van Swaay and A. deMello, “Microfluidic methods for forming liposomes”, *Lab Chip*, **13**, 752–767 (2013).
- [213] A. Yamada, T. Yamanaka, T. Hamada, M. Hase, K. Yoshikawa, and D. Baigl, “Spontaneous transfer of phospholipid-coated oil-in-oil and water-in-oil micro-droplets through an oil/water interface”, *Langmuir*, **22**, 9824–9828 (2006).
- [214] David M. Kaz, Ryan McGorty, Madhav Mani, Michael P. Brenner, and Vinothan N. Manoharan, “Physical ageing of the contact line on colloidal particles at liquid interfaces”, *Nat. Mater.*, **11**, 138–142 (2012).
- [215] J. O. Indekeu, “Line tension at wetting”, *Int. J. Mod. Phys. B*, **8**, 309–345 (1994).
- [216] B. Widom, “Line tension and the shape of a sessile drop”, *Int. J. Phys. Chem*, **99**, 2803–2806 (1995).
- [217] S. M. Allen and J. W. Cahn, “A microscopic theory for antiphase boundary motion and its application to antiphase domain coarsening”, *Acta Metall.*, **27**, 1085–1095 (1975).
- [218] P. G. de Gennes, F. B-Wyart, and D. Quere, editors. *Capillarity and Wetting Phenomena: Drops, Bubbles, Pearls, Waves*. Springer, New York, (2004).
- [219] J. Stümpel, Winchil L. C. Vaz, and D. Hallmann, “An x-ray diffraction and differential scanning calorimetric study on the effect of sucrose on the properties of phosphatidylcholine bilayers”, *Biochim. Biophys. Acta*, **821**, 165–168 (1985).

- [220] M. del C. Luzardo, F. Amalfa, A. M. Nuñez, S. Díaz, A. C. Biondi de Lopez, and E. A. Disalvo, “Effect of trehalose and sucrose on the hydration and dipole potential of lipid bilayers”, *Biophys. J.*, **78**, 2452–2458 (2000).
- [221] H. D. Andesen, C. Wang, L. Arleth, G. H. Peters, and P. Westh, “Reconciliation of opposing views on membrane-sugar interactions”, *Proc. Nat. Acad. Sci. USA*, **108**, 1874–1878 (2011).
- [222] S. Nakata, T. Shiota, N. Kumazawa, and M. Denda, “Interaction between a monosaccharide and a phospholipid molecular layer”, *Colloids Surf. A*, **405**, 14–18 (2012).
- [223] J. Tian, A. Sethi, B. I. Swanson, B. Goldstein, and S. Gnanakaran, “Taste of sugar at the membrane: Thermodynamics and kinetics of the interaction of a disaccharide with lipid bilayers”, *Biophys. J.*, **104**, 622–632 (2013).
- [224] J. C. Shillcock and U. Seifert, “Thermally induced proliferation of pores in a model fluid membrane”, *Biophys. J.*, **74**, 1754–1766 (1988).
- [225] L. Fournier and B. Joós, “Lattice model for the kinetics of rupture of fluid bilayer membranes”, *Phys. Rev. E*, **67**, 051908 (2003).
- [226] J. W. Szostak, D. P. Bartel, and P. L. Luisi, *Nature*, **409**, 387–390 (2001).
- [227] Z. Nourian, W. Roelofsen, and C. Danelon, *Angew. Chem. Int. Ed.*, **51**, 3114–3118 (2012).
- [228] S. i. M. Nomura, K. Tsumoto, T. Hamada, K. Akiyoshi, Y. Nakatani, and K. Yoshikawa, *ChemBioChem*, **4**, 1172–1175 (2003).
- [229] H. Saito, Y. Kato, M. Le Berre, A. Yamada, T. Inoue, K. Yoshikawa, and D. Baigl, *ChemBioChem*, **10**, 1640–1643 (2009).
- [230] H. Matsubayashi, Y. Kuruma, and T. Ueda, *Angew. Chem. Int. Ed.*, **53**, 7535–7538 (2014).
- [231] C. Dietrich, L. A. Bagatolli, Z. N. Volovyk, N. L. Thompson, M. Levi, K. Jacobson, and E. Gratton, *Biophys. J.*, **80**, 1417–1428 (2001).
- [232] S. L. Veatch and S. L. Keller, *Biophys. J.*, **85**, 3074–3083 (2003).
- [233] D. Scherfeld, N. Kahya, and P. Schwille, *Biophys. J.*, **85**, 3758–3768 (2003).
- [234] T. Baumgart, S. T. Hess, and W. W. Webb, *Nature*, **425**, 821–824 (2003).
- [235] D. L. Richmond, E. M. Schmid, S. Martens, J. C. Stachowiak, N. Liska, and D. A. Fletcher, “Forming giant vesicles with controlled membrane composition, asymmetry, and contents”, *Proc. Natl. Acad. Sci. U.S.A.*, **108**, 9431–9436 (2011).
- [236] P. F. Devaux and R. Morris, *Traffic*, **5**, 241–246 (2004).
- [237] G. van Meer, D. R. Voelker, and G. W. Feigenson, *Nat. Rev. Mol. Cell Biol.*, **9**, 112–124 (2008).
- [238] S. Pautot, B. J. Frisken, and D. A. Weitz, *Langmuir*, **19**, 2870–2879 (2003).

BIBLIOGRAPHY

- [239] Y.-C. Tan, K. Hettiarachchi, M. Siu, Y.-R. Pan, and A. P. Lee, *J. Am. Chem. Soc.*, **128**, 5656–5658 (2006).
- [240] K. Funakoshi, H. Suzuki, and S. Takeuchi, *J. Am. Chem. Soc.*, **129**, 12608–12609 (2007).
- [241] H.C. Shum, D. Lee, I. Yoon, T. Kodger, and D. A. Weitz, *Langmuir*, **24**, 7651–7653 (2008).
- [242] J. C. Stachowiak, D. L. Richmond, T. H. Li, A. P. Liu, S. H. Parekh, and D. A. Fletcher, *Proc. Natl. Acad. Sci. U.S.A.*, **105**, 4697–4702 (2008).
- [243] S. Ota, S. Yoshizawa, and S. Takeuchi, *Angew. Chem. Int. Ed.*, **48**, 6533–6537 (2009).
- [244] S.-Y. Teh, R. Khnouf, H. Fan, and A. P. Lee, *Biomicrofluidics*, **5**, 044113 (2011).
- [245] L. R. Arriaga, S. S. Datta, S.-H. Kim, E. Amstad, T. E. Kodger, F. Monroy, and D. A. Weitz 2014, *Small*, **10**, 950–956 (2014).
- [246] S. Matosevic and B. M. Paegel, *Nat. Chem.*, **5**, 958–963 (2013).
- [247] K. Maeda, H. Onoe, M. Takinoue, and S. Takeuchi, *Adv. Mater.*, **24**, 1340–1346 (2012).
- [248] J. Eggers, *Rev. Mod. Phys.*, **69**, 865–929 (1997).
- [249] S. Murata, A. Konagaya, S. Kobayashi, H. Saito, and M. Hagiya, *New Gener. Comput.*, **31**, 27–45 (2013).
- [250] M. Hagiya, A. Konagaya, S. Kobayashi, H. Saito, and S. Murata, *Acc. Chem. Res.*, **47**, 1681–1690 (2014).